1.0

1.1

1.25

2.8   2.5

3.2   2.2

3.6

4.0   2.0

1.8

1.4   1.6

MICROCOPY RESOLUTION TEST CHART

NATIONAL BUREAU OF STANDARDS-1963-A

# PARTICLE IMPACT DAMAGE IN SILICON NITRIDE

Annual Report — Part III

May 1979

By: K. C. Dao, D. A. Shockey, L. Seaman,
D. R. Curran, and D. J. Rowcliffe

D D C

RECEIVED

SEP 10 1979

C

AD A073570

DDC FILE COPY

79 07 24 041

⑥ **PARTICLE IMPACT DAMAGE IN SILICON NITRIDE**

⑨ Annual Report — Part III 3,

⑪ May 1979   ⑫ 116 p.

⑩

By: K. C. Dao, D. A. Shockey, L. Seaman,
D. R. Curran and D. J. Rowcliffe

Prepared for:

Office of Naval Research
800 N. Quincy Street
Arlington, VA 22203

Attn: Dr. R. C. Pohanka
Dr. A. M. Diness

⑮

Contract N00014-76-C-0657

SRI Project PYU-4928

Approved:

G. R. Abrahamson, Director
Poulter Laboratory

P. J. Jorgensen, Vice President
Physical and Life Sciences

## SUMMARY

In the study of fracture in thick silicon nitride plates by
particle impact and quasi-static indentation, we used three types of
silicon nitride:  hot pressed, reaction bonded, and oxidized hot
pressed.  The fractures were characterized, quantified, and where
possible, correlated with calculated elastic stress fields.

The fracture damage was seen to occur in well-defined progressive
stages.  For impact loads or quasi-static indentation loads that do
not appreciably exceed the flow stress in the silicon nitride, the
elastic radial tensile stresses cause ring and Hertzian cone cracks
to form.  In the dynamic case, the short duration of the tensile pulse
restricts the formation of the ring cracks to the vicinity of the
maximum contact radius of the impacting particle.  In the quasi-static
case, the ring cracks form well outside the maximum contact radius,
suggesting that the fracture nucleation and growth kinetics play a
significant role in determining the extent of damage.

For dynamic loads that exceed the flow stress of the silicon
nitride, the plastic flow reduces the tensile radial stress and produces
tensile hoop stresses, which in turn, cause radial cracks to form and
propagate.  At still higher dynamic loads, lateral cracks form.  The
intersection of these later-stage cracks with the free surface causes
material removal (erosion).

Computer modeling with elastic-plastic material models will be
required to improve our understanding of this fracture behavior.  Radial
and lateral cracks were not formed in the quasi-static indentation
tests because flow and failure of the indentors prevented application
of sufficient load levels.

The oxidized surface on hot pressed silicon nitride spalled
locally under particle impact.  Crack size determination showed that
the oxide has little influence on the morphology and extent of fracture
damage in the host material.

iii

We found that the local crack propagation is sensitive to microstructural features in the hot pressed silicon nitride; the fractures were intergranular and the fracture paths were tortuous. Thus, resistance to erosion might be improved by modifying the size and shape of the grains. In reaction-bonded silicon nitride, on the other hand, the grains and pores are mostly smaller than 1 μm and do not appear to exert a marked influence on crack propagation and macrofracture.

At high temperatures representative of turbine blade operating conditions, the silicon nitride exhibited significantly more resistance to fracture, thus suggesting that future work should focus on this effect.

## CONTENTS

ILLUSTRATIONS

vii

ILLUSTRATIONS (continued)

ILLUSTRATIONS (concluded)

## TABLES

## ACKNOWLEDGMENTS

# I  INTRODUCTION

Development of materials and fabrication processes for ceramic
turbine components continues to emphasize silicon nitride and silicon
carbide.  Although hot pressed high-density silicon nitride has superior
strength, the reaction bonded silicon nitride is more resistant to high-
temperature creep and can be formed into components less expensively.
Therefore, both types of silicon nitride hold promise of being useful
gas turbine materials.  However, because silicon nitride is brittle,
it is very susceptible to localized surface cracking by repeated bombard-
ments of debris and solid impurities in the hot and corrosive environment
of a turbine engine.  Brittle cracks that form in silicon nitride may
cause serious strength degradation, leading to gradual deterioration
in performance and even failure of the vital ceramic components.  To
solve this problem, we need to define the mechanisms that govern the
impact erosion process in silicon nitride.

In our earlier work on zinc sulfide,[1] we noted the similarity
between quasi-static indentation and dynamic particle impact fracture
damage and suggested the use of quasi-static indentation experiments
and theory to characterize the impact erosion process in ZnS.  Silicon
nitride, however, is a stronger ceramic and its response to particle
contact situations is little known.  Both quasi-static indentation and
particle impact experiments were therefore required to determine if the
quasi-static approach was adequate for silicon nitride.

The problem of progressive oxidation of silicon nitride at high
turbine operating temperatures has been recently recognized,[2,3] and it
is believed that gradual thickening of the oxide scale coupled with
significant spallation of the scale by particle impact may accelerate
the erosion process.  However, the effect of the oxide scale on the
erosion process has not, to our knowledge, been experimentally investigated.

1

The Navy is also interested in determining whether microstructural features may influence resistance to impact erosion of these materials and, if so, how optimum microstructures can be produced.

The specific objectives of this research were to:

(1) Define in detail the mechanism of particle impact fracture in hot pressed and reaction bonded silicon nitride.

(2) Investigate the response of silicon nitride to quasi-static indentation.

(3) Explain the effects of particle size, particle material, and the oxide scale on particle contact damage in silicon nitride.

(4) Describe the influence of microstructural features on crack propagation and particle contact fracture damage.

(5) Determine the effect of high temperature on impact erosion resistance of silicon nitride.

(6) Develop analyses for predicting particle impact fracture behavior of silicon nitride.

In the remainder of this report we describe our progress toward meeting these objectives. Section II describes the material characterization, Sections III and IV discuss the dynamic and static experimentation, respectively, and Section V covers the observed effect of high temperature on the dynamic results. Section VI describes the observed correlation of fracture behavior with microstructural features, and Section VII discusses the analysis of the experimental data. Finally, in Section VIII we present our conclusions.

## II SPECIMEN MATERIALS

### Hot Pressed Silicon Nitride

Hot pressed silicon nitride (HP $Si_3N_4$) NC132 with a density of
3.2 $g/cm^3$ was obtained from Norton Company in the form of a flat billet
approximately 15 cm by 15 cm by 1.3 cm. X-ray diffraction showed
$\beta$-$Si_3N_4$ and small peaks attributed to $WSi_2$ and $Si_2ON_2$. The $WSi_2$
results from reaction of tungsten carbide (WC) and $Si_3N_4$ during hot
pressing, and the WC pick-up arises from the use of WC milling balls
in the original powder processing. Specimens for the impact experi-
ments were all taken parallel to the hot pressing direction and polished
to a 1-$\mu$m particle finish. In this condition the surface was essentially
featureless. The microstructure illustrated in Figure 1 was revealed by
etching in a solution of 30% HF, 25% $H_2O_2$ and 5% $HNO_3$ at 100°C for
up to 2 minutes. The structure consists of $\beta$-$Si_3N_4$ with large grains
of about 2 $\mu$m and submicrometer grains. Most grains are equiaxed, but
occasional ones have aspect ratios up to 10:1. No microstructural
evidence of grain boundary phases or inclusions could be found.

### Oxide Scale

Several samples of NC132 were oxidized for 100 hours at 1250°C
in air to form an oxide scale about 20 $\mu$m thick. The structure and
composition of scales on NC132 have been studied in detail.[2,3] Scales
formed at 1250°C consisted of $\alpha$-cristobalite and $MgSiO_3$ as major
crystalline phases with small amounts of $\beta$-$Si_3N_4$ and $Si_3ON_2$. The most
striking microstructural feature of the scale was its porosity. Pores
up to 5 $\mu$m in diameter were present throughout the scale's thickness,
and pits were formed beneath the scale in the unoxidized material. The
outer surface of the scale consisted of a thin layer of much less
porous oxide.

MP–4928–71

FIGURE 1    MICROSTRUCTURE OF HOT PRESSED SILICON NITRIDE

4

## Reaction Bonded Silicon Nitride

Reaction bonded silicon nitride (RB $Si_3N_4$), NC350, was obtained from the Norton Company in the form of a disc approximately 22.5 cm in diameter by 6 cm thick. Test specimens were polished to a 1-$\mu$m particle finish. A scanning electron micrograph of the microstructure at the specimen surface is shown in Figure 2. Density and pore size distribution were measured using a mercury porosimeter; the results are shown in Figure 3. The density was 2.65 g/cm$^3$, which is 84.5% of the theoretical value. The pore size ranged from 0.01 to 0.1 $\mu$m, with the mean close to 0.05 $\mu$m. X-ray diffraction studies identified $\alpha$- and $\beta$-$Si_3N_4$ with no other second phases. A comparison of peak intensities showed the material to consist of approximately 60% $\alpha$-$Si_3N_4$ and 40% $\beta$-$Si_3N_4$.

5

5 μm
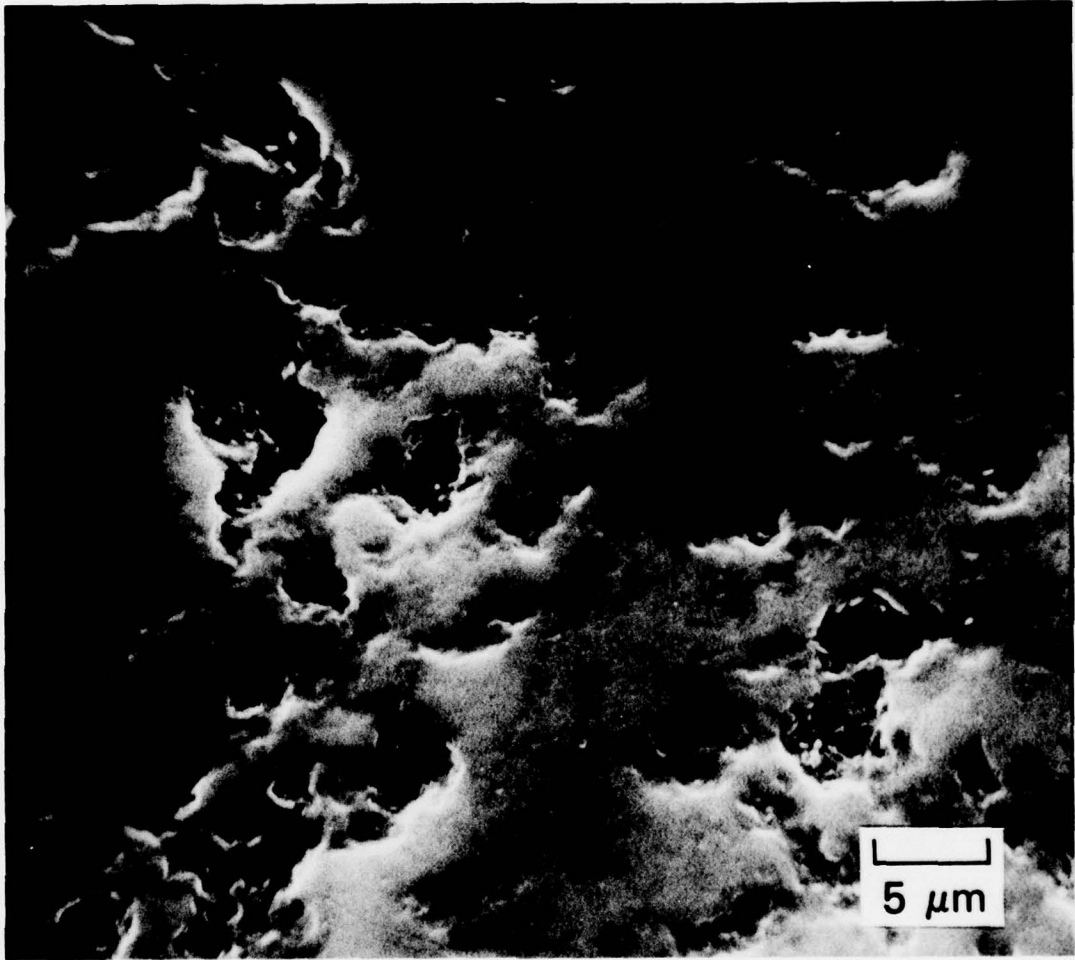
MP-4928-72

FIGURE 2    MICROSTRUCTURE OF REACTION BONDED SILICON NITRIDE

6
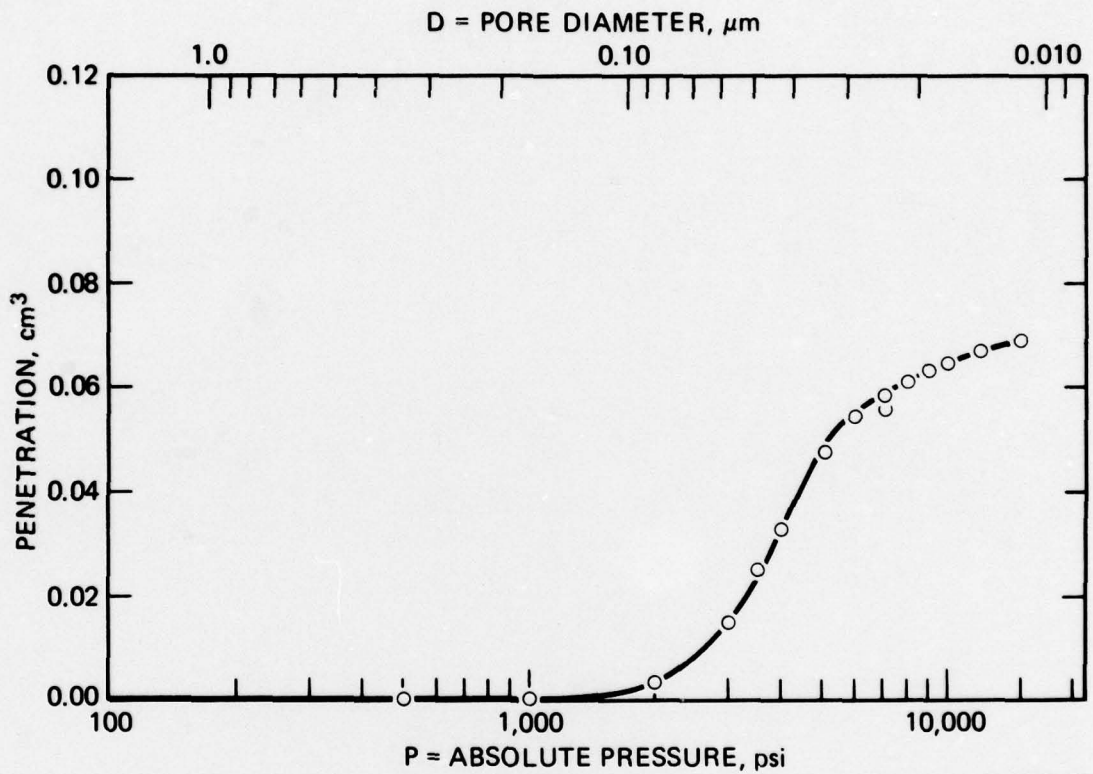
FIGURE 3    PORE SIZE DISTRIBUTION IN REACTION BONDED SILICON NITRIDE
(PENETRATION IS A DIRECT MEASURE OF VOLUME FRACTION OF
PORES AND MAXIMUM PENETRATION, ABOUT 0.07 cm$^3$ CORRESPONDS
TO VOLUME FRACTION OF ALL PORES, 0.155)

MA-4928-73

## III PARTICLE IMPACT EXPERIMENTS

### Experimental Procedure

An impact facility for accelerating small, single, solid particles against target specimens, as shown schematically in Figure 4, was designed and constructed at SRI International for our ONR erosion program.  Individual spherical particles of WC and steel, positioned in the breech section of the gun and held in place by a magnetic ring, were accelerated by fast release of nitrogen gas.  Fast release of the high-pressure gas was activated by a rupture disc assembly that consisted essentially of a thin disc located in a two-part chamber,  Figure 4(b). The gas pressure was allowed to build up on one side of the chamber.  At a desired pressure, the disc ruptured, dumping the gas to the side where the particle was initially at rest.  The expansion of the gas was rapid and the particle was propelled to high velocities.  The disc material and thickness were varied to provide a wide range of velocity.

The impact and rebound velocities were measured by a system of three photomultipliers, each consisting of a photosensitive element located in a housing that was connected to a light pipe.  The three light pipes directed light at locations of known distances apart along the path of the particle.  Light reflected from the moving particle entered the pipes and sent signals via the photomultipliers to a recorder.  At each photomultiplier location, the moving particle was illuminated by a common light source via individual fiber optics cables. Typical velocity records are shown in Figure 5.

The particle-impact facility is capable of operating at temperatures from ambient to 1500°C and at velocities from 13 to 700 m/s.  Maximum impact velocity depends on particle size.  Velocities higher than 700 m/s can be obtained by higher gas pressures and improved gas-release devices. Particles of the following diameters can be accelerated in the facility:

9
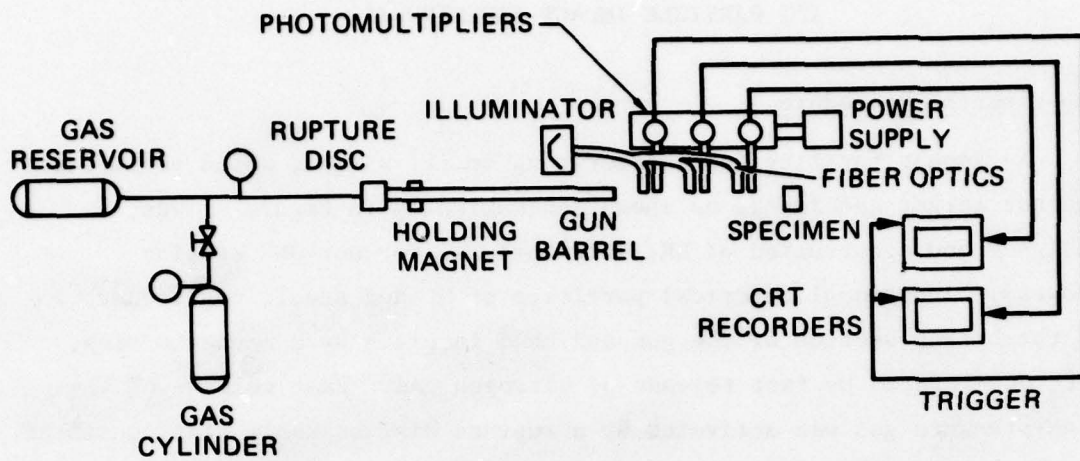
(a) SCHEMATIC OF THE FACILITY
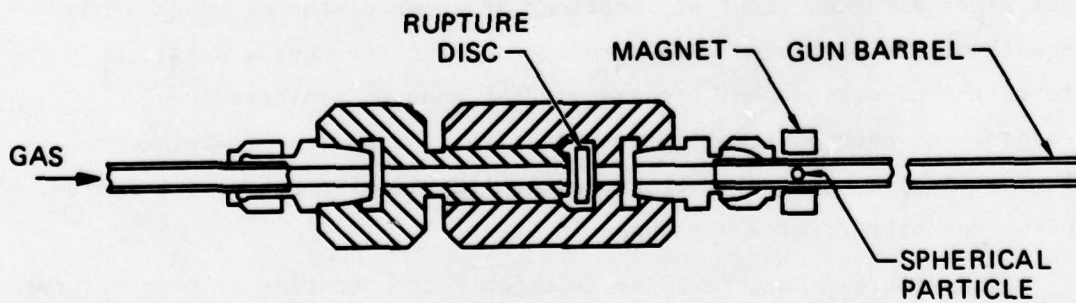


(b) DETAIL OF RUPTURE DISC ASSEMBLY FOR FAST RELEASE OF GAS

MA-4928-88

FIGURE 4    SRI PARTICLE-IMPACT FACILITY

10

STATION 1

ARRIVAL

STATION 2

2 V/DIVISION

ARRIVAL

REBOUND

REBOUND

500 µs/DIVISION
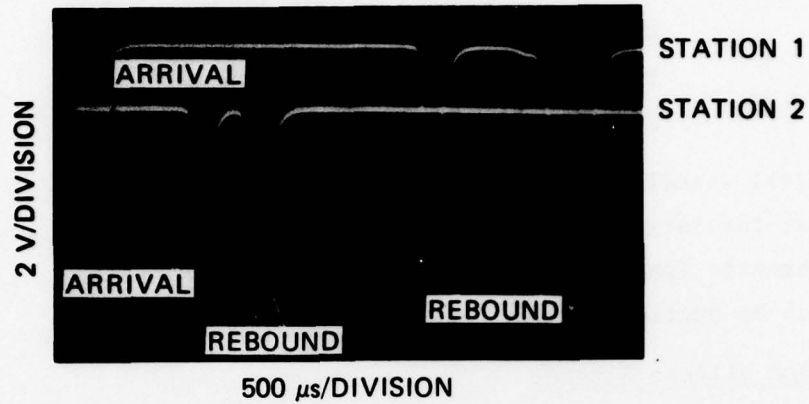
Particle: Steel, 2.4 mm
Target: $Si_3N_4$
Velocity: 56.4 m/s

STATION 1

1 V/DIVISION

ARRIVAL

STATION 2

ARRIVAL

PARTICLE
FRAGMENTATION

200 µs/DIVISION
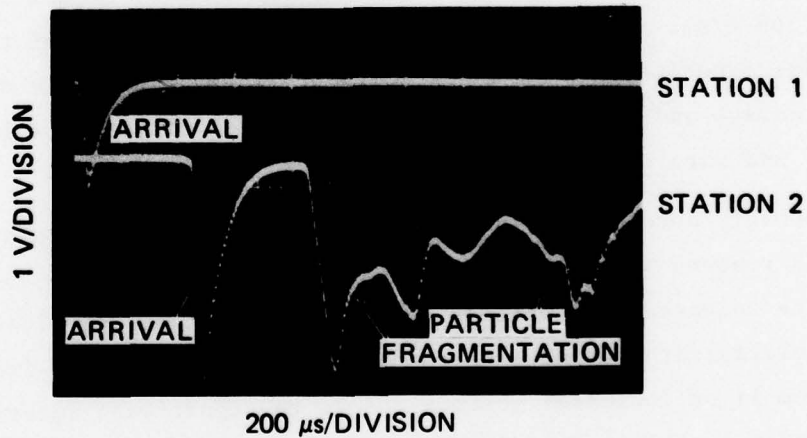
Particle: WC, 2.4 mm
Target: $Si_3N_4$
Velocity: 120.9 m/s

MP-4928-12

FIGURE 5   TYPICAL VELOCITY RECORDS

11

|                | Diameter (mm) |
|----------------|---------------|
| Tungsten carbide | 0.4 to 4.8 |
| Steel          | 1.0 to 4.8 |
| Glass          | 0.1 to 4.8 |
| Nylon          | 1.0 to 4.8 |
| $Al_2O_3$      | 3.2 to 4.8 |

The smallest diameter is dictated by the smallest commercially available particles; the largest is the diameter of the largest current gun barrel. The nonmagnetic spheres, glass, nylon and $Al_2O_3$, can be held in the gun breech by suction.

## Hot Pressed Silicon Nitride

### Summary of Particle Impact Experiments

We performed 43 particle impact experiments on HP $Si_3N_4$ using spherical particles of two sizes (1.6 and 2.4 mm diameter), two particle materials (tungsten carbide and steel), and a range of impact velocity (16.9 to 368 m/s). Table 1 lists the important parameters of these tests. The experiments were expected to provide a wide range of fracture damage and show influences of impact velocity, particle size, material, and particle/target combination.

Reasonably normal impacts and accurate velocity measurements (both impact and rebound velocities) were realized for most of the 43 experiments. The selected combinations of impact velocities, particle sizes, and particle/target combinations resulted in a wide range of fracture damage from light incipient surface cracks to significant material removal and target failure. Some particles were recovered and examined for impact damage. The results were included in Table 1.

### Fractographic Observations

Optical micrographs of typical surface damage observed in the HP $Si_3N_4$ specimens are presented in Figures 6 through 8. The results show increasing surface damage with increased impact velocity as expected.

12

Table 1

PARTICLE IMPACT EXPERIMENTS ON HOT PRESSED SILICON NITRIDE

| Test No. | SRI No. | Impact Velocity (m/s) | Rebound Velocity (m/s) | Damage to Particle |
|---|---|---|---|---|
| Impact configuration A (2.40-mm-diameter steel, HP $Si_3N_4$) | | | | |
| 1 | 4928-119 | 42.3 | a | Intact |
| 2 | 4928-131 | 42.3 | 32 | Intact |
| 3 | 4928-133 | 46.2 | a | Flattened |
| 4 | 4928-132 | 56.4 | 34 | Flattened |
| 5 | 4928-129 | 62 | 36 | b |
| 6 | 4928-120 | 87.6 | a | b |
| 7 | 4928-121 | 105.8 | 52 | b |
| 8 | 4928-122 | 133.7 | 58 | b |
| 9 | 4928-124 | 141 | 63 | b |
| 10 | 4928-123 | 154 | 67 | b |
| 11 | 4928-126 | 195 | 69 | b |
| 12 | 4928-127 | 231 | 70 | Fragmentation[c] |
| 13 | 4928-128 | 299 | a | Fragmentation[c] |
| Impact configuration B (2.40 mm-diameter WC, HP $Si_3N_4$) | | | | |
| 14 | 4928-117 | 16.9 | 15 | Intact |
| 15 | 4928-116 | 19.5 | 16 | Intact |
| 16 | 4928-115 | 24.2 | 18 | Flattened |
| 17 | 4928-114 | 31.7 | 24 | Flattened |

[a] Rebound velocity not available or particle fragmented.

[b] Particles were not recovered or no signals from fragments.

[c] Determined from photomultiplier signals of rebounded fragments.

## Table 1 (continued)

### PARTICLE IMPACT EXPERIMENTS ON HOT PRESSED SILICON NITRIDE

| Test No. | SRI No. | Impact Velocity (m/s) | Rebound Velocity (m/s) | Damage to Particle |
|---|---|---|---|---|
| Impact configuration B (continued) (2.40 mm-diameter WC, HP $Si_3N_4$) | | | | |
| 18 | 4928-112 | 33.8 | 25 | Flattened |
| 19 | 4928-113 | 39 | 27 | b |
| 20 | 4928-118 | 39 | 30 | b |
| 21 | 4928-111 | 46.2 | 35 | b |
| 22 | 4928-109 | 50.8 | 39 | b |
| 23 | 4928-110 | 52.9 | 39 | b |
| 24 | 4928-108 | 92.3 | 25 | Fragmentation[c] |
| 25 | 4928-107 | 97.7 | a | Fragmentation[c] |
| 26 | 4928-105 | 121 | a | Fragmentation[c] |
| 27 | 4928-106 | 121 | a | Fragmentation[c] |
| 28 | 4928-103 | 159 | a | Fragmentation[c] |
| 29 | 4928-102 | 169 | a | Fragmentation[c] |
| 30 | 4928-104 | 231 | a | Fragmentation[c] |
| Impact configuration C (1.60-mm-diameter WC, HP $Si_3N_4$) | | | | |
| 31 | 4928-99 | 37.6 | 30 | b |
| 32 | 4928-97 | 46.2 | 35 | b |
| 33 | 4928-96 | 67.7 | 43 | Flattened |
| 34 | 4928-94 | 78.1 | a | Fragmentation[c] |

[a] Rebound velocity not available or particle fragmented.

[b] Particles were not recovered or no signals from fragments.

[c] Determined from photomultiplier signals or rebounded fragments.

14

## Table 1 (concluded)

| Test No. | SRI No. | Impact Velocity (m/s) | Rebound Velocity (m/s) | Damage to Particle |
|---|---|---|---|---|
| Impact configuration C (concluded) (1.60-mm-diameter WC, HP $Si_3N_4$) | | | | |
| 35 | 4928-95 | 78.1 | 30 | Fragmentation[c] |
| 36 | 4928-93 | 84.6 | 30 | Fragmentation[c] |
| 37 | 4928-92 | 92.4 | 24 | Fragmentation[c] |
| 38 | 4928-89 | 102 | 24 | Fragmentation[c] |
| 39 | 4928-91 | 127 | a | Fragmentation[c] |
| 40 | 4928-87 | 195 | a | b |
| 41 | 4928-100 | 254 | a | Fragmentation[c] |
| 42 | 4928-101 | 254 | a | Fragmentation[c] |
| 43 | 4928-64 | 368 | a | b |

[a]Rebound velocity not available or particle fragmented.

[b]Particles were not recovered or no signals from fragments.

[c]Determined from photomultiplier signals of rebounded fragments.
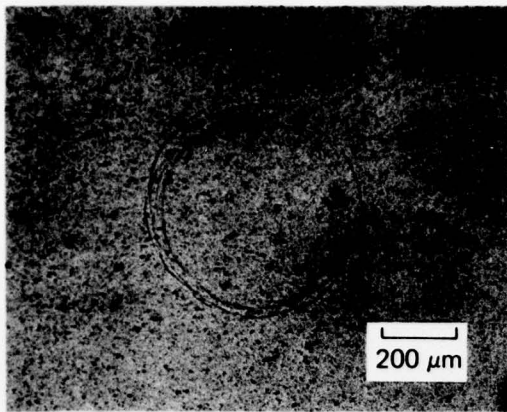
(a) 42.3 m/s
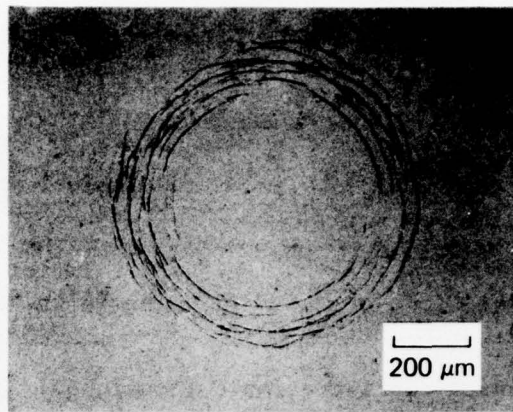
(d) 195 m/s
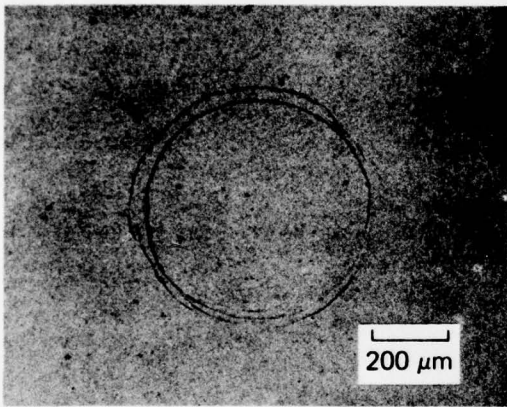
(b) 56.4 m/s
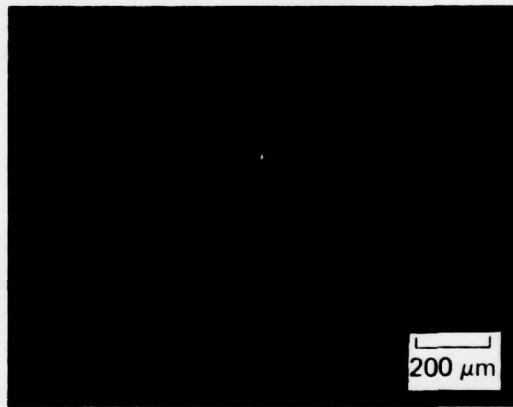
(e) 231 m/s
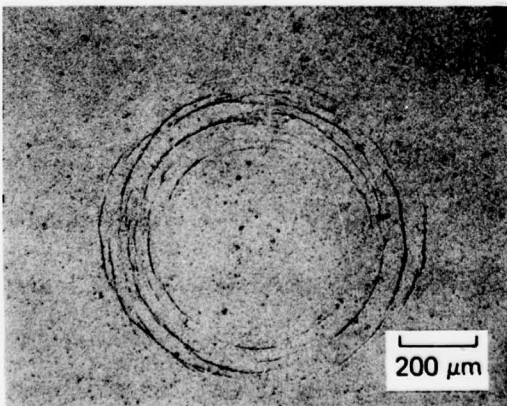
(c) 154 m/s
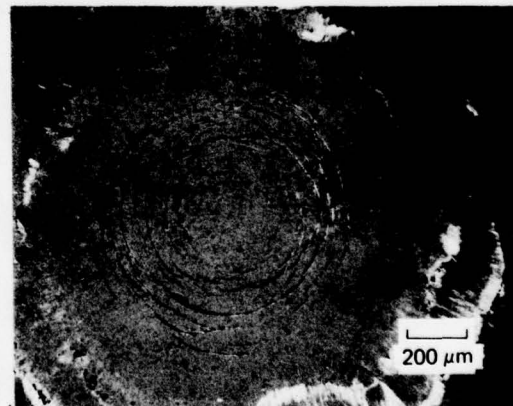
(f) 299 m/s

MP-4928-31

FIGURE 6    TYPICAL IMPACT DAMAGE IN HP Si$_3$N$_4$ BY 2.4-mm-DIAMETER STEEL SPHERES
(Impact Configuration A)

16
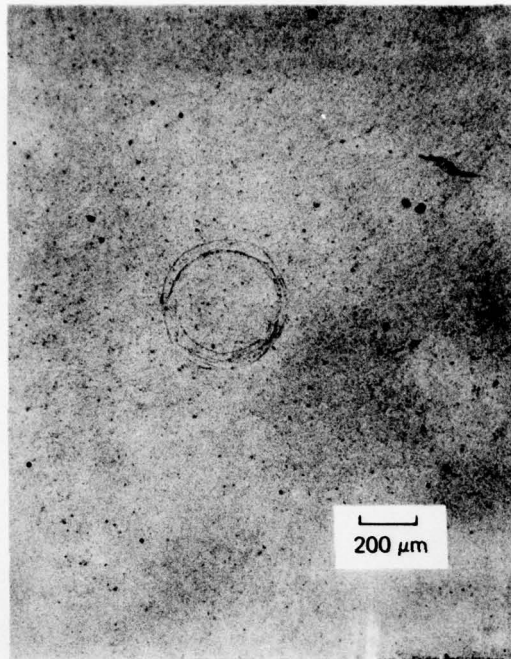
(a) 19.5 m/s
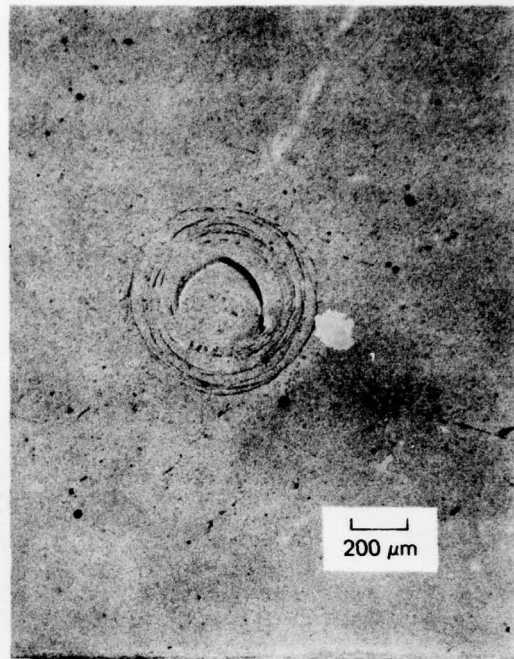
(c) 46.2 m/s
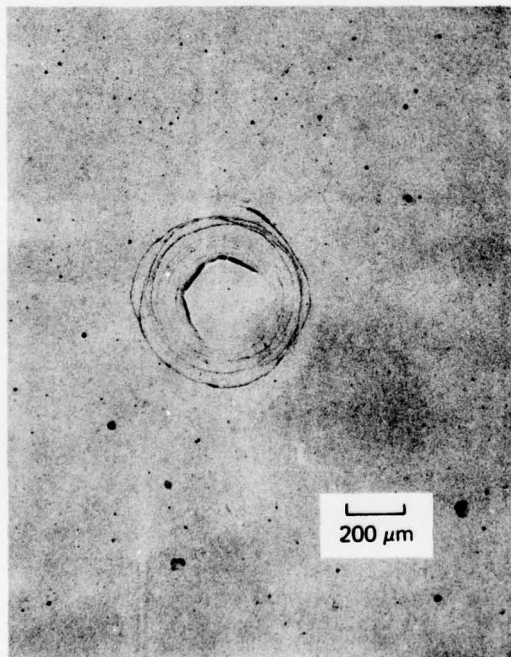
(b) 39 m/s
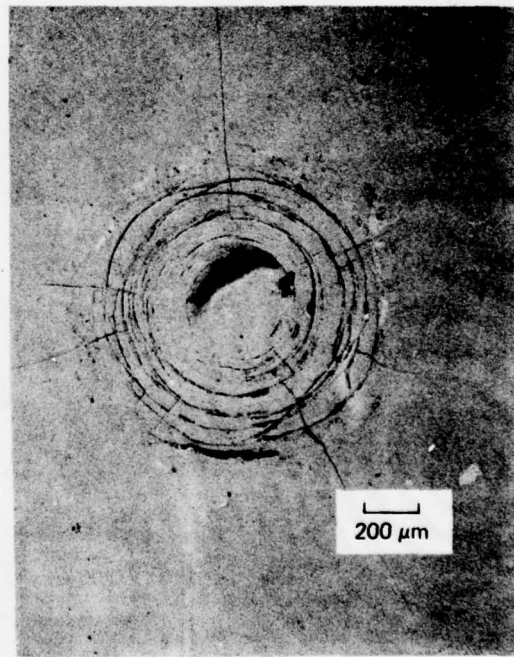
(d) 97.7 m/s

MP-4928-33

FIGURE 7    TYPICAL IMPACT DAMAGE IN HP $Si_3N_4$ BY 2.4-mm-DIAMETER WC SPHERES
(Impact Configuration B)

17

(e) 121 m/s

(g) 169 m/s
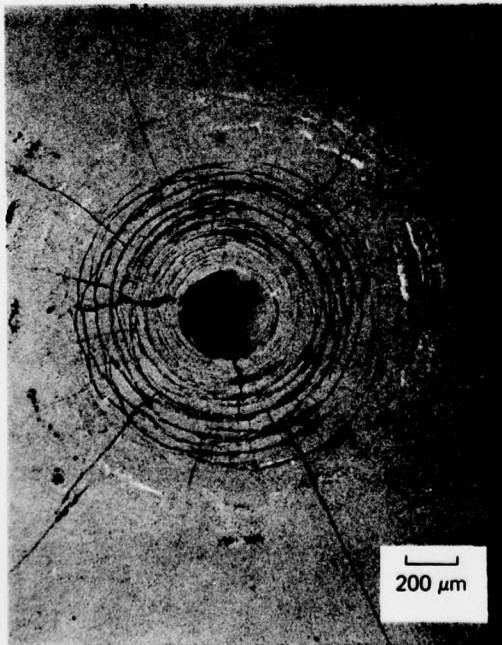
(f) 159 m/s
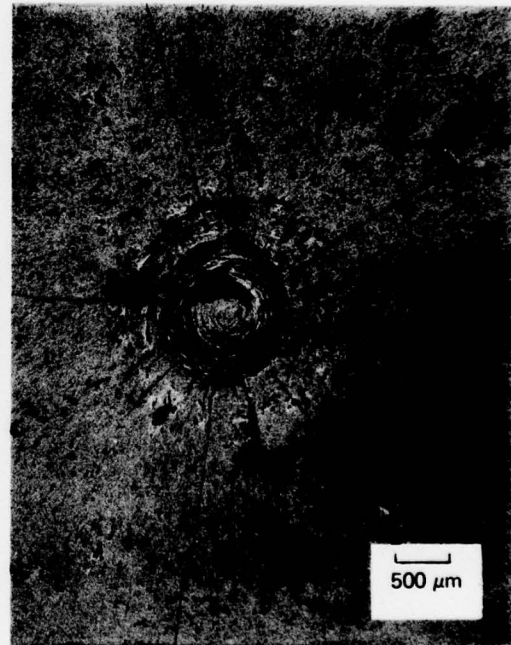
(h) 231 m/s

MP–4928–34

FIGURE 7    TYPICAL IMPACT DAMAGE IN HP $Si_3N_4$ BY 2.4-mm-DIAMETER WC SPHERES
(Impact Configuration B) (Concluded)

18
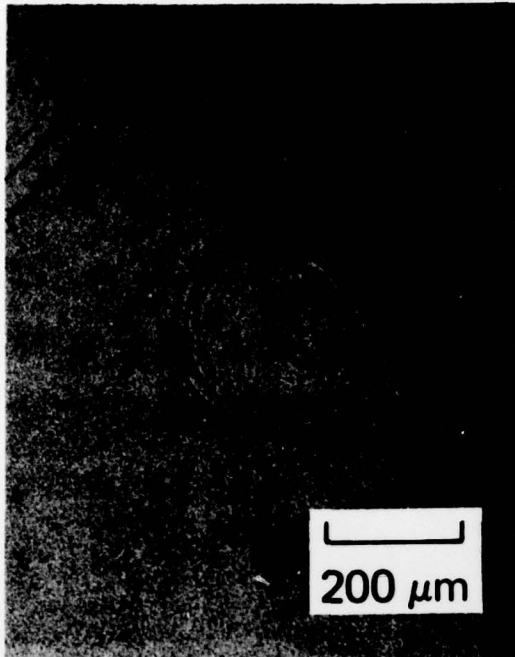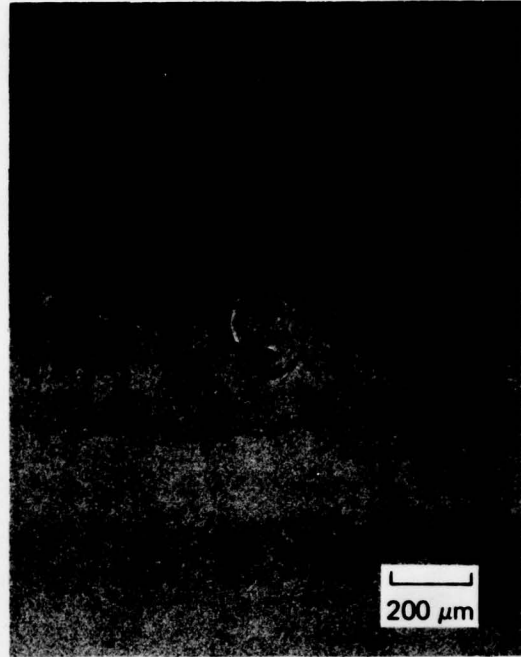
(a) 37.6 m/s        (c) 78.1 m/s
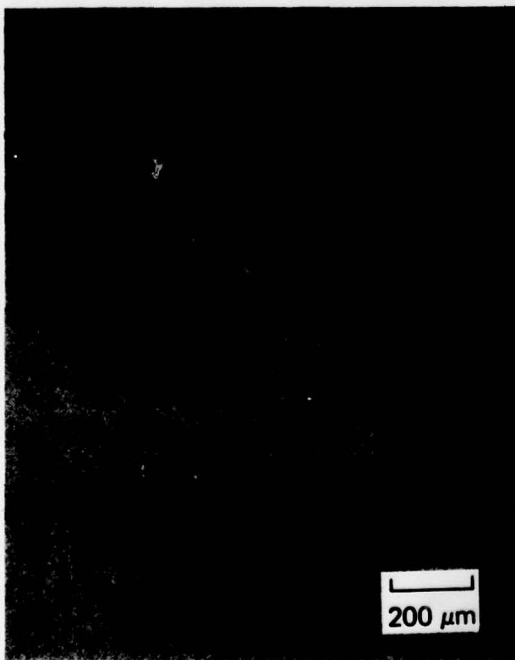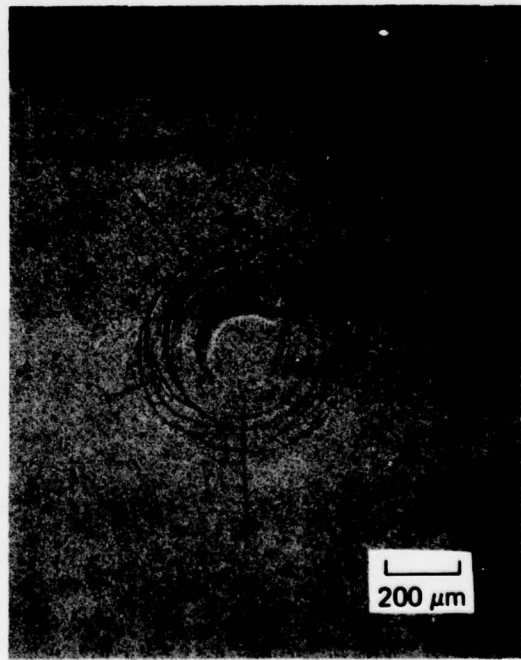
(b) 67.7 m/s        (d) 92.4 m/s

MP–4928–35

FIGURE 8     TYPICAL IMPACT DAMAGE IN HP $Si_3N_4$ BY 1.6-mm-DIAMETER WC SPHERES
(Impact Configuration C)

19
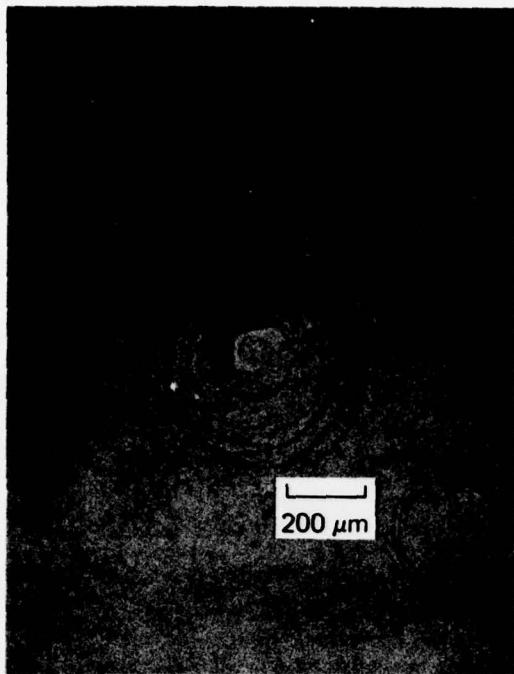
(e) 102 m/s
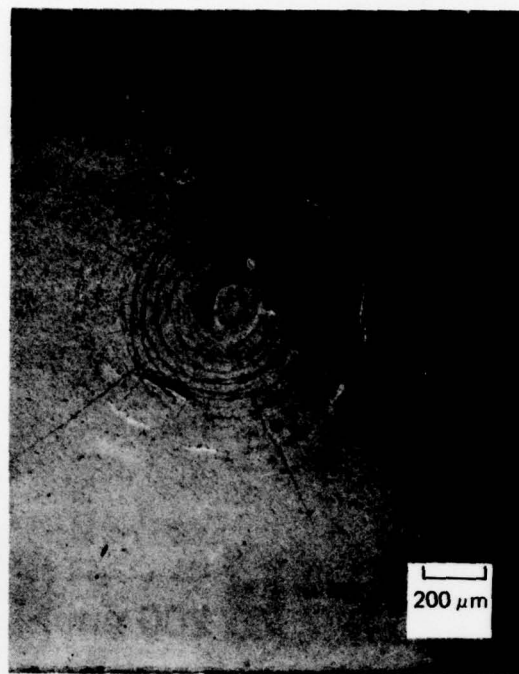
(g) 195 m/s
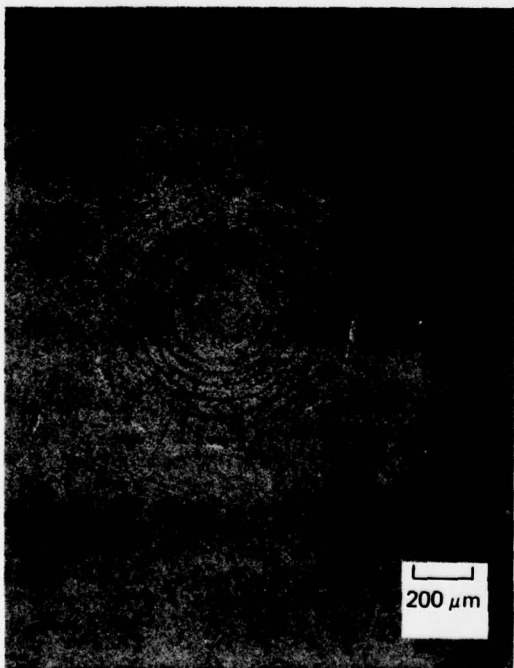
(f) 127 m/s
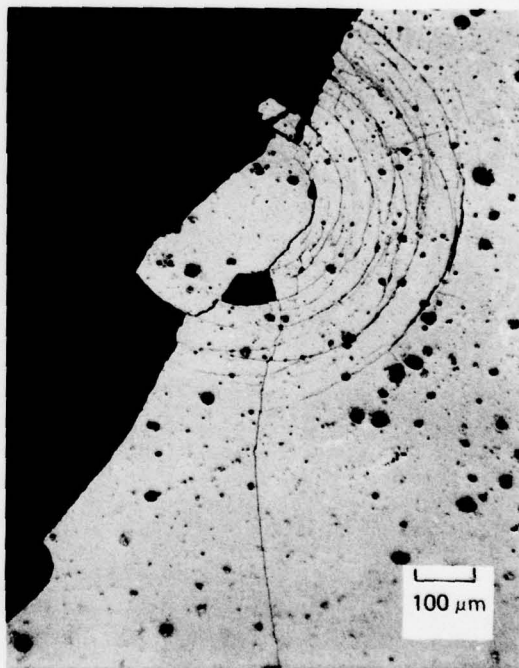
(h) 368 m/s

MP-4928-36

FIGURE 8    TYPICAL IMPACT DAMAGE IN HP Si$_3$N$_4$ BY 1.6-mm-DIAMETER WC SPHERES
(Impact Configuration C) (Concluded)

20

The cracking sequence caused by the 1.6- and 2.4-mm-diameter WC spheres was qualitatively similar. It consisted of ring cracks (shallow circumferential cracks) followed by a plastic impression, radial cracks, lateral cracks, and target fracture.

Damage in HP $Si_3N_4$ due to 2.4-mm-diameter steel spheres (impact configuration A) consisted exclusively of ring cracks throughout the velocity range. At 299 m/s the steel projectile disintegrated, and no significant increase in target damage was observed beyond this velocity. The white areas in Figure 7(f) seem to result from outflow of material from the disintegrating sphere. Ring cracks started to form at fairly low velocities for all three impact configurations (42.3 m/s, Figure 6; 19.5 m/s, Figure 7; and 37.6 m/s, Figure 8). As impact velocity increased, more and longer ring cracks formed.

The ring cracks appeared to be similar to the Hertzian ring cracks formed under quasi-static loading (Reference 4, for example). A magnified view of a typical population of ring cracks is presented in Figure 9. Most ring cracks were short segmental cracks that seemed to nucleate at an arbitrary location where a particular flaw might exist, propagated circumferentially a short distance, and stopped. There were also some full-circle cracks. The number of these cracks increased strongly with increasing impact velocity, spreading both toward the contact center and to outer regions.

We produced ring cracks by both quasi-static indentation and particle impact and used replica and scanning electron microscopy to examine the influence of microstructure on crack nucleation and growth. The results are described in Section VI.

Slight plastic impressions were first observed at 31.7 and about 42 m/s for impact configurations B and C, respectively. As the velocity increased, the impression became deeper but did not enlarge. Plastic impression and radial cracks seemed to appear at the same time in the cracking sequence. As the impression deepened with increased velocity, the radial cracks grew in both size and number, although only a few (8 or 9) of the radial cracks grew to great lengths (several millimeters).
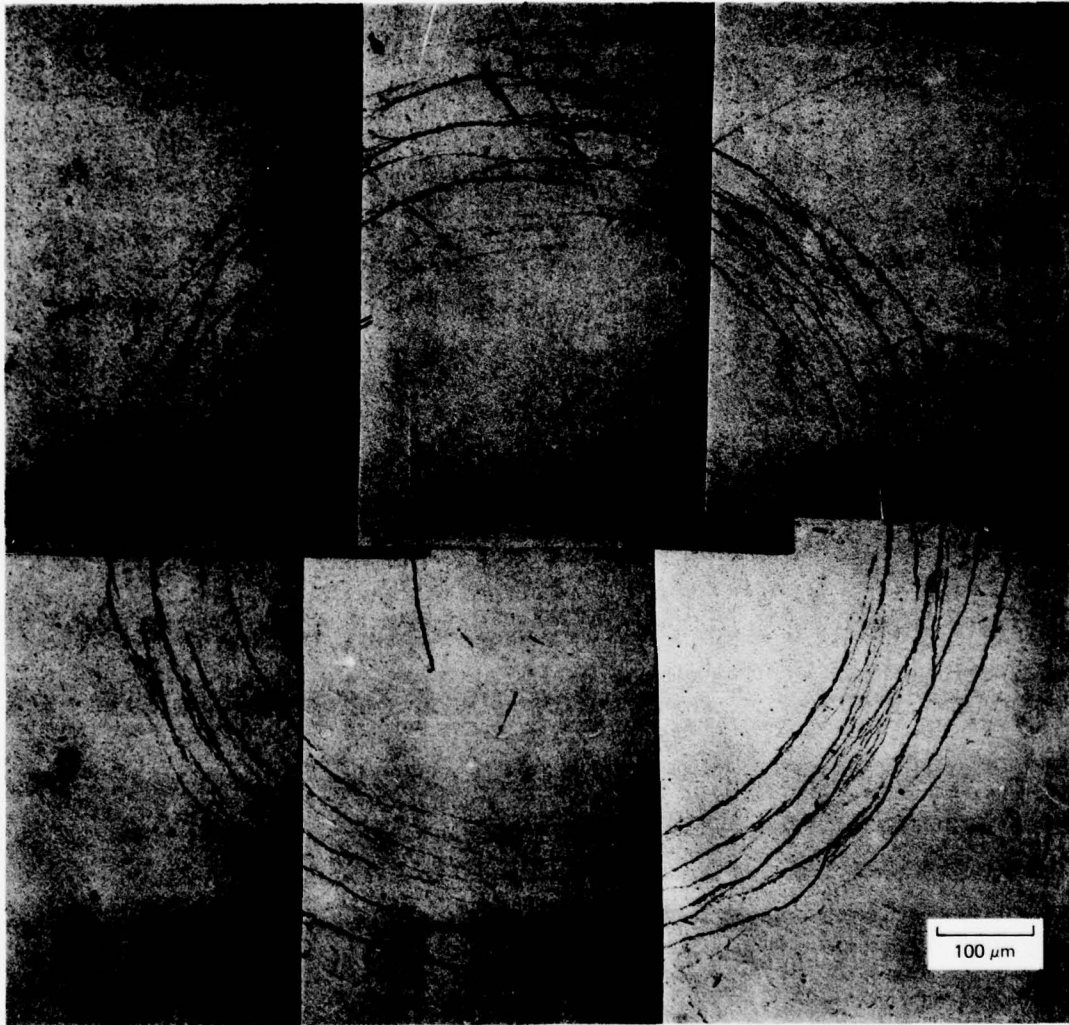
MP–4928–37

FIGURE 9    A MAGNIFIED VIEW OF TYPICAL RING CRACKS IN HP $Si_3N_4$ (Particle: 2.4-mm-diameter steel sphere, Velocity: 195 m/s, See also Figure 6d)

Plastic deformation in the target probably modifies the previous elastic stress field outside the contact zone. The hoop stress must become tensile, creating the necessary conditions for radial cracking as observed.

To determine internal damage and the extent of growth of the various cracks below the specimen surface, we sectioned the specimens to expose surfaces at various radial distances from the center of the contact zone and examined the subsurface fracture damage microscopically. The nucleation and growth sequence of the ring cracks is illustrated in Figure 10. The surface ring cracks grew in depth into cone cracks starting at approximately 45° and veering toward the specimen surface at various angles up to about 75° from the vertical. At higher impact velocities, additional cone cracks formed both inside and outside the main cone crack, and the innermost cone grew several millimeters in depth.

Figure 11 shows profiles of several cone cracks, essentially depicting a section view across the cone cracks of the area marked AA in Figures 10 and 11. Figure 11 also illustrates the surface profile of a radial crack and its interaction with the cone cracks. Cone cracks 1, 2, 3, (Figure 11) appeared first and grew independently of each other followed by the radial crack that intersected the first two cone cracks, reached the third cone, and then branched out. Newer cone cracks seemed to nucleate and grow in the presence of radial cracks, and their growth was often interrupted (cone crack 4 in Figure 11).

Under increasingly severe impacts, Figure 12, cone cracks seemed to cease growing; instead, new types of cracks were created. There were profiles of what appeared to be lateral cracks that nucleated near the contact center, ran approximately parallel to, and eventually veered sharply toward the specimen free surface. There were also vertical cracks that initiated from inside the innermost cone and converged to the damage center as successive sections were examined. We speculate that these are penny-shaped cracks similar to the median-vent cracks observed by Evans and Wilshaw in their quasi-static indentation experiments.[5] A zone of damage-induced porous material, approximately spherical

23
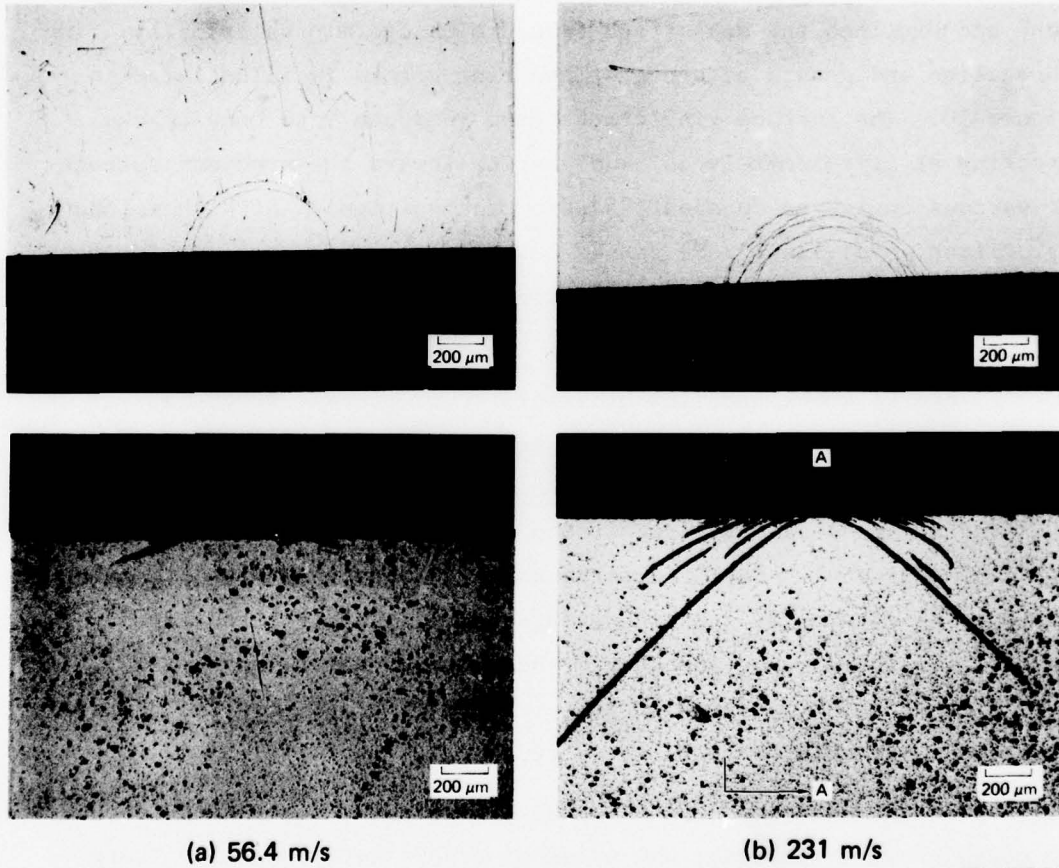
(a) 56.4 m/s             (b) 231 m/s

MP-4928-38

FIGURE 10  SECTIONAL VIEWS SHOWING SUBSURFACE GROWTH OF RING CRACKS INTO
CONE CRACKS IN HP $Si_3N_4$ (Particles: 2.4-mm-Diameter Steel Spheres)

24

RING AND CONE CRACKS

200 μm

RADIAL CRACK

A      A



1
2

RADIAL CRACK

4    3

CONE CRACK

200 μm
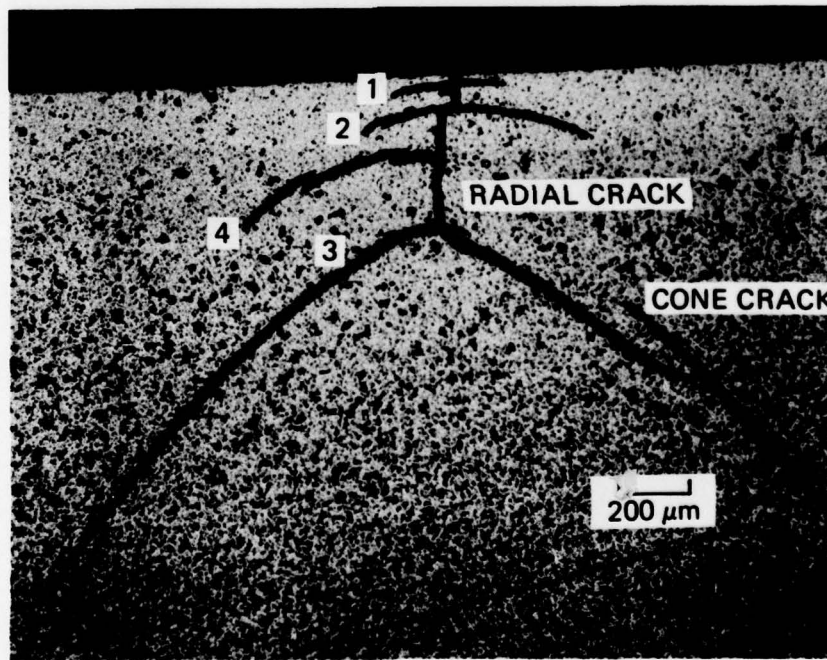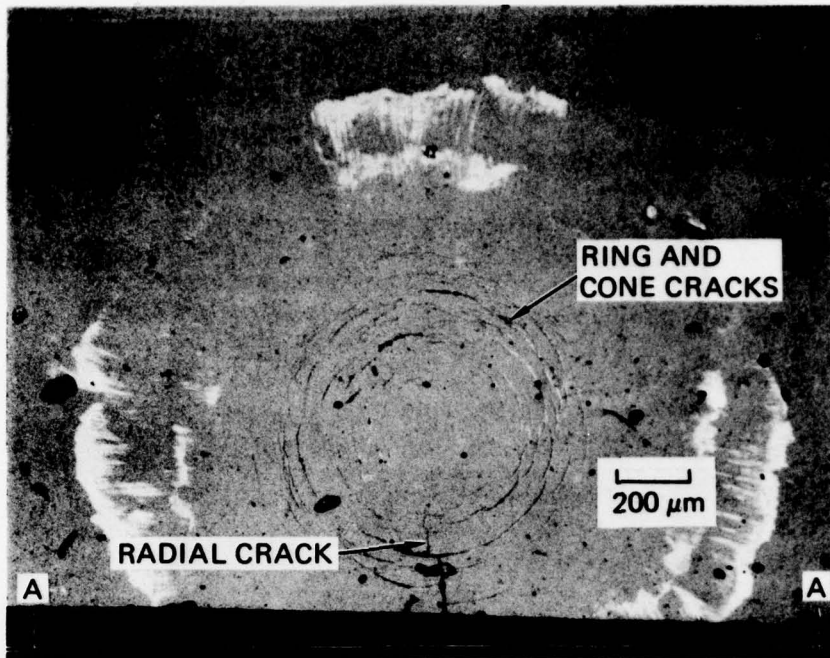
299 m/s

MP-4928-39

FIGURE 11   SECTIONAL VIEW OF SEVERAL CONE CRACKS AND ONE RADIAL CRACK 0.50 mm FROM CONTACT CENTER

Note the interaction between cone and radial cracks. Particle: steel, 2.4 mm; Target: HP $Si_3N_4$

25

RING AND
CONE CRACKS

RADIAL CRACK

200 μm

RADIAL
CRACK

LATERAL
CRACK

MEDIAN-VENT
CRACK

CONE
CRACK

200 μm
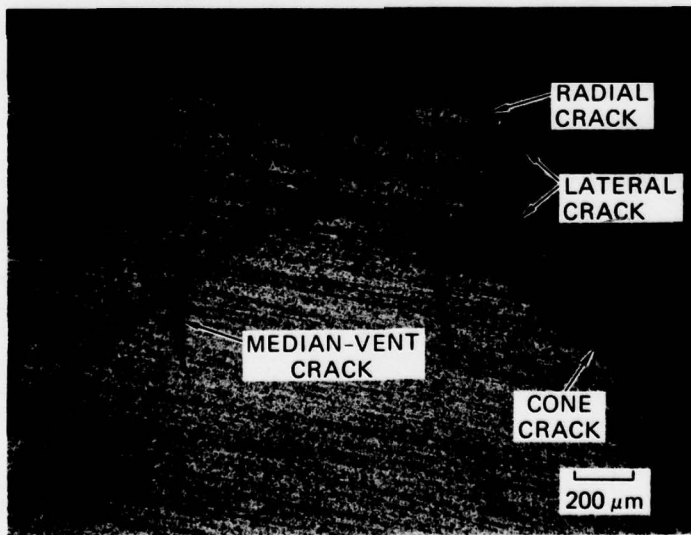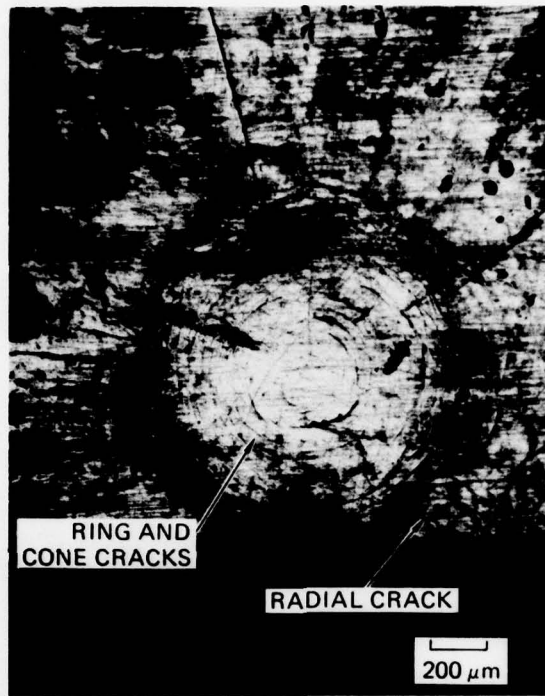
(a) 0.60 mm FROM CONTACT CENTER

MP-4928-40

FIGURE 12    SECTIONAL VIEW OF SEVERAL TYPES OF CRACKS IN HP Si$_3$N$_4$ IMPACTED
AT 231 m/s BY A 2.4-mm-DIAMETER WC SPHERE

26
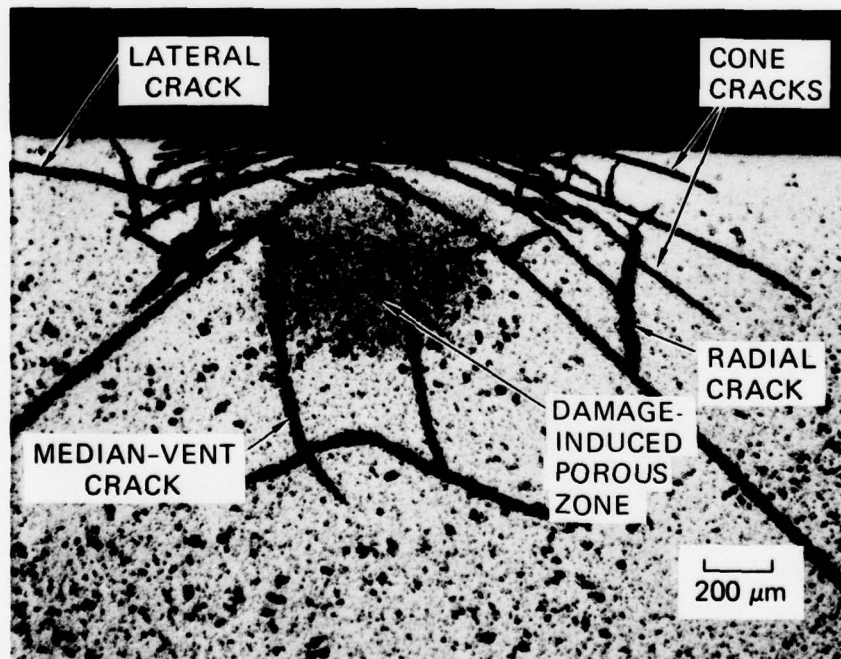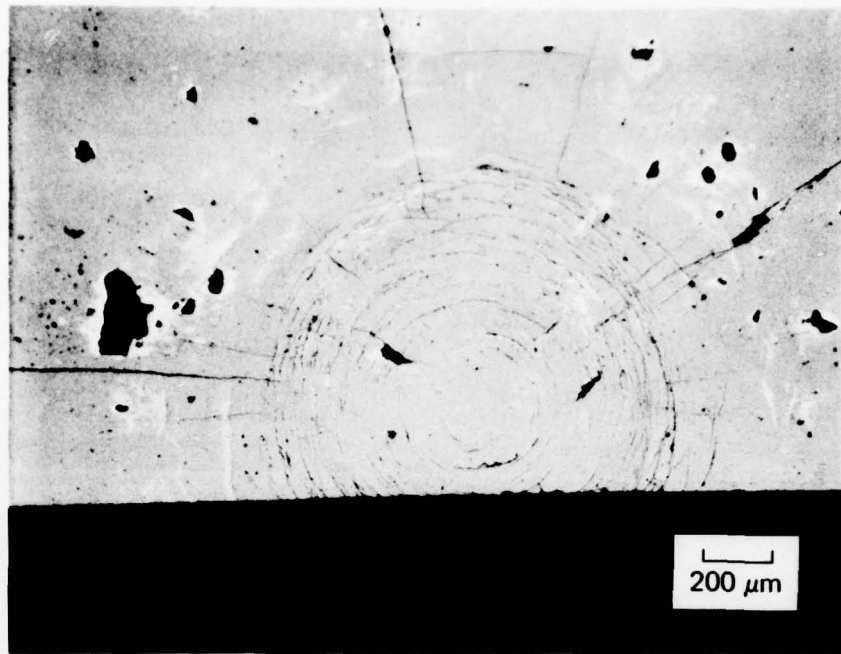
(b) 0.25 mm FROM CONTACT CENTER

MP-4928-41

FIGURE 12   SECTIONAL VIEW OF SEVERAL TYPES OF CRACKS IN HP Si$_3$N$_4$ IMPACTED
AT 231 m/s BY A 2.4-mm-DIAMETER WC SPHERE  (Continued)

27
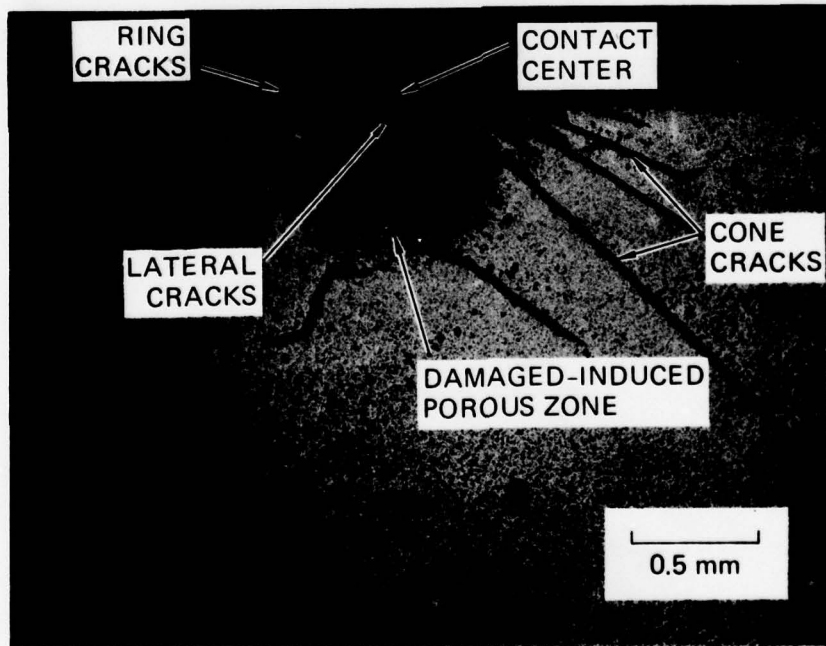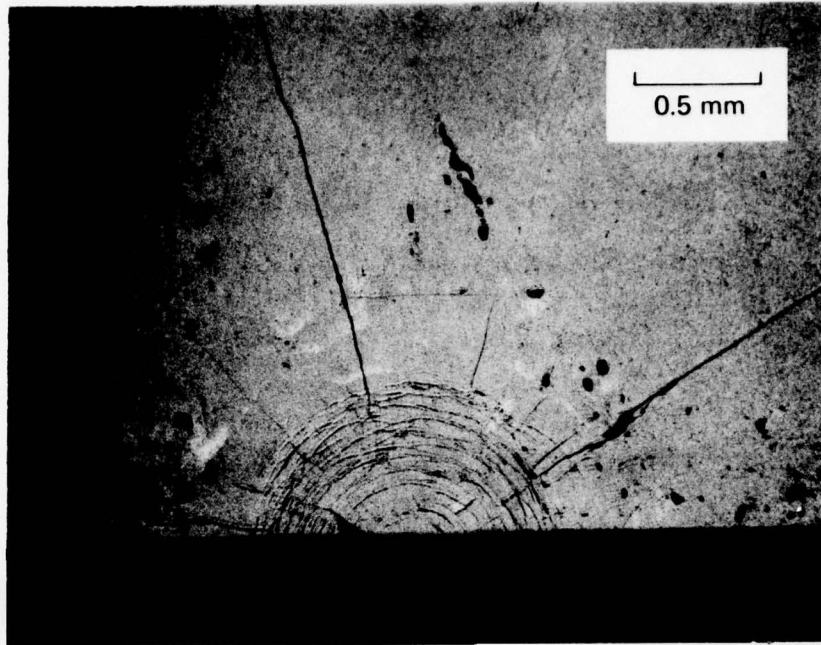
(c) AT CONTACT CENTER

MP–4928–42

FIGURE 12   SECTIONAL VIEW OF SEVERAL TYPES OF CRACKS IN HP $Si_3N_4$ IMPACTED
AT 231 m/s BY A 2.4-mm-DIAMETER WC SPHERE  (Continued)

28
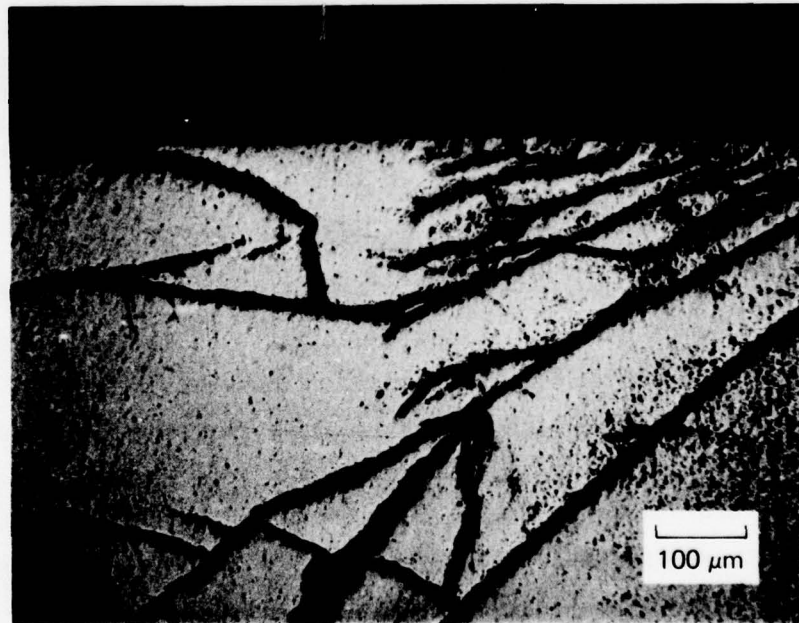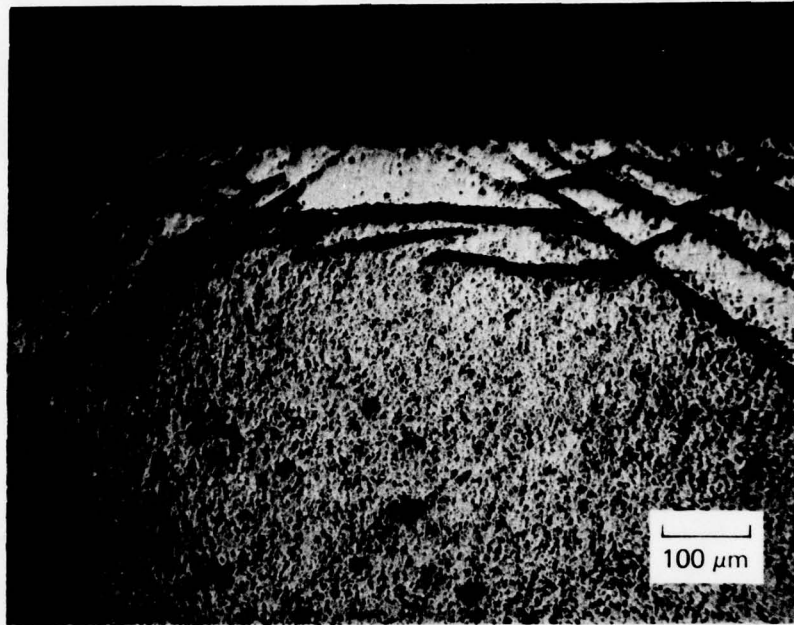
(d) MAGNIFIED VIEWS OF DAMAGE-INDUCED POROUS
ZONE BENEATH CONTACT CENTER

MP-4928-74

FIGURE 12   SECTIONAL VIEW OF SEVERAL TYPES OF CRACKS IN HP $Si_3N_4$ IMPACTED
AT 231 m/s BY A 2.4-mm-DIAMETER WC SPHERE   (Concluded)

29

in shape, was also observed beneath the contact area, Figure 12(b) and
(c). High-magnification photographs give detail of this porous zone
in Figure 12(d). Zinc sulfide impacted by 0.4- and 0.8-mm-diameter WC
spheres exhibited a similar porous zone.[1,6] The failure mechanism
responsible for this porous zone is not clearly understood.

Figures 6 and 7 compare impact damage at 231 m/s by spheres of
steel and WC. The surface and subsurface damage by the WC sphere is
significantly greater.

The foregoing preliminary fractographic observations provide
several qualitative conclusions:

- While larger particles produced larger damage zones and cracks,
  the fracture-damage morphology produced by the 2.4-mm-diameter
  and 1.6-mm-diameter WC spheres was qualitatively similar.

- The cracking sequence produced by the WC spheres consisted of
  surface ring cracks with associated cone cracks followed by
  plastic deformation and radial cracks, lateral cracks, and
  median-vent cracks. There were strong interactions between
  these different types of cracks.

- For a similar range of velocity, the softer steel spheres
  produced only ring cracks, some of which grew into cone cracks.
  Complete fragmentation of the steel sphere at 299 m/s and
  little increase in target damage above 299 m/s indicated the
  inability of the steel spheres to produce other types of
  damage.

## Reaction Bonded Silicon Nitride

### Summary of Particle Impact Experiments

We performed 18 particle impact experiments on RB $Si_3N_4$ with
particles of two sizes (1.6 and 0.4 mm in diameter), one particle/target
combination (WC sphere/RB $Si_3N_4$ target), and a range of impact velocities
(11.3 to 700 m/s). The experiments were conducted to obtain a wide
range of fracture damage in RB $Si_3N_4$ to investigate the influences of
impact velocity and particle size on the damage. The results could also
be compared with those obtained for HP $Si_3N_4$ under similar impact
conditions.

Fourteen impacts were carried out on RB $Si_3N_4$ using the 1.6-mm-
diameter WC spheres ranging in impact velocity from 11.3 to 72.6 m/s.

It was discovered during the experiments that low velocities were sufficient for the 1.6-mm-diameter WC spheres to cause substantial damage in the RB $Si_3N_4$. The 2.4-mm-diameter WC spheres were not used for similar experiments because it was expected that even lower velocities would be adequate to cause severe damage and the information would be less useful. We decided to conduct several experiments in which submillimeter WC spheres were used to raise the impact velocities to a damage level more representative of erosion conditions. Four experiments were performed using a 0.4-mm-diameter WC sphere with impact velocities ranging from 310 to 700 m/s. Table 2 summarizes the important details of these tests.

### Fractographic Observations

Typical scanning electron micrographs of the RB $Si_3N_4$ specimens are presented in Figures 13 through 15. The SEM gave a better resolution to the various damage features than the optical microscope because the large population of dark pores did not reflect light very well when an optical microscope was used.

The damage characteristics found for the RB material were similar to those for the HP material described earlier, although much lower velocities were necessary to cause equivalent damage in the RB material. Observable damage features included ring and cone cracks followed, as impact velocity increased, by a plastic impression; radial, lateral, and median-vent cracks; material removal; and target failure. Plastic impressions were deeper for impacts with the 0.4-mm-diameter spheres (Figure 14). Ring cracks were visible at the bottom of the craters. These ring cracks formed earlier in the impact process, but their surface profile later became closed or healed by the increased compressive stress field and significant plastic flow in the target.

Test 17, Figure 14(c) shows surface interaction of the lateral cracks. They are approximately planar cracks that ran almost parallel to and eventually intersected with the specimen free surface, causing portions of the material between adjacent radial cracks to be removed from the impact site. Test 18, Figure 14(d), performed at about 700 m/s,

31

## Table 2

### PARTICLE IMPACT EXPERIMENTS ON REACTION BONDED SILICON NITRIDE

| Test No. | SRI No. | Impact Velocity (m/s) | Rebound Velocity (m/s) | Damage to Particle |
|----------|---------|-----------------------|------------------------|--------------------|
| Impact configuration D (1.60-mm-diameter steel, RB $Si_3N_4$) | | | | |
| 1 | 4928-76 | 11.3 | 11.5[a] | Intact |
| 2 | 4928-75 | 12.7 | 12.6 | b |
| 3 | 4928-74 | 15.9 | 15.4 | Intact |
| 4 | 4928-70 | 16.9 | 16.8 | Intact |
| 5 | 4928-73 | 18.1 | 20 | Intact |
| 6 | 4928-72 | 24.2 | 27 | b |
| 7 | 4928-78 | 30 | 34 | Intact |
| 8 | 4928-71 | 31.7 | 33 | Intact |
| 9 | 4928-83 | 46.2 | 44 | Intact |
| 10 | 4928-85 | 48 | 46 | b |
| 11 | 4928-82 | 48.4 | 43 | b |
| 12 | 4928-81 | 58.4 | 50 | b |
| 13 | 4928-80 | 65.7 | 56 | b |
| 14 | 4928-79 | 72.6 | 58 | b |
| Impact configuration E (0.40-mm-diameter WC, RB $Si_3N_4$) | | | | |
| Impact configuration E WC-0.40/RB $Si_3N_4$ | | | | |
| 15 | 4928-52 | 310 | c | b |
| 16 | 4928-50 | 356 | c | b |
| 17 | 4928-49 | 506 | c | b |
| 18 | 4928-54 | 700 | c | b |

---

[a] Higher rebound velocities indicate increased error in measurements of low velocities (estimated at $\pm$ 5%).

[b] Particles were not recovered or no signals from fragments.

[c] Rebound velocity not available or particle fragmented.

32
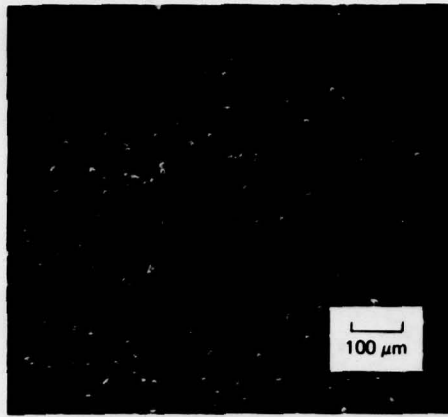
(a) 11.3 m/s
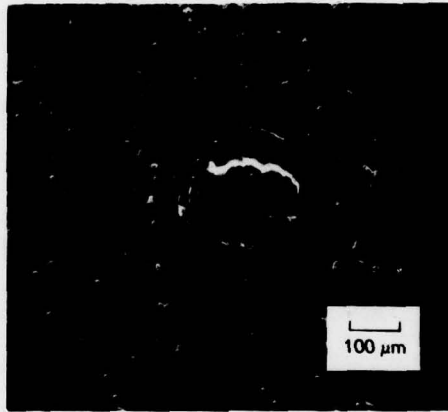
(b) 18.1 m/s
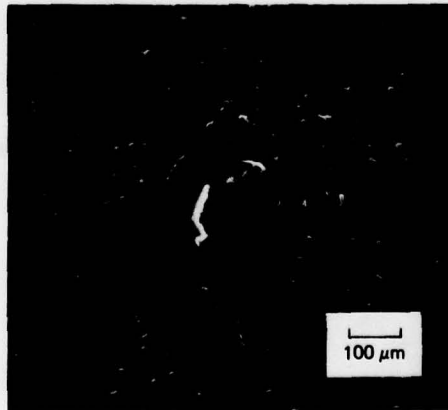
(c) 24.2 m/s

MP–4928–43

FIGURE 13   TYPICAL IMPACT DAMAGE IN RB $Si_3N_4$ BY 1.6-mm-DIAMETER WC SPHERES
(Impact Configuration D)

33
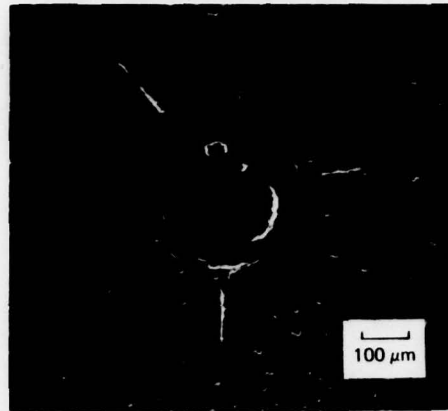
(d) 30 m/s
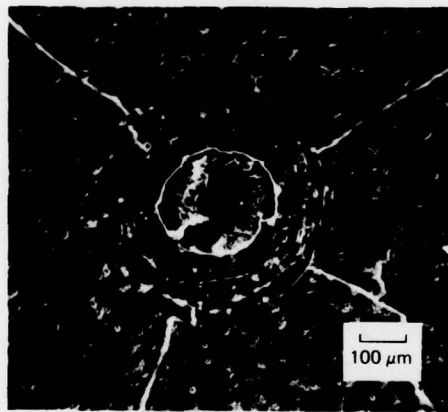
(e) 46.2 m/s
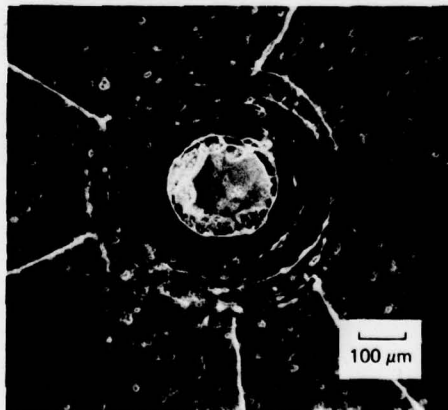
(f) 48.4 m/s

MP-4928-44

FIGURE 13    TYPICAL IMPACT DAMAGE IN RB Si$_3$N$_4$ BY 1.6-mm-DIAMETER WC SPHERES
(Impact Configuration D)  (Concluded)

34
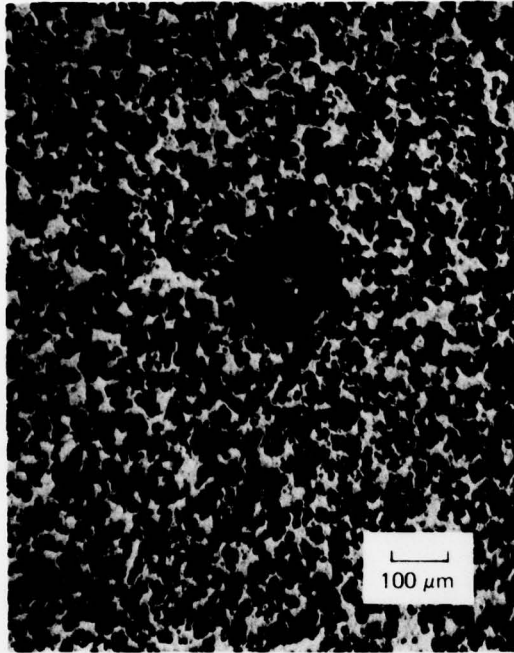
(a) 310 m/s
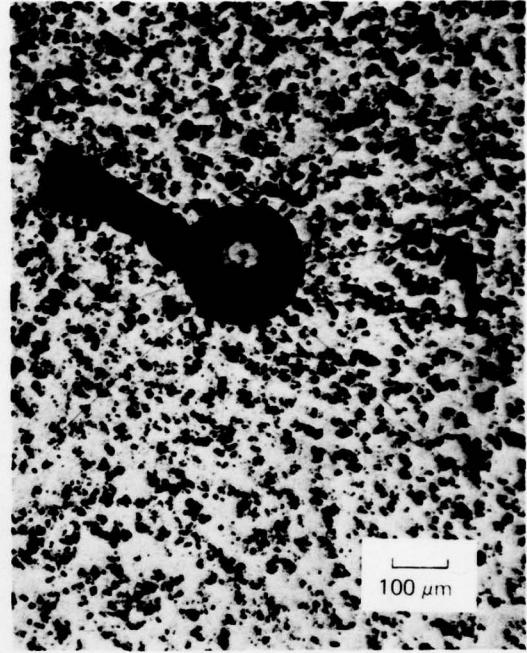
(c) 506 m/s
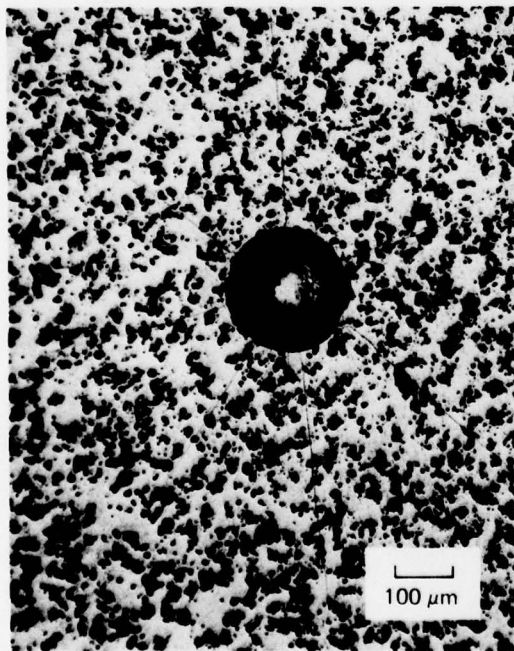
(b) 356 m/s

(d) 700 m/s

MP–4928–45

FIGURE 14    TYPICAL IMPACT DAMAGE IN RB Si$_3$N$_4$ BY 0.4-mm-DIAMETER WC SPHERES
(Impact Configuration E)

35
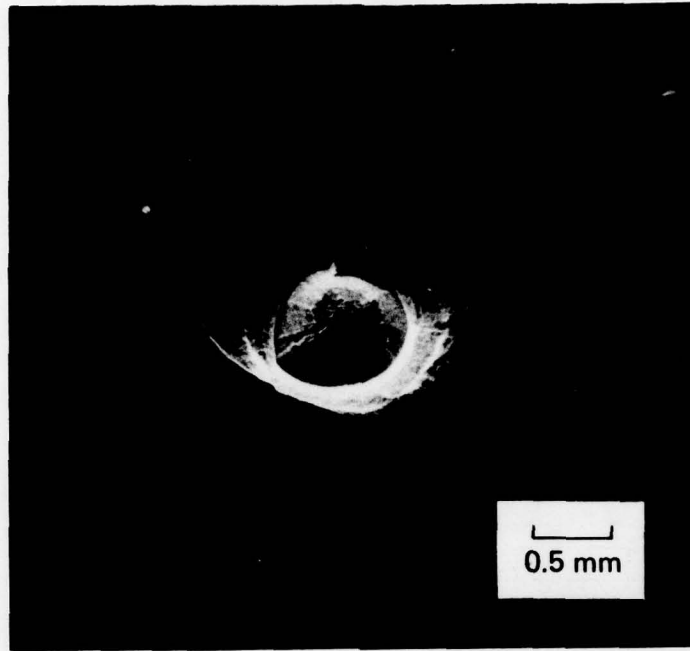
(a) 58.4 m/s
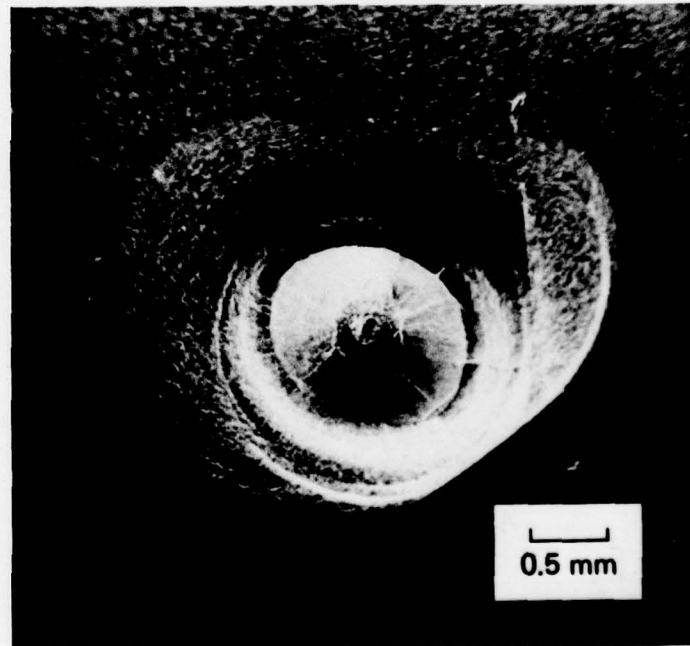


(b) 65.7 m/s

MP–4928–46

FIGURE 15   SEVERE SURFACE DAMAGE IN RB $Si_3N_4$ IMPACTED BY 1.6-mm-DIAMETER WC
SPHERES AT VELOCITIES SLIGHTLY HIGHER THAN THOSE IN FIGURE 13

shows increased material rem·.al and reveals the subsurface profile of several lateral cracks. Test 12 and 13 (Figure 15) indicate a more severe case of surface damage in RB $Si_3N_4$ by larger-size particles (1.6-mm in diameter) when impact velocities were increased only slightly (58-65 m/s) from impacts shown in Figure 13. Profiles of both cone and lateral cracks are visible in the craters. Interactions of these two types of cracks produced surface fracture and material removal.

## Oxidized Hot Pressed Silicon Nitride

### Summary of Particle Impact Experiments

We performed 16 experiments in which HP $Si_3N_4$ specimens covered with a layer of oxide scale approximately 20 μm thick were impacted with 2.4-mm-diameter WC spheres (impact configuration F) at 13.4 to 196 m/s. The experiments were performed to investigate the fracture behavior of the oxide scale and the effect of the oxide scale on the fracture response of the underlying HP $Si_3N_4$. Table 3 lists these experiments.

### Fractographic Observations

Typical scanning electron micrographs of the oxidized specimens impacted at various velocities by the 2.4-mm-diameter WC spheres are shown in Figure 16. The unpolished rugged and porous oxide scale did not reflect light very well. The SEM was therefore used to better resolve the various damage details. Damage features observed on the oxide scale included local spallation, ring cracks, and scattered radial fractures. The spallations at low velocities (13.4-50.8 m/s) were rather small. As the impact velocity was raised, the spalled area broadened and ring cracks formed in the crater. Radial fractures were observed in tests at high velocities (> 72.5 m/s), appearing as small spalled areas (arrowed in Figure 16) scattered around the rim of the crater. The mechanism that controlled the formation of these radial fractures may be linked with the same mechanism that initiated and extended the radial cracks observed in the underlying host material.

37

## Table 3

### PARTICLE IMPACT EXPERIMENTS ON OXIDIZED HOT PRESSED SILICON NITRIDE

| Test No. | SRI No. | Impact Velocity (m/s) | Rebound Velocity (m/s) | Damage to Particle |
|---|---|---|---|---|
| Impact configuration F<br>(2.40-mm-diameter WC, oxidized HP Si$_3$N$_4$) | | | | |
| 1 | 4928-145 | 13.4 | a | Intact |
| 2 | 4928-143 | 14.5 | a | b |
| 3 | 4928-142 | 16.9 | 18.5[c] | Intact |
| 4 | 4928-144 | 25.4 | 24 | Intact |
| 5 | 4928-148 | 34.3 | a | b |
| 6 | • 4928-147 | 46.2 | 31 | Flattened |
| 7 | 4928-146 | 50.8 | 39 | Flattened |
| 8 | 4928-150 | 72.6 | 42 | b |
| 9 | 4928-149 | 72.6 | 29 | Fragmentation[d] |
| 10 | 4928-141 | 82 | 29 | Fragmentation[d] |
| 11 | 4928-140 | 84.7 | a | b |
| 12 | 4928-139 | 113 | a | Fragmentation[d] |
| 13 | 4928-138 | 145 | a | Fragmentation[d] |
| 14 | 4928-135 | ∼150 | a | b |
| 15 | 4928-136 | 169 | a | Fragmentation[d] |
| 16 | 4928-137 | 169 | a | Fragmentation[d] |

[a] Rebound velocity not available or particle fragmented.

[b] Particles were not recovered or no signals from fragments.

[c] Higher rebound velocity indicates increased error in measurement of low velocities (estimated at $\pm$ 5%).

[d] Determined from photomultiplier signals of rebounded fragments.

(a) 13.4 m/s　　　　(b) 34.3 m/s　　　　(c) 46.2 m/s
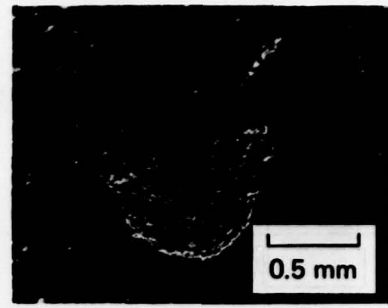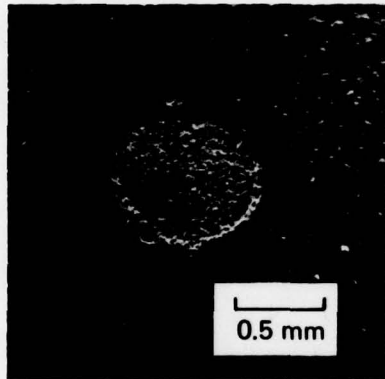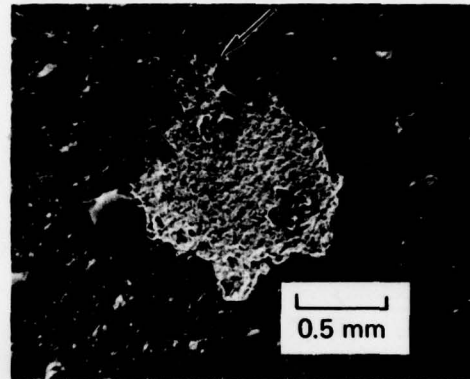
(d) 50.8 m/s　　　　(e) 72.6 m/s
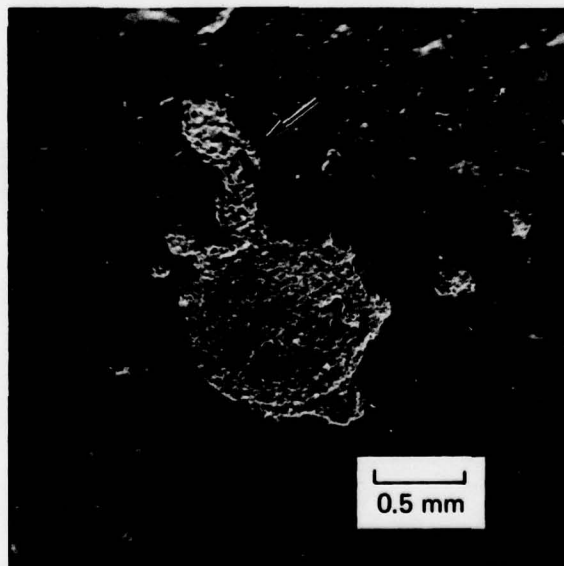
(f) 82 m/s

MP-4928-47

FIGURE 16　TYPICAL IMPACT DAMAGE IN OXIDIZED HP $Si_3N_4$ BY 2.4-mm-DIAMETER WC SPHERES (Impact Configuration F)

Arrows point to radial fractures.

39
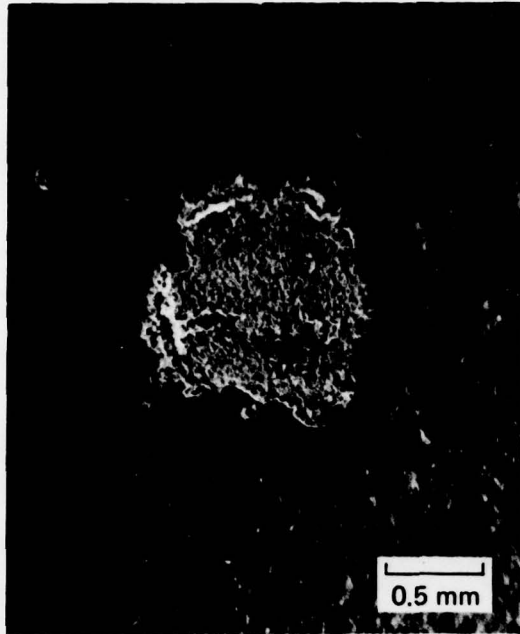
(g) 84.7 m/s        (i) 150 m/s
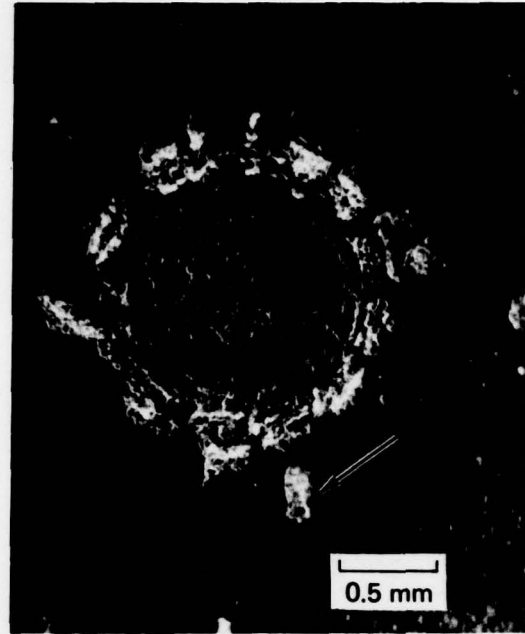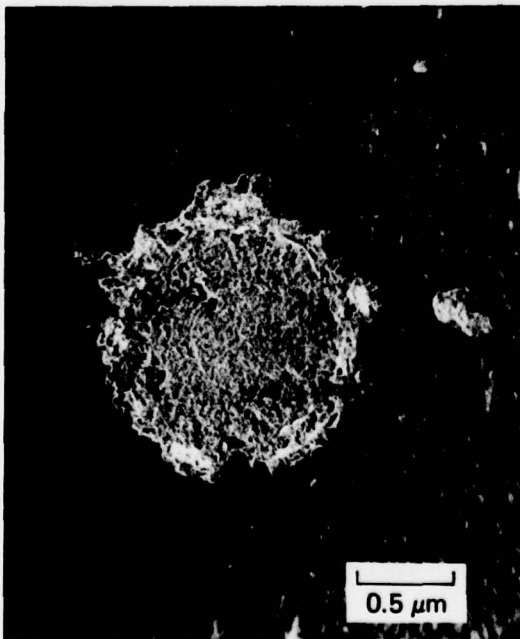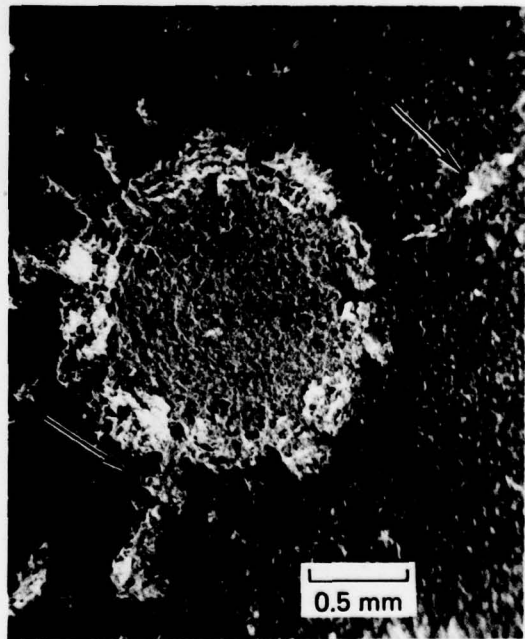
(h) 113 m/s        (j) 169 m/s

MP4928-48

FIGURE 16    TYPICAL IMPACT DAMAGE IN OXIDIZED HP $Si_3N_4$ BY 2.4-mm-DIAMETER WC
SPHERES (Impact Configuration F)

Arrows point to radial fractures. (Concluded)

40

To determine internal damage in the oxide layer and in the host material, we removed successive layers of the oxide scale from the surface of the specimens. For test 14 at 150 m/s, the damage observed at different depths is illustrated in Figure 17. In the crater area where the impact spalled the specimen free of oxide material, the damage revealed was that sustained in the host material as shown by all four pictures in Figure 17, where a pattern of ring cracks was observed. Outside the crater zone, as successive layers of the oxide scale were removed by polishing (Figure 17a to c), no cracking was observed in the oxide. This was not surprising because the oxide scale was highly porous.

When the oxide layer was completely removed by polishing, Figure 17d, we observed damage in the substrate that consisted of ring cracks as well as radial cracks. Figure 18 illustrates substrate damage in different tests as a function of impact velocity. Surface damage to the oxide scale and to the HP $Si_3N_4$ substrate can be compared by comparing Figures 16 and 18.

The cracking sequence in the HP $Si_3N_4$ substrate was similar to that observed for the unoxidized material under similar impact conditions (compare Figures 7 and 18). The crack size distributions are compared quantitatively in Section VII.

(a) SURFACE

(c) ~ 15 μm BELOW SURFACE
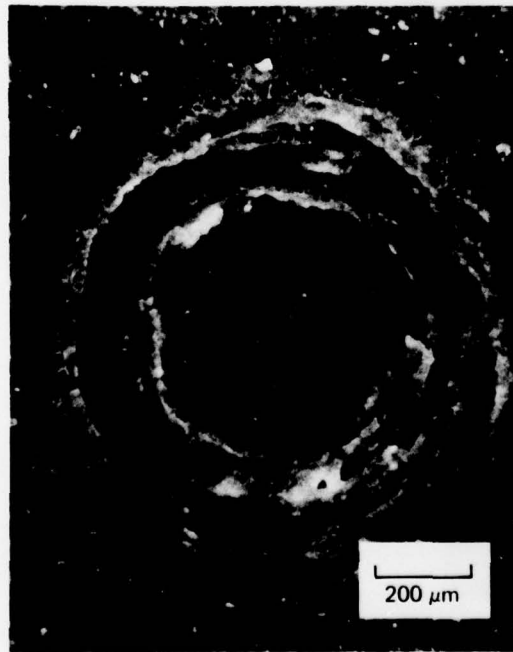
(b) ~ 8 μm BELOW SURFACE
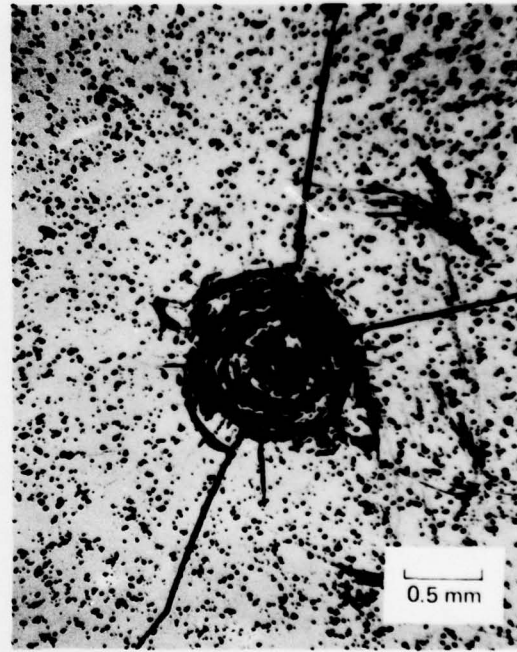
(d) OXIDE SCALE COMPLETELY
REMOVED

MP-4928-49

FIGURE 17   IMPACT DAMAGE VIEWED AT SUCCESSIVE DEPTHS (Oxidized HP $Si_3N_4$ Impacted at 150 m/s with a 2.4-mm-Diameter WC Sphere)

42

THIS PAGE INTENTIONALLY LEFT BLANK
TO ACCOMMODATE FIGURE 18 BEING ON FACING PAGES.
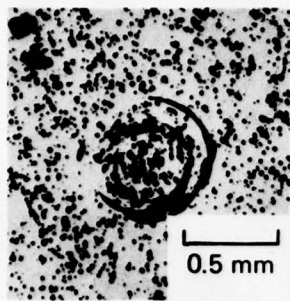
(a) 13.4 m/s      (b) 34.3 m/s      (c) 46.2 m/s
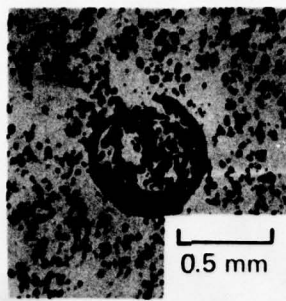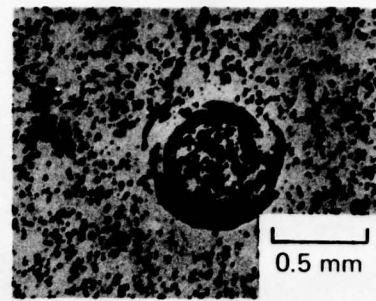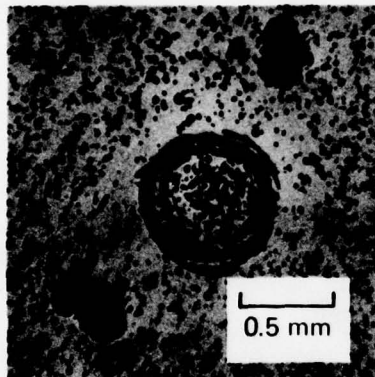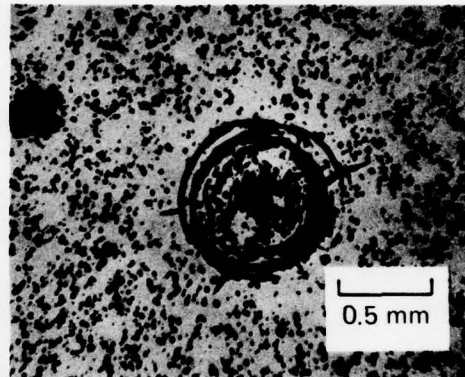
(d) 50.8 m/s      (e) 72.6 m/s
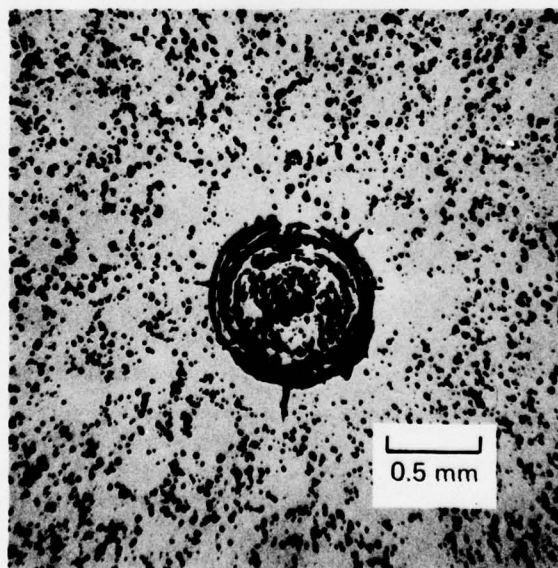
(f) 82 m/s

MP-4928-50

FIGURE 18   TYPICAL IMPACT DAMAGE IN HP Si$_3$N$_4$ SUBSTRATE (Beneath the Oxide Scale) BY 2.4-mm-DIAMETER WC SPHERES (Impact Configuration F)

44
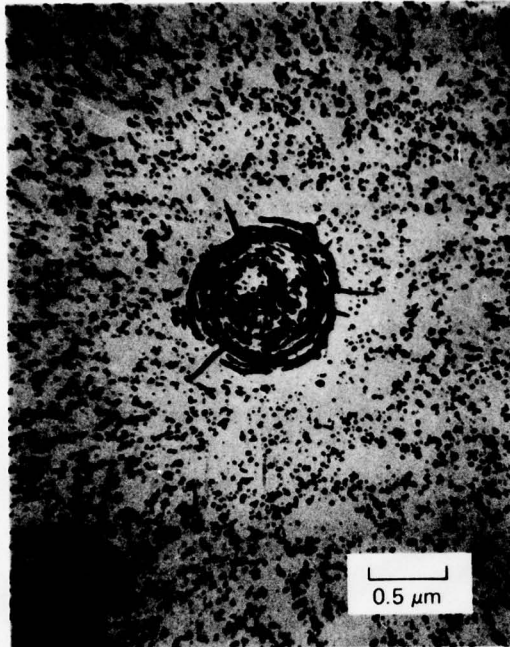
(g) 84.7 m/s
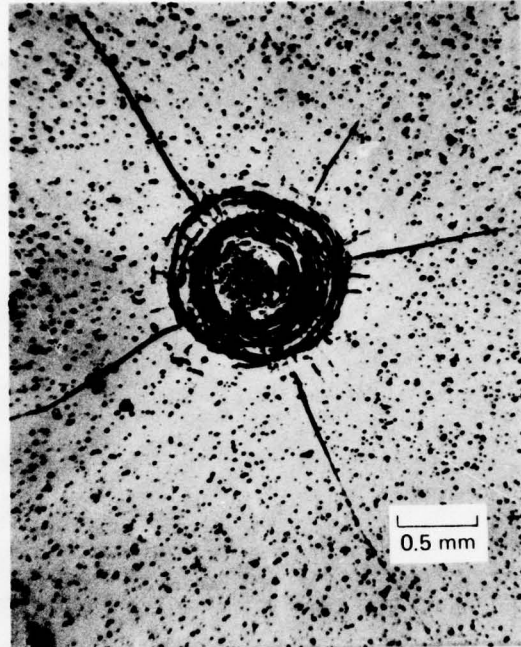
(i) 150 m/s
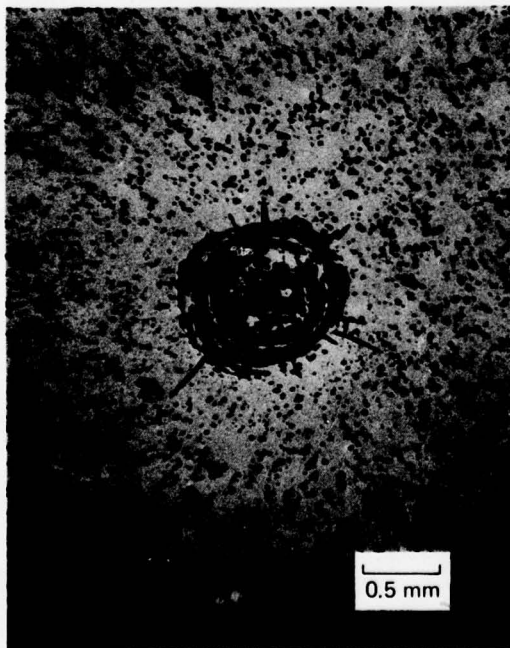
(h) 113 m/s
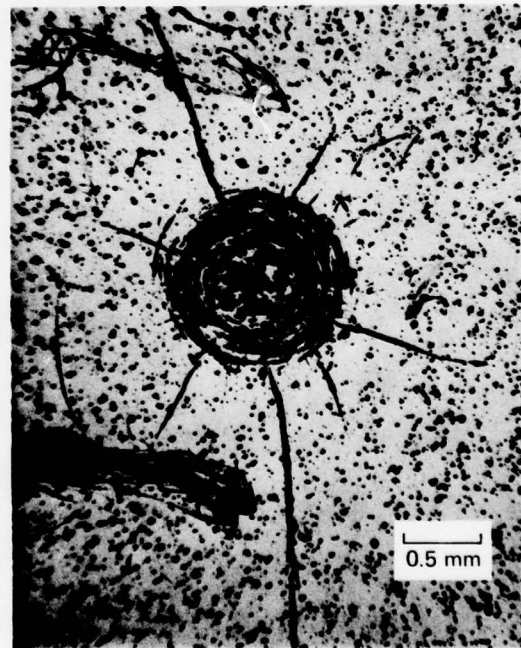
(j) 169 m/s

MP–4928–51

FIGURE 18   TYPICAL IMPACT DAMAGE IN HP $Si_3N_4$ SUBSTRATE (Beneath the Oxide Scale) BY
2.4-mm-DIAMETER WC SPHERES  (Impact Configuration F) (Concluded)

45

# IV  QUASI-STATIC INDENTATION EXPERIMENTS

The test fixture illustrated schematically in Figure 19 was used
for all quasi-static indentation experiments.  An Instron machine, model
TT-C-L, was used to apply the load continously during the test, and the
load was measured by a load cell located between the specimen and the
machine frame.  The WC sphere was press-fitted to a hardened-steel cone.
Since WC and $Si_3N_4$ were comparable in hardness, flattening of the WC
sphere was expected at high loads.  Indentations experiments were con-
ducted both in the load range where the sphere remained elastic and in
the range where the sphere began to deform plastically.  Similar experi-
ments were performed on oxidized HP $Si_3N_4$ specimens.

Eleven indentation experiments were performed on HP $Si_3N_4$ using a
2.4-mm-diameter WC sphere.  The critical load at which a single ring
crack first formed was recorded to be about 180 lb, and the load at
which the WC sphere began to flatten was approximately 550 lb.  Twelve
experiments were performed in which HP $Si_3N_4$ covered with a layer of
oxide scale was indented with a 2.4-mm-diameter WC sphere at 200 to
800 lb.  A small indent was first observed at about 150 lb, and the
ball began to deform plastically at about 550 lb.  The objectives of
these tests were to determine whether damage similar to that obtained
with particle impacts could be produced quasi-statically and to investi-
gate the effect of loading rate.  If damage similar to that caused by
particle impacts could be produced quasi-statically and the effect of
loading rate was negligible, indentation experiments would provide a
simpler means to study impact erosion behavior of the material.  Table
4 lists all the indentation experiments.

Optical micrographs of surface damage in HP $Si_3N_4$ specimens
indented at various loads by the 2.4-mm-diameter WC spheres are presented
in Figure 20.  We observed the development of the ring cracks with
increasing load.  Above 500 lb the indenter began to flatten rapidly

47
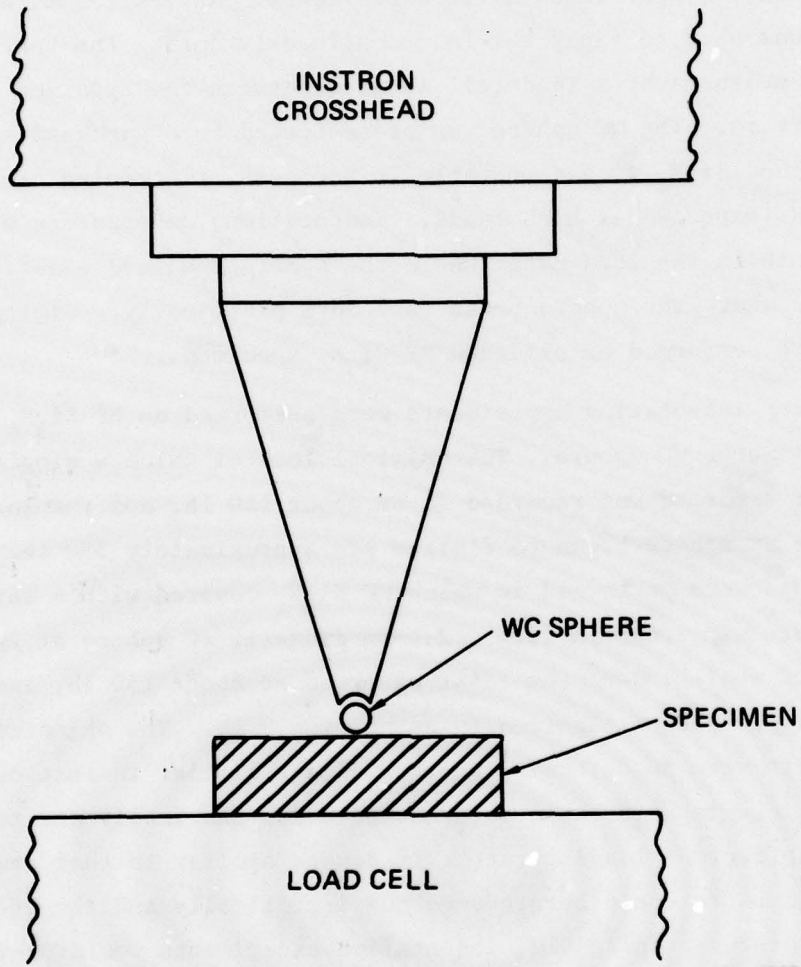
FIGURE 19   TEST FIXTURE FOR QUASI-STATIC INDENTATION EXPERIMENTS

## Table 4

## QUASI-STATIC INDENTATION EXPERIMENTS

| Test No. | SRI No. | Indentation Load (lb) | (N) | Damage to Indenter | Damage to Specimen |
|---|---|---|---|---|---|
| 2.40-mm-diameter WC, HP Si$_3$N$_4$ | | | | | |
| 1 | 4928-160 | 200 | (890) | Intact | |
| 2 | 4928-161 | 250 | (1112) | Intact | |
| 3 | 4928-162 | 300 | (1334) | Intact | |
| 4 | 4928-163 | 350 | (1557) | Intact | |
| 5 | 4928-164 | 400 | (1780) | Intact | |
| 6 | 4928-165 | 500 | (2224) | Intact | |
| 7 | 4928-166 | 500 | (2224) | Intact | |
| 8 | 4928-167 | 600 | (2669) | Flattened | |
| 9 | 4928-168 | 700 | (3114) | Flattened | |
| 10 | 4928-169 | 800 | (3558) | Flattened | |
| 11 | 4928-170 | 850 | (3781) | Flattened | |
| 2.40-mm-diameter WC, Oxidized HP Si$_3$N$_4$ | | | | | |
| 12 | 4928-171 | 50 | (222) | Intact | |
| 13 | 4928-172 | 100 | (444) | Intact | |
| 14 | 4928-173 | 150 | (667) | Intact | |
| 15 | 4928-174 | 200 | (890) | Intact | |
| 16 | 4928-175 | 250 | (1112) | Intact | |
| 17 | 4928-176 | 300 | (1334) | Intact | |
| 18 | 4928-177 | 350 | (1557) | Intact | |
| 19 | 4928-178 | 400 | (1780) | Intact | |
| 20 | 4928-179 | 500 | (2224) | Intact | |
| 21 | 4928-180 | 600 | (2669) | Flattened | |
| 22 | 4929-181 | 700 | (3114) | Flattened | |
| 23 | 4928-182 | 800 | (3558) | Flattened | |
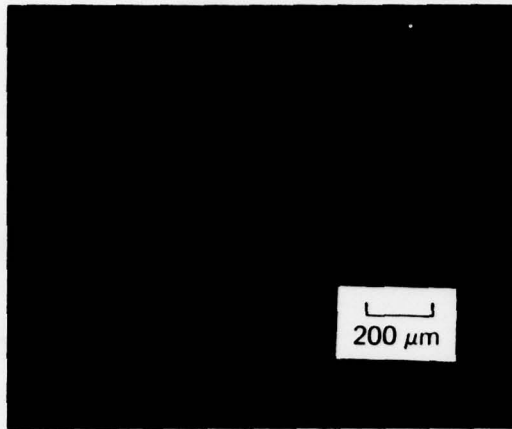
(a)  200 lb (890 N)
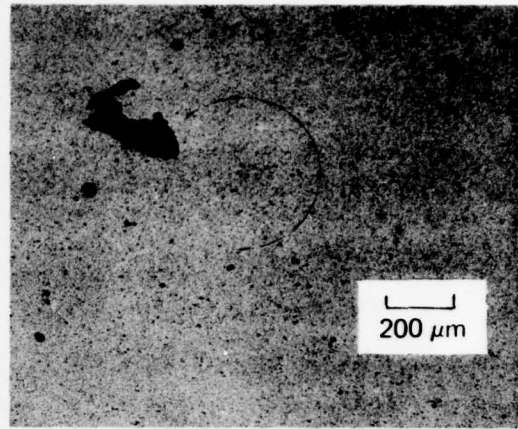
(d)  350 lb (1557 N)
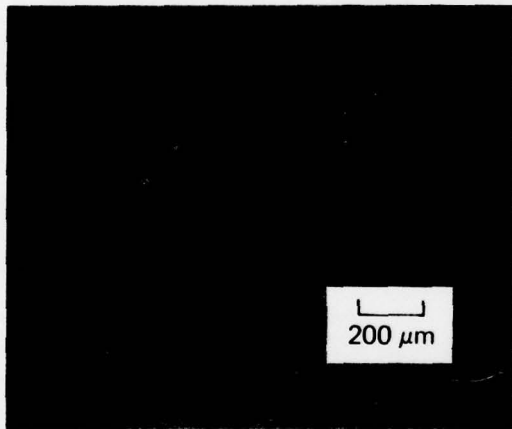
(b)  250 lb (1112 N)
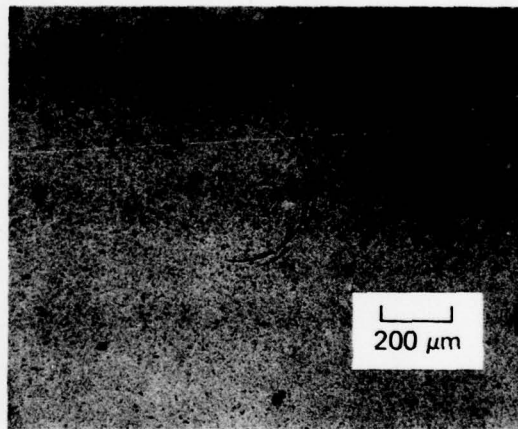
(e)  400 lb (1780 N)
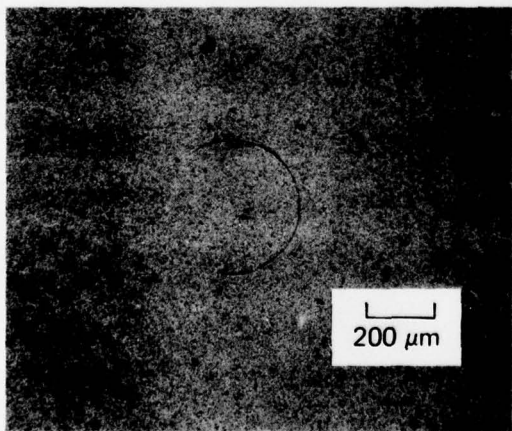
(c)  300 lb (1334 N)
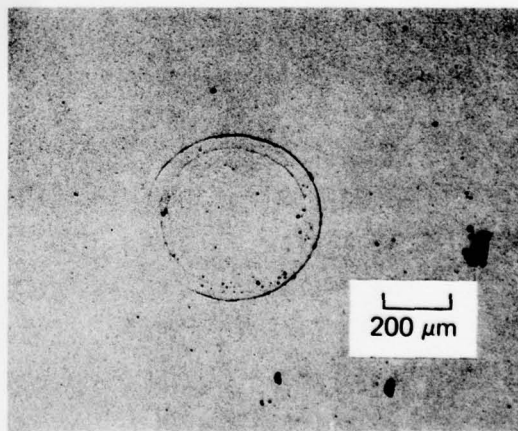
(f)  500 lb (2224 N)

MP-4928-53

FIGURE 20   TYPICAL QUASI-STATIC-INDENTATION DAMAGE IN HP $Si_3N_4$ BY 2.4-mm-DIAMETER
WC SPHERES

50

with load, and no further increase in specimen damage was observed. The results indicate that quasi-static particle contact produced incipient ring cracks but could not induce second-stage damage such as plastic impression and radial, lateral, and median-vent cracks similar to that sustained under impact conditions. At high loads the indenter deformed plastically and did not transfer the increase in load or pressure necessary for additional specimen damage. In particle impact experiments sufficiently high loads could be applied to the specimens by the impacting spheres for short durations.

Scanning electron micrographs of the oxide scale indented at three representative loads by the 2.4-mm-diameter WC sphere are shown in Figure 21. The scale broke off in a layer similar to local spallations by particle impacts at low velocities (Figure 16). There were no observable surface ring cracking or radial fractures produced quasi-statically. We conclude from these observations, without further analysis, that oxidized and unoxidized HP $Si_3N_4$ behaved similarly under quasi-static indentation, and that high levels of impact erosion damage can not be easily duplicated quasi-statically for silicon nitride because plastic deformation of the indenter prevents sufficient loads from being applied.
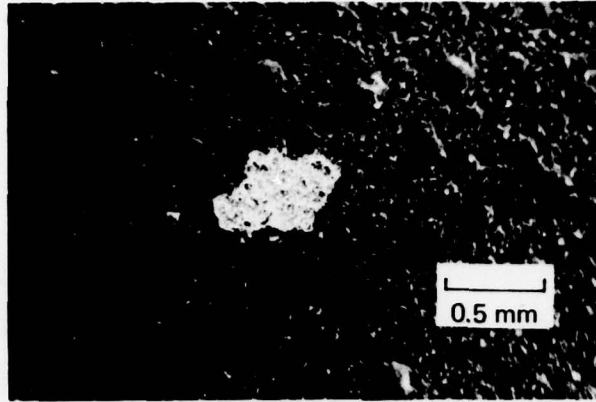
(a) 300 lb (1334 N)
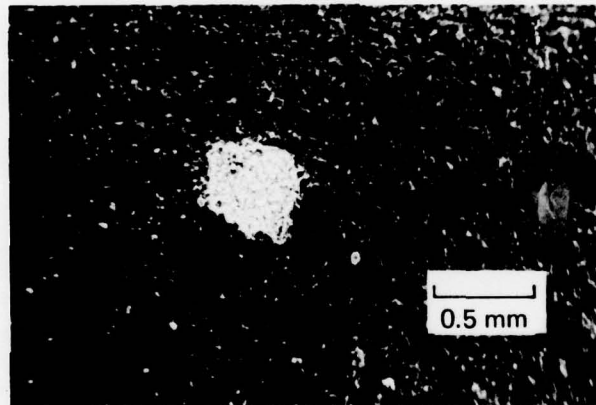
(b) 400 lb (1780 N)
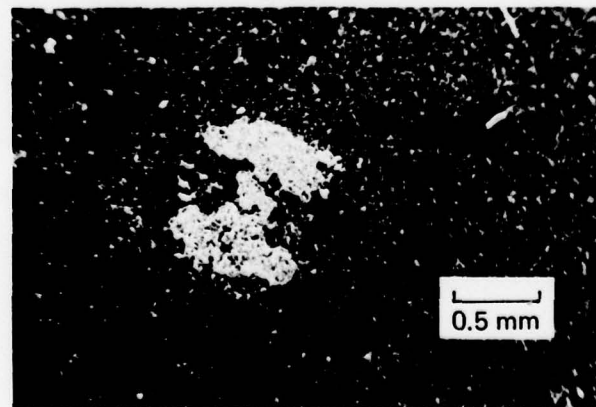
(c) 500 lb (2224 N)

MP-4928-54

FIGURE 21   TYPICAL QUASI-STATIC INDENTATION DAMAGE IN OXIDIZED HP $Si_3N_4$ BY
2.4-mm-DIAMETER WC SPHERES

52

# V PARTICLE IMPACT EXPERIMENTS AT HIGH TEMPERATURES

An electric furnace was used to heat the HP $Si_3N_4$ specimens to
1370°C (2500°F), a temperature representative of operating turbines.
The arrangement of the specimen in the furnace is illustrated in
Figure 22. The specimen temperature was measured by thermocouples.
The steady temperature was held for about 10 minutes, then the specimen
was impacted in situ. The impact velocities were measured by the
photomultipliers as described in Section III.

Two preliminary experiments at high temperatures were performed.
Figure 23 shows optical micrographs of surface damage in the HP $Si_3N_4$
specimens impacted by 2.4-mm-diameter steel spheres at 127 and 222 m/s
and at 1370°C. The specimen surface was lightly oxidized after a brief
heat-up time (about 1 hour) in the furnace and, therefore, did not show
any crack pattern. After the surface was lightly polished, a population
of ring cracks was visible in both specimens (Figure 24). The number
of ring cracks seemed to increase and newer ones formed closer to the
contact center for the impact at higher velocity, Figure 24(b). The
surface crack pattern was similar to that exhibited bv HP $Si_3N_4$ impacted
at room temperature at similar velocities, Figure 6(d) and (e).

To determine internal damage to HP $Si_3N_4$ impacted at 1370°C, we
sectioned the specimen shown in Figure 24(b) across the damage center.
No cone cracking was observed. This seems to indicate a deviation from
the room-temperature fracture process in which subsurface growth of
cone cracks with velocity was observed (Figure 10). More high-temperature
impacts are necessary to confirm these observations for any reliable
evaluation.
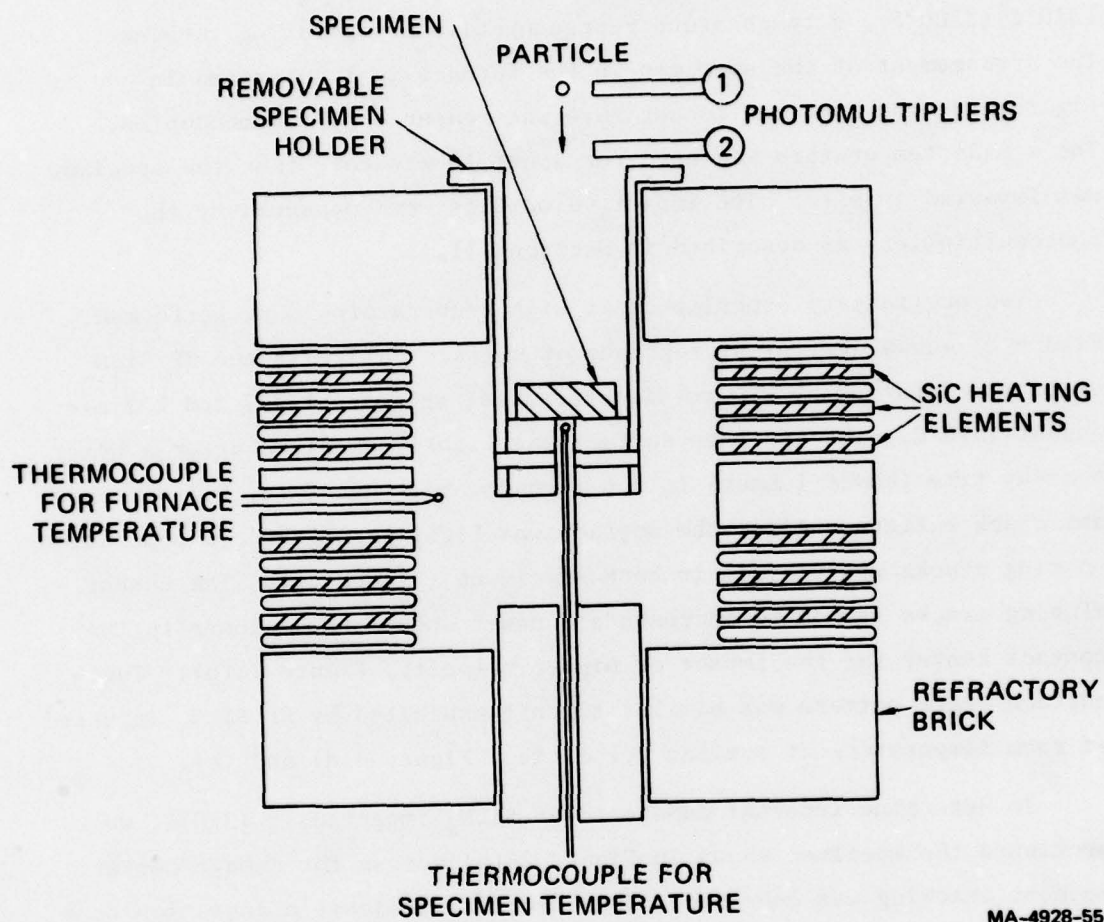
FIGURE 22    EXPERIMENTAL ARRANGEMENT FOR HIGH–TEMPERATURE PARTICLE-
IMPACT TESTS
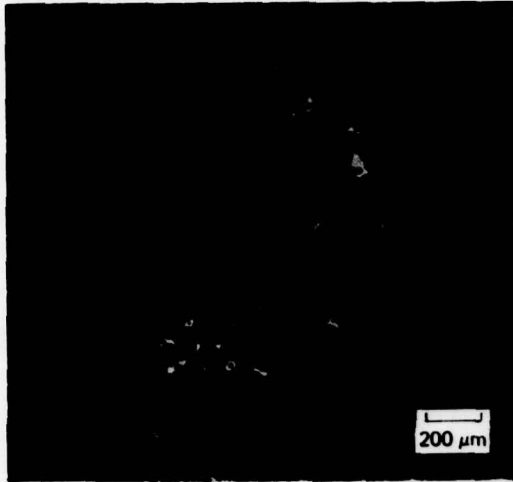
(a) 192 m/s
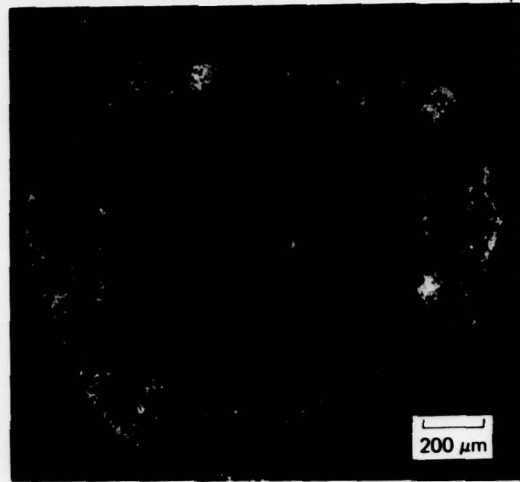
(b) 222 m/s

MP–4928–56

FIGURE 23    SURFACE DAMAGE IN HP Si$_3$N$_4$ HEATED TO 1370°C AND IMPACTED WITH
2.4-mm-DIAMETER STEEL SPHERES
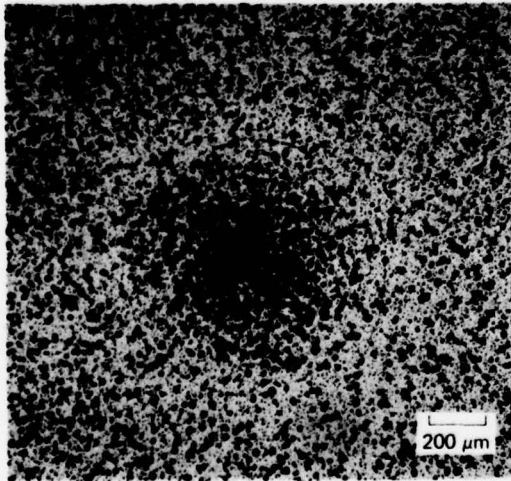


(a) 192 m/s
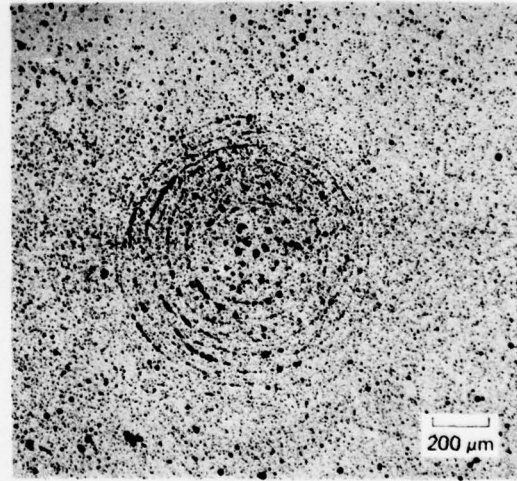
(b) 222 m/s

MP–4928–57

FIGURE 24    RING CRACKS THAT APPEARED AFTER THE SURFACES OF SPECIMENS IN FIGURE
23 WERE LIGHTLY POLISHED, SHOWING FRACTURE DAMAGE IN THE SUBSTRATE
BENEATH THE OXIDE

55

## VI   EFFECT OF MICROSTRUCTURE ON CRACK PROPAGATION

Ring cracks were produced in HP $Si_3N_4$ and in RB $Si_3N_4$ by quasi-static indentation and were examined by replica electron microscopy to determine whether the microstructure influenced crack propagation. Impressions were made with a 2.4-mm-diameter WC sphere using low loads to generate only a relatively small amount of damage in the form of partial ring cracks.   For HP $Si_3N_4$, it was found that the type of damage produced depended on surface preparation.   Ring cracks were seen only on unetched surfaces; plastic impressions with no ring cracks were formed on etched surfaces.   Such an effect could arise if thin oxide layers were produced during etching.   For the replica studies described here, impressions were made on polished surfaces, with very light etching following indentation.   Ring cracks produced dynamically were also examined to determine the effect of microstructure on crack propagation in particle impacts.

### Hot Pressed Silicon Nitride

In hot pressed $Si_3N_4$ the direction of the ring cracks is locally perturbed by the microstructure as illustrated in Figure 25(a).   The effect of the microstructure is significant since in some instances the cracks appear to be forced into a radial orientation that may cause them to stop or to form concentric segments of ring cracks as shown in Figure 25(b).   The general appearance of cracks indicates intergranular failure.   This can be seen more clearly in Figure 26, which also shows that intergranular microfracture occurs in the immediate vicinity of the main propagating crack.   These observations are important because they suggest that resistance to impact cracking might be improved by modifying the size and shape of the grains is hot pressed $Si_3N_4$.

(a)

MP-4928-75

FIGURE 25    TYPICAL RING CRACKS IN HP $Si_3N_4$ PRODUCED BY QUASI-STATIC INDENTATION

1 μm

(D)

MP-4928-76

FIGURE 25 TYPICAL RING CRACKS IN HP Si$_3$N$_4$ PRODUCED BY QUASI-STATIC
INDENTATION (Concluded)

59

1 μm
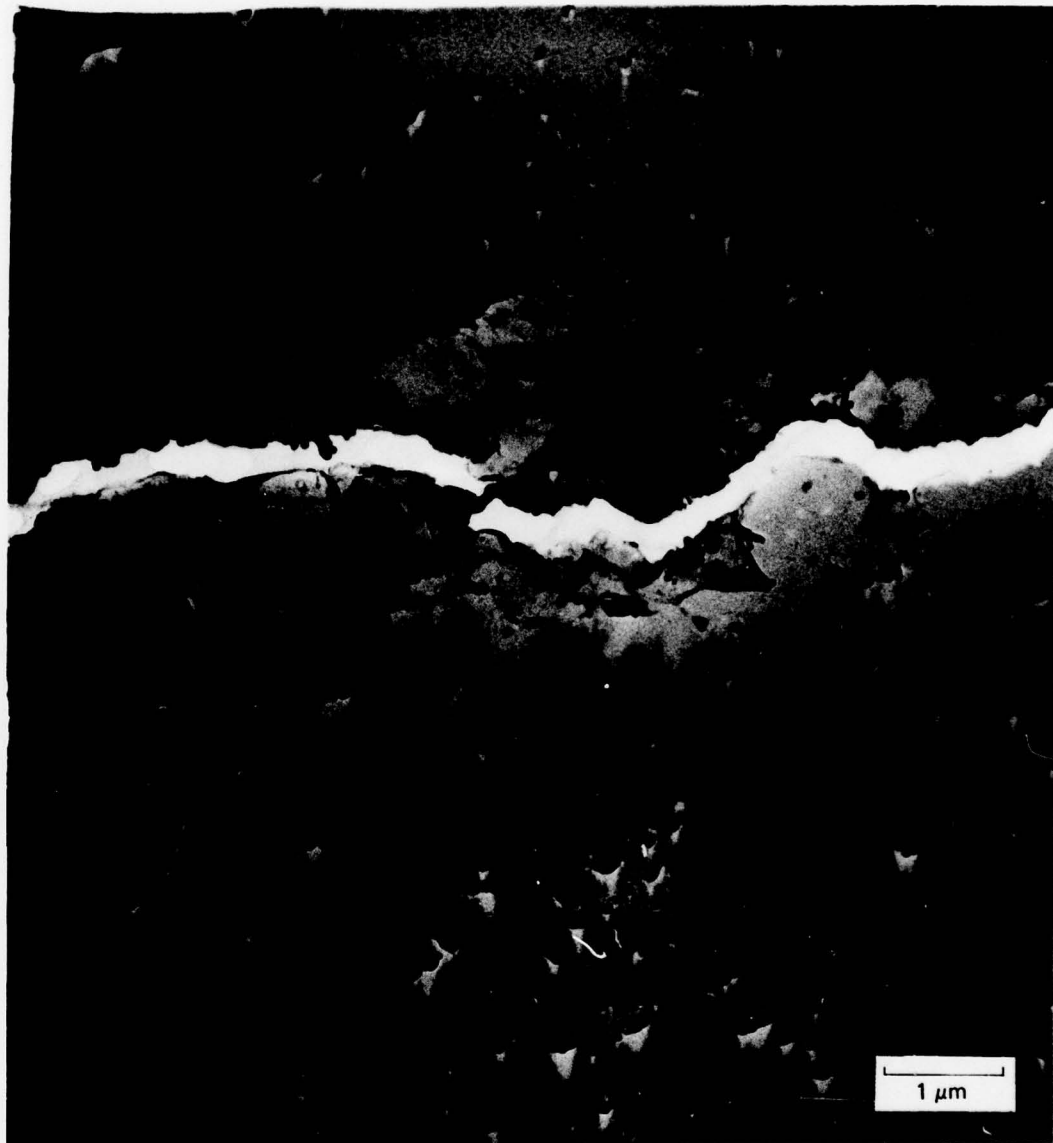
MP-4928-77

FIGURE 26    INTERGRANULAR PROPAGATION OF A RING CRACK IN HP Si$_3$N$_4$

60

## Reaction Bonded Silicon Nitride

Examples of ring cracks in RB $Si_3N_4$ are shown in Figures 27 through 29. The ring cracks follow the imposed Hertzian stress field much more closely than those in HP $Si_3N_4$ and appear to be diverted only by large pores. Figure 27 shows parts of several concentric ring cracks and an interconnecting crack in radial orientation, which are typical features of damage in RB $Si_3N_4$. The interconnecting cracks form when a propagating ring crack is diverted, presumably by a microstructural feature. The propagation direction of these radial segments, relative to the indent center, is not known, but in many cases where the radial segments end in uncracked material, they have propagated toward the center of indentation, as can be seen in Figure 28. Ring cracks also interact with, and occasionally terminate at, large pores as shown in Figure 29.

Samples of ring cracks produced in particle impacts on RB $Si_3N_4$ are shown in Figures 30 and 31. The general appearance of the ring cracks produced quasi-statically and dynamically is very similar (compare Figures 27 and 30). The effect of the microstructure also appears to be similar. Ring cracks produced in particle impacts are seen to be similarly diverted by large pores and often terminated in them (Figure 31). The grains and the majority of pores in RB $Si_3N_4$ are smaller than 1 μm, however, and do not appear to exert a marked influence on crack propagation and macrofracture.

61
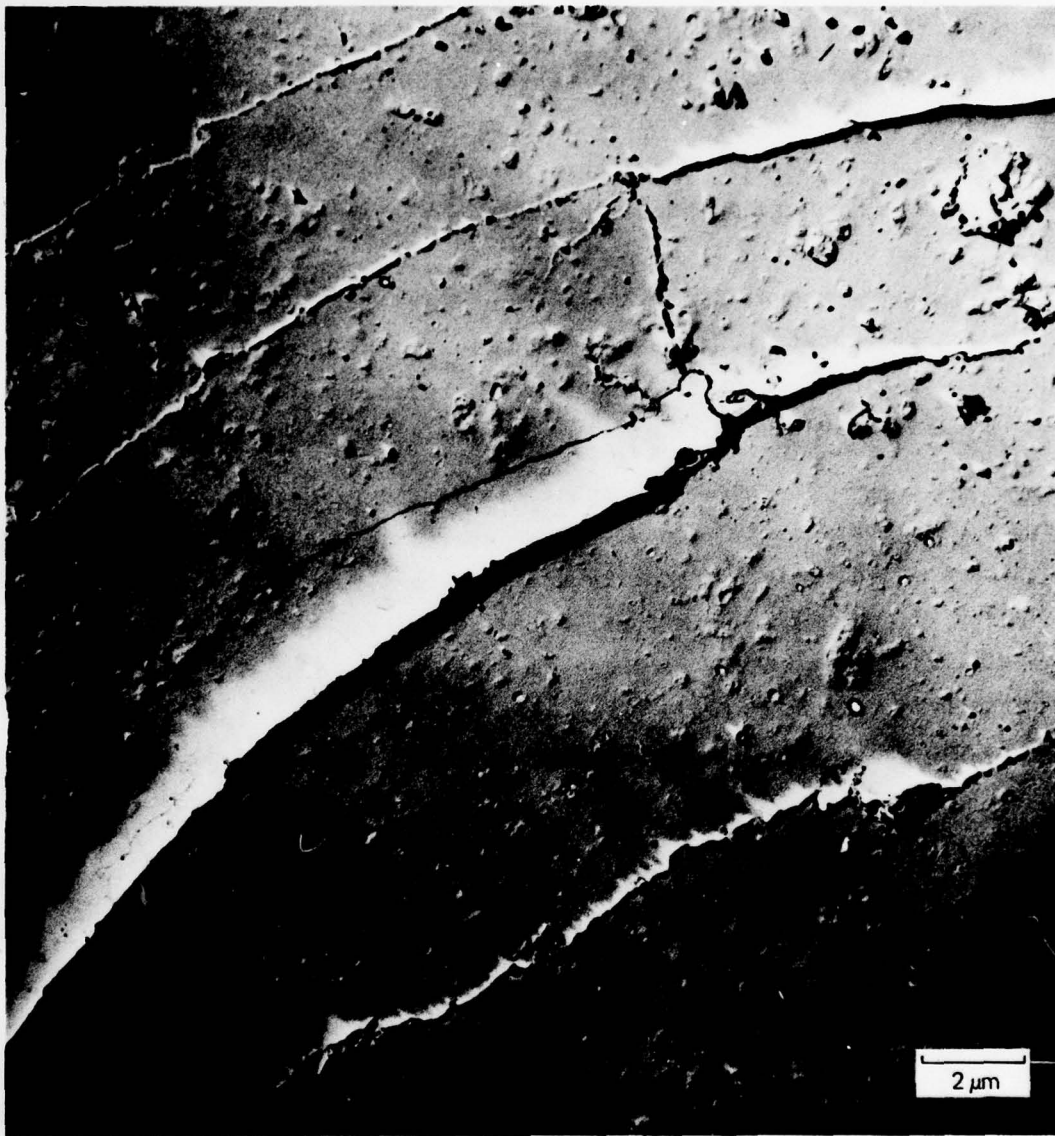
MP-4928-78

FIGURE 27    TYPICAL RING CRACKING BY QUASI-STATIC INDENTATION IN RB $Si_3N_4$: A
Population of Concentric Ring Cracks and Interconnecting Radial Segments

1μm

MP-4928-79

FIGURE 28   CRACK TIP OF A RADIAL SEGMENT (Shown in Figure 27) THAT VEERS TOWARD
CONTACT CENTER

MP-4928-80

FIGURE 29    A RING CRACK IN RB $Si_3N_4$  PRODUCED BY QUASI-STATIC INDENTATION THAT
TERMINATES AT A LARGE PORE
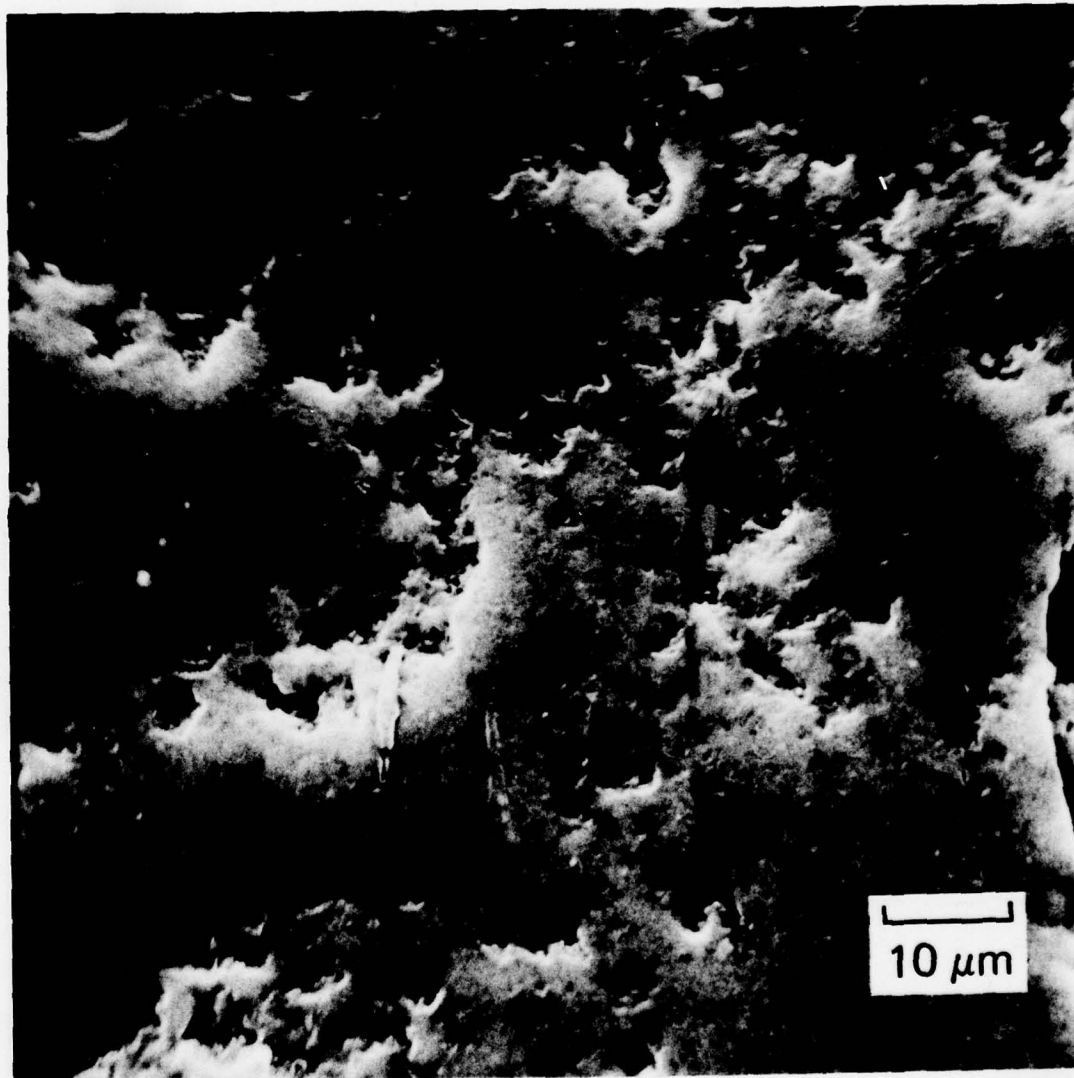
MP-4928-81

FIGURE 30    TYPICAL RING CRACKING BY PARTICLE IMPACT IN RB $Si_3N_4$

65
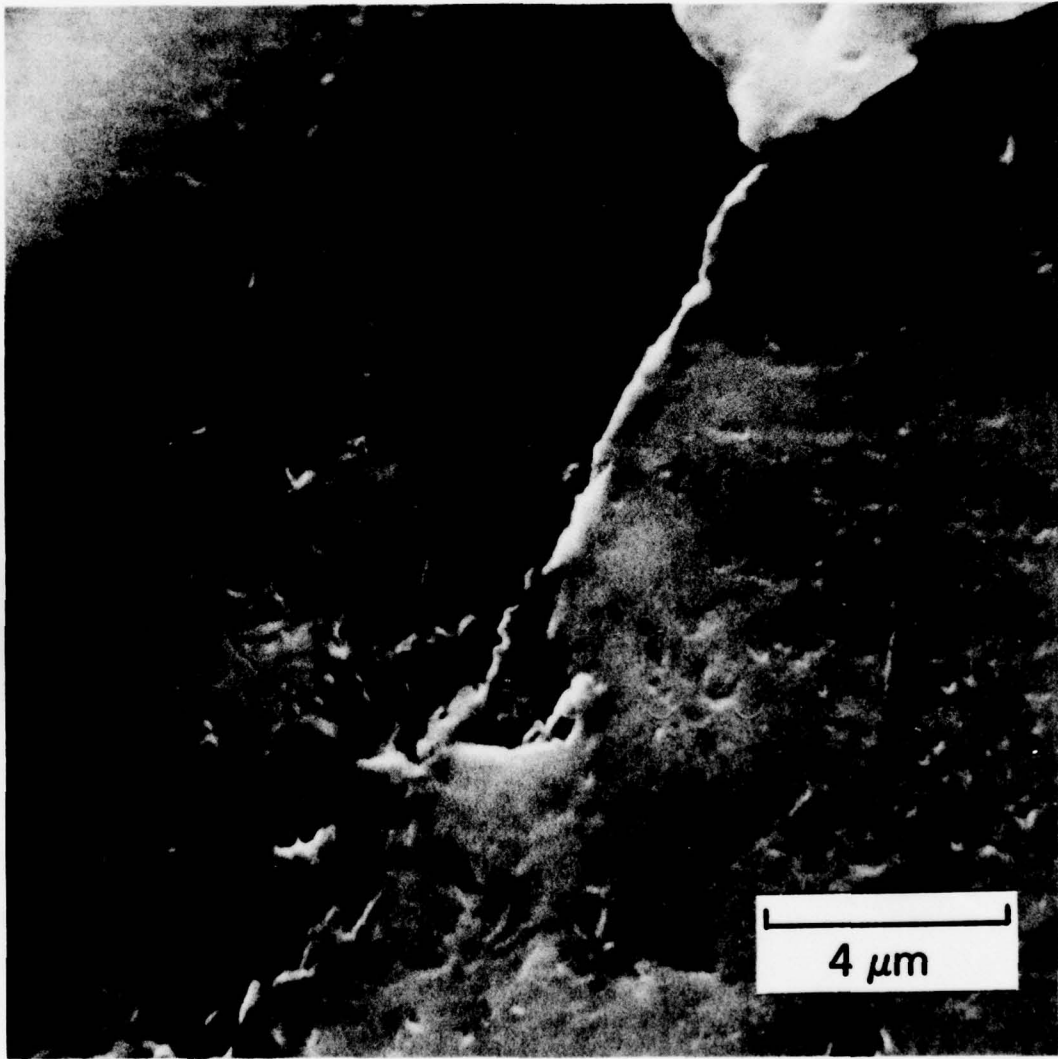
MP-4928-82

FIGURE 31    A RING CRACK IN RB Si$_3$N$_4$ PRODUCED BY PARTICLE IMPACT  THAT TERMINATES
AT A LARGE PORE

# VII  ANALYSIS OF RESULTS

## Nature of Contact

The coefficient of restitution, COR = $V_{reb}/V_{imp}$, or the fractional energy loss, $\frac{\Delta E}{E} = 1 - (COR)^2$, is a measure of the nature of contact. Experimental COR and fractional energy loss are plotted against impact velocity for all impact configurations in Figures 32 and 33. For all impact cases, the deviation from elastic impact (COR = 1) increased with impact velocity, as expected.

The behavior of RB $Si_3N_4$ and HP $Si_3N_4$ in similar impact conditions is compared in Figures 32(a) and 33(a). Higher energy loss and lower COR are indicated for tougher and higher-density HP $Si_3N_4$. Surface damage is heavy in both target materials (Figures 8 and 13), but WC spheres impacting HP $Si_3N_4$ suffered more severe plastic deformation and fracture (damage to particles is listed in Tables 1 and 2). Thus, most of the increased energy loss in the HP $Si_3N_4$ case was apparently absorbed, not in the target, but in damaging the impacting spheres. Oxidized and unoxidized HP $Si_3N_4$ under similar impact conditions are compared in Figures 32(b) and 33(b). The data indicate similar contact behavior. Impacts of HP $Si_3N_4$ by particles of different materials (WC and steel) are also compared in Figures 32(b) and 33(b). The results show that, except for low velocities, both impact situations were highly nonelastic.

Examination of impact damage to particles in these impacts also provided information directly related to the nature of contact. In almost all cases, elastic impacts (COR $\gtrsim$ 1) produced intact particles, and in impacts with low COR (i.e., reduced rebound velocities) the particles were heavily deformed or fragmented. Observed particle damage for different tests is listed with other impact parameters in Tables 1 through 3.

67
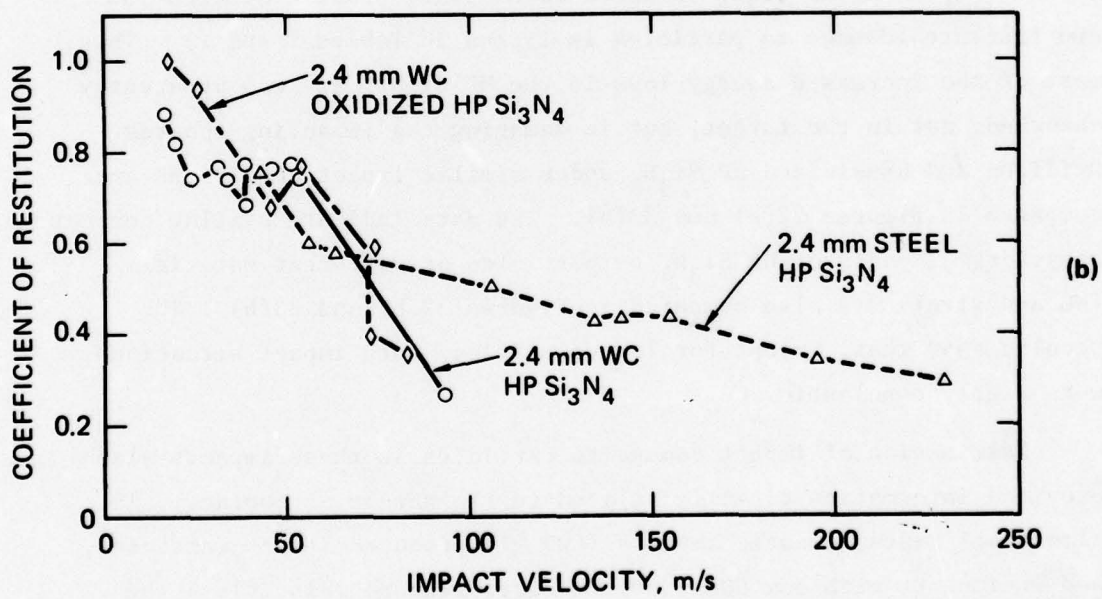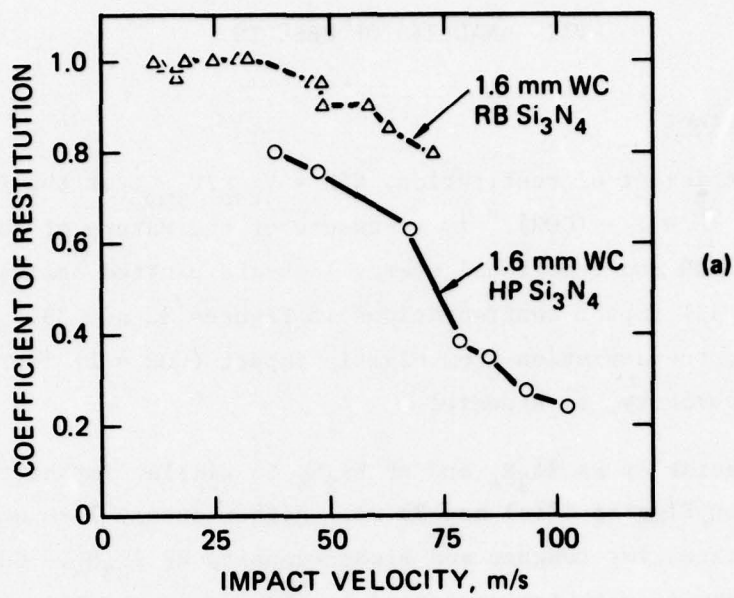
FIGURE 32   COEFFICIENT OF RESTITUTION

MA–4928–58

68

(a)

1.6 mm WC
HP Si₃N₄

1.6 mm WC
RB Si₃N₄

(b)

2.4 mm WC
HP Si₃N₄

2.4 mm STEEL
HP Si₃N₄

2.4 mm WC
OXIDIZED HP Si₃N₄
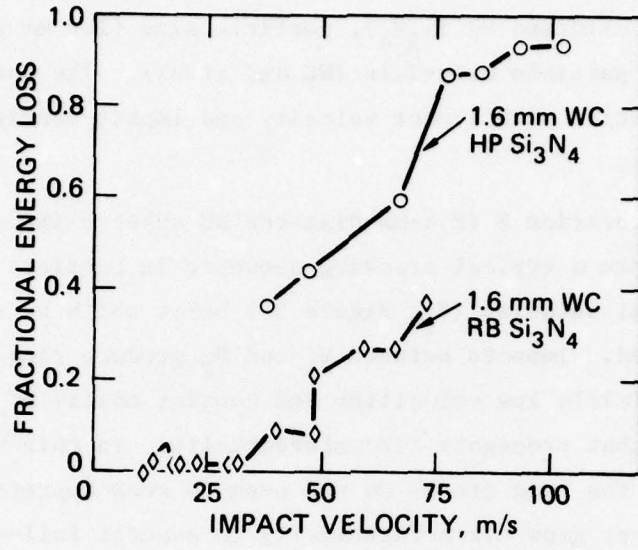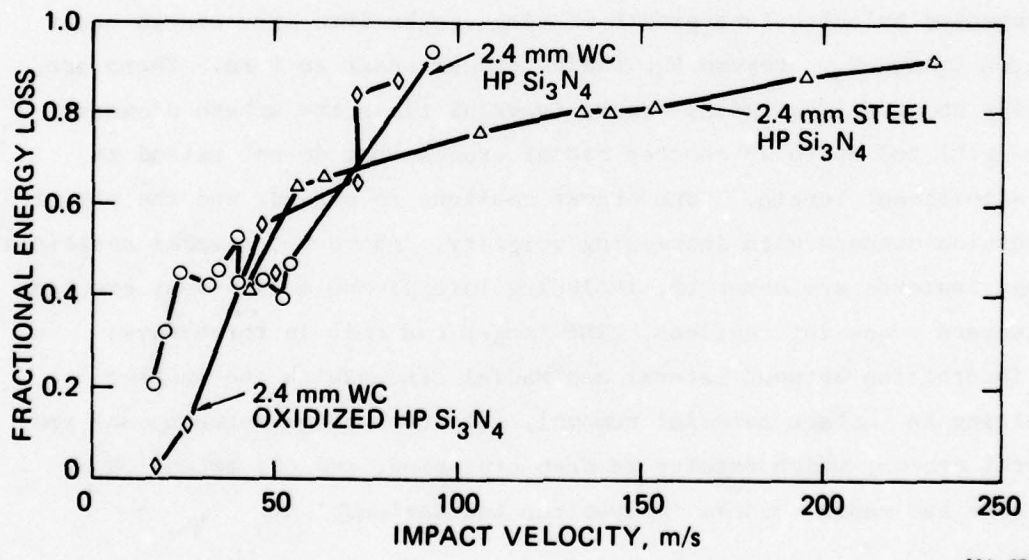
MA-4928-59

FIGURE 33   FRACTIONAL ENERGY LOSS

69

## Failure Modes

The fractographic examinations of individual impact configurations described in Sections III and V are now combined for an overall study of the specimen failure modes as influenced by various target materials (HP and RB $Si_3N_4$, oxidized HP $Si_3N_4$), particle size (1.6 mm and 2.4 mm in diameter), and particle materials (WC and steel). The variation of damage characteristics with impact velocity and impact configuration is given in Figure 34.

Impact configuration B (2.4-mm-diameter WC spheres impacting HP $Si_3N_4$) represents a typical cracking sequence in particle impacts. There is a critical velocity ($V_1$, Figure 34) below which no target damage was observed. Impacts between $V_1$ and $V_2$ produce ring cracks that nucleate at fairly low velocities and consist mostly of short segmental cracks that propagate circumferentially. In this velocity range ($V_1$ to $V_2$), the ring cracks do not seem to grow appreciably in depth; instead, they grow circumferentially to several full-circle cracks as the velocity increases. Surface plastic flow (plastic impressions) accompanied by subsurface growth of ring cracks into cone cracks occur between $V_2$ and $V_3$. Beyond $V_3$, radial cracks start to form. There are usually about 9 long radial cracks (several times the sphere diameter in length) and up to 25 shorter radial cracks that do not extend to any significant length. Cone cracks continue to extend, and the plastic impression deepens with increasing velocity. Above $V_4$, several additional damage features are observed, including lateral and median-vent cracking and severe crack interactions. The target can fail in three ways: (1) interaction between lateral and radial cracks with the surface resulting in surface material removal, (2) interaction between cone and lateral cracks, which results in deep cratering, and (3) extension of the cone and radial cracks to specimen boundaries.

Response of RB and HP $Si_3N_4$ to similar impacts can be compared in Figure 34 (configurations D and C). The cracking sequence is similar for both materials, but all stages of fracture development in RB $Si_3N_4$ occur in a much narrower range and at substantially lower impact velocity.
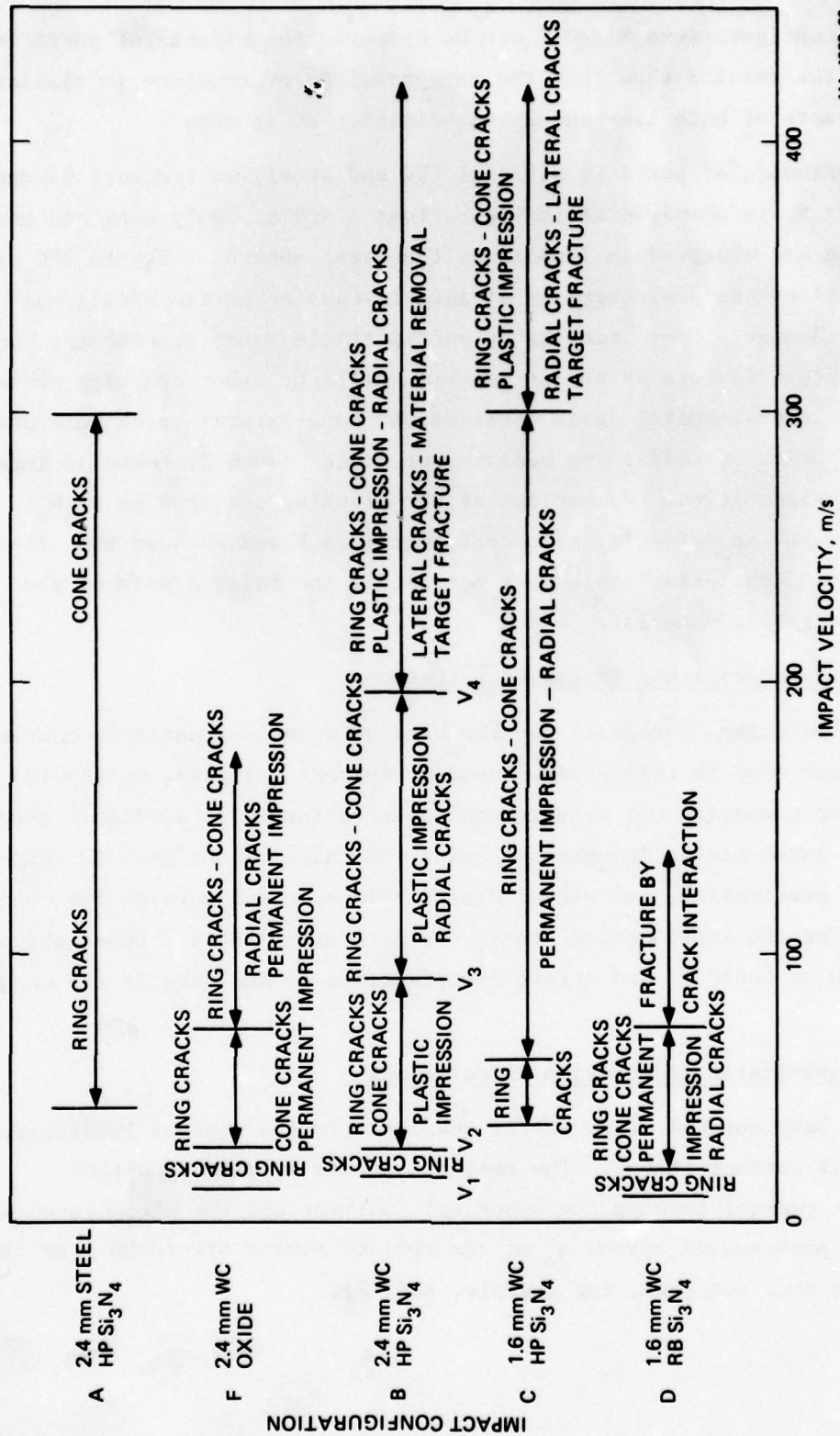
70

FIGURE 34  SPECIMEN FAILURE MODES

MA-4928-60

71

Impact configurations B and C can be compared for effects of particle size. The results show that the phenomonology of fracture is similar for impacts of both 1.6- and 2.4-mm-diameter WC spheres.

Influence of particle material (WC and steel) on fracture damage in HP $Si_3N_4$ is compared in configurations A and B. Only ring and cone cracking are observed in impacts by the steel spheres. Beyond 300 m/s, the steel sphere disintegrates at impact, causing little additional surface damage. Cone cracking by soft-particle impacts, however, could cause target failure as severe as that caused by other cracking mechanisms such as lateral-radial crack interaction, cone-lateral crack interaction, and extension of radial and median-vent cracks commonly found in impacts by harder particles. Comparison of the cracking patterns on $Si_3N_4$ covered with an oxide layer in configurations B and F shows that the presence of the oxide scale does not change the failure mode of the underlying host material.

## Contact Parameters and Stress Distributions

Calculations were made for the various spherical particle contact situations used in this study, based on current analyses, to provide a means for comparing our experimental observations with available theory. For the quasi-static indentation case, the calculations provide contact radius, penetration, and stress distributions in and outside the contact zone. For the impact cases, they provide contact radius, penetration, duration of contact, and stress distributions in and outside the contact zone.

### Quasi-Static Indentation Calculations

We base our calculations for quasi-static indentation loading on the Hertz contact theory. The radius a of the circle of contact (contact radius) between the spherical indenter and the plane (specimen) and the peak normal stress $q_o$ at the contact center are found from the Hertzian analysis (see, for example, Ref. 7):

$$a = \left[ \frac{3FR}{4} \left( \frac{1 - \nu_1^2}{E_1} + \frac{1 - \nu_2^2}{E_2} \right) \right]^{1/3} \tag{1}$$

$$q_o = \frac{3F}{2\pi a^2} \quad \frac{3F^{1/3}}{2\pi \left[ \frac{3R}{4} \left( \frac{1 - \nu_1^2}{E_1} + \frac{1 - \nu_2^2}{E_2} \right) \right]^{2/3}} \tag{2}$$

where F is the normal load on the indenter, R is the indenter radius, $E_1$ and $E_2$ are the Young's moduli of the plane and indenter, respectively, and $\nu_1$ and $\nu_2$ are the corresponding values of the Poisson's ratio.

A force-penetration relation can also be obtained from the Hertz contact theory:

$$F = \frac{4X^{3/2} R^{1/2}}{3 \left( \frac{1 - \nu_1^2}{E_1} + \frac{1 - \nu_2^2}{E_2} \right)} \tag{3}$$

where X is the penetration or distance of mutual approach.

The noraml stress between a spherical indenter and a plane is shown by the Hertz contact theory to vary from $q_o$ at the center to zero at the outer edge of the contact area.

$$q = \frac{q_o}{a} \sqrt{a^2 - r^2} \tag{4}$$

where r is the radial distance from the center of the contact area. Because of this normal stress, large radial and circumferential (hoop) stresses occur at the surface of the plate. The amplitude of the radial and circumferential stresses at the surface of an elastic plate will now be determined for statically applied spherical indenter.

The solution procedure follows the analysis of Bycroft[8] for loadings on an elastic half-space. First the radial and vertical displacements are written as integrals of Bessel functions.

73

$$u = \int_0^\infty (A_1 + B_1 z)e^{-xz}J_1(xr)dx \qquad (5)$$

$$w = \int_0^\infty [A_1 - \frac{B_1(\tau^2 + 1)}{x(\tau^2 - 1)} + B_1z]e^{-xz}J_o(xr)dx \qquad (6)$$

where $A_1$ and $B_1$ = functions of x, the variable of integration

r  =  radial coordinate

z  =  depth coordinate

$\tau^2$  =  $\mu/(\lambda + 2\mu)$

$\lambda, \mu$ = Lame's constants.

Next we use the elastic stress-strain relations (specialized for the axisymmetric case) to determine the radial, depth, hoop, and shear stresses

$$\sigma_{rr} = \lambda\left(\frac{\partial u}{\partial r} + \frac{u}{r} + \frac{\partial w}{\partial z}\right) + 2\mu\frac{\partial u}{\partial r} \qquad (7)$$

$$\sigma_{zz} = \lambda\left(\frac{\partial u}{\partial r} + \frac{u}{r} + \frac{\partial w}{\partial z}\right) + 2\mu\frac{\partial w}{\partial z} \qquad (8)$$

$$\sigma_{\theta\theta} = \lambda\left(\frac{\partial u}{\partial r} + \frac{u}{r} + \frac{\partial w}{\partial z}\right) + 2\mu\frac{u}{r} \qquad (9)$$

$$\sigma_{rz} = \mu\left(\frac{\partial u}{\partial z} + \frac{\partial w}{\partial r}\right) \qquad (10)$$

The shear stress expression at the surface (z = 0) is obtained by inserting the integrals from Eqs. (5) and (6) into Eq. (10):

$$\sigma_{rz} = \int_0^\infty 2\mu\left[\frac{B_1\tau^2}{\tau^2 - 1} - A_1x\right]J_1(xr)dx \qquad (11)$$

74

A zero shear stress condition on the surface is obtained by setting

$$\frac{B_1 \tau^2}{\tau^2 - 1} = A_1 x = A_2 \tau^2 x \tag{12}$$

where $A_2$ is a new function of x. Next we obtain the expression for stress in the depth direction at the surface.

$$\sigma_{zz} = \int_0^\infty 2\mu \left[ \frac{B_1}{\tau^2 - 1} - A_1 x \right] J_0(xr)dx \tag{13}$$

$$= 2\mu(\tau^2 - 1) \int_0^\infty A_2(x)x \, J_0(xr)dx$$

In this equation we have introduced the new variable $A_2$ from Eq. (12). Now we wish to evaluate $A_2$ such that $\sigma_{zz}$ will equal the applied stress in Eq. (4) in the region of contact and be zero elsewhere on the surface. $A_2$ is obtained by equating the loading to a Fourier-Bessel expansion as follows:

$$q = \frac{q_0}{a} \sqrt{a^2 - r^2} = \frac{q_0}{a} \int_0^\infty J_0(xr)x \left[ \int_0^\infty \sqrt{a^2 - t^2} \, J_0(xt)t\,dt \right] dx$$

$$\tag{14}$$

$$= \frac{q_0 \, 2\pi a}{2} \int_0^\infty J_{\frac{3}{2}}(xa) J_0(xr) x^{-3/2} dx$$

where the integration has been performed with Sonine's first finite integral (p. 740 of Ref. 9 and p. 406 of Ref. 10). By equating Eqs. (13) and (14), we now evaluate $A_2$

$$A_x(x) = \frac{q_0 \quad 2\pi a \; J_{3/2}(xa)}{4\mu(\tau^2 - 1) \; x^{3/2}} \tag{15}$$

75

Next the expression for $\sigma_{rr}$, Eq. (7), is derived from the equations for u and w, Eqs. (5) and (6) and then evaluated at the surface where $z = 0$. The result is

$$
\sigma_{rr} = 2(\lambda + \mu) \int_0^\infty A_1(x) x \, J_o(xr)dx - \frac{2\mu}{r} \int_0^\infty A_1(x) J_1(xr)dx
$$

(16)

$$
= \frac{q_o^2 \sqrt{2\pi a}}{2\mu(\tau^2 - 1)} \left[ (\lambda + \mu) \int_0^\infty J_{3/2}(xa) J_o(xr) x^{-1/2} dx \right.
$$

$$
\left. - \frac{\mu}{r} \int_0^\infty J_{3/2}(xa) J_1(xr) x^{-3/2} dx \right]
$$

These integrals are found in standard tables such as Gradshteyn and Ryzhik[9]. For $r < a$, that is, within the contact region, the radial stress is

$$
\sigma_{rr} = \frac{q_o \sqrt{\pi}}{2\Gamma(3/2)} \left[ F\left(1, -\frac{1}{2}, 1, \frac{r^2}{a^2}\right) - \frac{\mu}{\lambda + \mu} \frac{\Gamma(1)}{2\Gamma(2)} F\left(1, -\frac{1}{2}, 2, \frac{r^2}{a^2}\right) \right] \quad (17)
$$

where F is the hypergeometric function and $\Gamma$ is the gamma function. At the boundary of the contact area, $r = a$, and the radial stress is

$$
\sigma_{rr} = \frac{q_o \sqrt{\pi}}{2} \left[ \frac{\Gamma(\frac{1}{2}) \, \Gamma(1)}{\Gamma(0) \Gamma(\frac{3}{2}) \Gamma(\frac{3}{2})} - \frac{\mu}{\lambda + \mu} \cdot \frac{1}{2\Gamma(\frac{5}{2})} \right]
$$

(18)

Outside the contact area, where $r > a$, the radial stress is

$$
\sigma_{rr} = \frac{q_o \sqrt{\pi a^2}}{2r^2} \left[ \frac{\Gamma(1) F(1, 1, \frac{5}{2}, \frac{a^2}{r^2})}{\Gamma(0) \Gamma(\frac{5}{2})} \right.
$$

(19)

$$
\left. - \frac{\mu}{(\lambda + \mu) 2 \, \Gamma(\frac{5}{2})} F(1, 0, \frac{5}{2}, \frac{a^2}{r^2}) \right]
$$

76

The three expressions for radial stress can be reduced somewhat by evaluating the Gamma functions (Ref. 10, p. 3) and writing the hypergeometric functions as integrals (Ref. 11, p. 59). The following intermediate results are obtained.

$$F(1, -\frac{1}{2}, 1, \frac{r^2}{a^2}) = \sqrt{1 - r^2/a^2}$$

$$F(1, -\frac{1}{2}, 2, \frac{r^2}{a^2}) = -\frac{2a^2}{3r^2}\left[\left(1 - \frac{r^2}{a^2}\right)^{3/2} - 1\right]$$

$$F(1, 1, \frac{5}{2}, \frac{a^2}{r^2}) = \frac{3r^2}{a^2}\left[1 - \sqrt{\frac{r^2 - a^2}{a^2}} \text{ acrtan } \sqrt{\frac{a^2}{r^2 - a^2}}\right]$$

$$F(1, 0, \frac{5}{2}, \frac{a^2}{r^2}) = 1$$

$$\Gamma(0) = \infty$$

$$\Gamma(\frac{1}{2}) = \sqrt{\pi}$$

$$\Gamma(1) = 1$$

$$\Gamma(\frac{3}{2}) = \sqrt{\pi/2}$$

$$\Gamma(2) = 1$$

$$\Delta(\frac{5}{2}) = 3\sqrt{\pi/4}$$

77

In Eqs. (17) through (19), the ratio $\mu/(\lambda + \mu)$ is replaced by $1 - 2\nu$, where $\nu$ is Poisson's ratio. Then these equations become

For $r < a$:

$$\sigma_{rr} = q_o\{\sqrt{1 - r^2/a^2} + (1 - 2\nu)\frac{a^2}{3r^2}[(1 - r^2/a^2)^{3/2} - 1]\} \tag{20}$$

For $r = a$:

$$\sigma_{rr} = -\frac{(1 - 2\nu)}{3}q_o \tag{21}$$

For $r > a$:

$$\sigma_{rr} = -\frac{(1 - 2\nu)}{3}q_o \cdot \frac{a^2}{e^2} \tag{22}$$

For $r = 0$, Eq. (20) becomes

$$\sigma_{rr} = \frac{(1 + 2\nu)}{2}q_o \tag{23}$$

With the radial stress known, the circumferential stress $\sigma_{\theta\theta}$ can be easily found. Starting with Eq. (9), the expressions for u and w, and the value of $A_2$ from Eq. (15), we obtain an expression for $\sigma_{\theta\theta}$ comparable to Eq. (16)

$$\sigma_{\theta\theta} = 2\lambda \int_0^\infty A_1 \, x \, J_o(xr)dx + \frac{2\mu}{r} \int_0^\infty A_1 J_1(xr)dx \tag{24}$$

These two terms are proportional to the corresponding terms for $\sigma_{rr}$. We need only multiply the first term in $\sigma_{rr}$ by $\lambda/(\lambda + \mu) = 2\nu$ and change the sign of the second term in $\sigma_{rr}$. Then the final results are obtained from Eqs. (20) through (22).

78

For r < a:

$$\sigma_{\theta\theta} = q_o \left\{ 2\nu\sqrt{1 - r^2/a^2} - (1 - 2\nu) \frac{a^2}{3r^2} \left[ (1 - r^2/a^2)^{3/2} - 1 \right] \right\} \quad (25)$$

For r = a:

$$\sigma_{\theta\theta} = \frac{1 - 2\nu}{3} q_o \quad\quad\quad (26)$$

For r > a:

$$\sigma_{\theta\theta} = \frac{(1 - 2\nu) q_o a^2}{3r^2} \quad\quad\quad (27)$$

The stress is in the center of the contact area is

$$\sigma_{\theta\theta} = \frac{(1 + 2\nu)}{2} q_o \quad\quad\quad (28)$$

as it was for the radial stress.

The values of $q_o$, a, $\theta_{rr}$, and X from the foregoing equations are plotted in Figure 35 for a range of loadings for the indentation configuration listed in Table 5. The table also lists the material properties used in the calculation. The radial hoop and depth stress, $\sigma_{rr}$, $\sigma_{\theta\theta}$, and $\sigma_{zz}$ are plotted in Figure 36 for Poisson ratio of 0.26, the value for silicon nitride.

The stresses at r = 0, Eqs. (23) and (28), agrees with the results of Timoshenko[7] and Goodier for the stresses in the center of a uniformly loaded region. Also Eqs. (22) and (27) are identical with the results of Boussinesq[7] for stresses at a distance from a point load of magnitude $2q_o \pi a^2/3$.
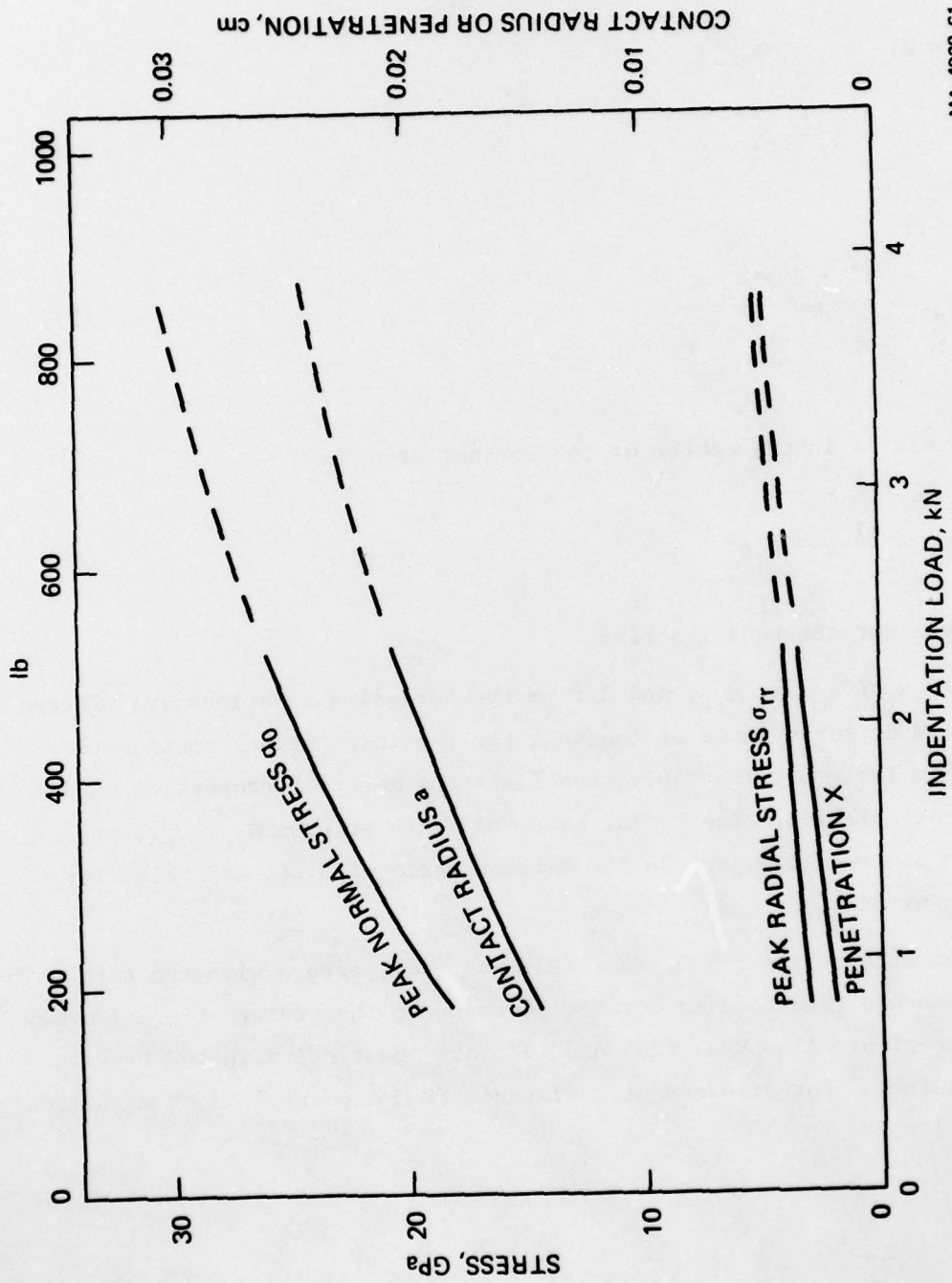
FIGURE 35  QUASI-STATIC CONTACT PARAMETERS (Indenter: 2.4-mm-Diameter WC Sphere Specimen: HP Si$_3$N$_4$)
Dotted lines are for range where experiments indicated inelastic behavior of the indenter.

MA-4928-61

80

## Table 5

### CONDITIONS FOR SPHERICAL CONTACT CALCULATIONS

| Calculation | Contact Configuration | | |
| --- | --- | --- | --- |
| | Loading | Sphere | Specimen |
| 1 | Indentation | 2.4-mm-dia WC | HP $Si_3N_4$ |
| 2 | Particle Impact | 2.4-mm-dia WC | HP $Si_3N_4$ |
| 3 | Particle Impact | 2.4-mm-dia steel | HP $Si_3N_4$ |
| 4 | Particle Impact | 1.6-mm-dia WC | HP $Si_3N_4$ |
| 5 | Particle Impact | 1.6-mm-dia WC | RB $Si_3N_4$ |

| Material | Material Properties | | |
| --- | --- | --- | --- |
| | Density, $\rho(g\ cm^{-3})$ | Modulus, E (GPa) | Poisson Ratio, $\nu$ |
| WC | 15.0 | 700 | 0.24 |
| Steel | 7.85 | 207 | 0.28 |
| HP $Si_3N_4$ | 3.3 | 320 | 0.26 |
| RB $Si_3N_4$ | 2.5 | 170 | 0.26 |

$q_0$ = MAXIMUM NORMAL STRESS UNDER THE SPHERE
a = RADIUS OF CONTACT

NORMAL $\sigma_{zz}$

HOOP $\sigma_{\theta\theta}$

RADIAL $\sigma_{rr}$

COMPRESSIVE

TENSILE

$\sigma/q_0$

r/a
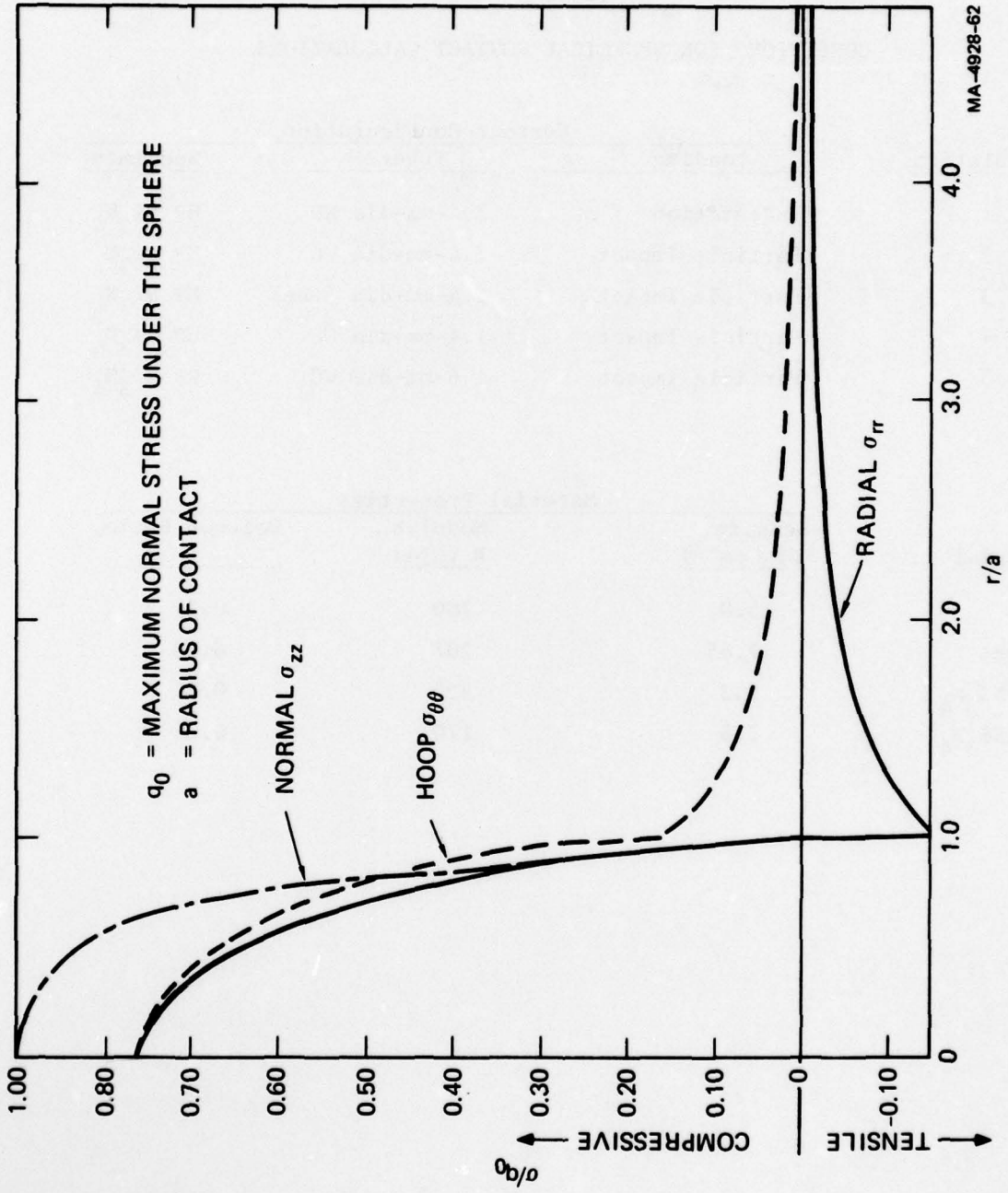
MA–4928–62

FIGURE 36   SURFACE STRESS DISTRIBUTIONS FOR QUASI-STATIC AND DYNAMIC ELASTIC CONTACTS

## Particle Impact Calculations

An approximate analysis of the spherical particle impact problem was made to provide a means for relating stresses and damage in the impact case to those in the static case. The spherical particle and the impacted plate (half-space) were taken to be elastic. The Hertz contact solution provided the force-displacement relations between the bodies. The present analysis provides the normal stresses in the contact area, extent of the contact area, duration of the impact, and displacement of the sphere after initial contact.

The static elastic stress distribution is used, in the analysis although the problem is dynamic and stresses are above the yield values. Hence the results can be expected to provide only an indication of the stress, duration, and contact area. The effects of the approximations are discussed at the end of this section.

The impact calculation was made by solving the following three equations with a finite difference technique:

$$u = \frac{dX}{dt} \qquad \text{(velocity-displacement)} \qquad (29)$$

$$F = M\frac{du}{dt} \qquad \text{(momentum)} \qquad (30)$$

$$F = F(X) \qquad \text{(force-displacement)} \qquad (31)$$

where F = normal force between the sphere and the plane

M = particle mass

u = particle velocity

X = particle displacement

t = time.

83

The equations are integrated by writing them in finite-difference form
and then integrating them over short time increments to obtain the force,
velocity, and displacement history. In finite-difference form, the
first two equations are

$$X_i = X_{i=1} + U_{i-\frac{1}{2}} \Delta t_{i-\frac{1}{2}} \tag{32}$$

$$\Delta U_i = \frac{F_i}{M} \Delta t_i \tag{33}$$

where the subscript i refers to the time increment. Hence $X_i$ and $F_i$
pertain to the $i^{th}$ time $t_i$, and $U_{i-\frac{1}{2}}$ pertains to a time $t_{i-\frac{1}{2}}$. The
increments are

$$\Delta U_i = U_{i+\frac{1}{2}} - U_{i-\frac{1}{2}}$$

$$\Delta t_i = t_{i+\frac{1}{2}} - t_{i-\frac{1}{2}}$$

$$\Delta t_{i-\frac{1}{2}} = t_i - t_{i-1}$$

With the noted subscripts in Eq. (32) and (33), the differences are
all central differences. Hence all derivatives and other terms pertain
to the same time.

The force-displacement relation is obtained from the Hertz contact
theory:

$$F = \frac{4X^{3/2} \sqrt{R}}{3 \left( \frac{1 - \nu_1^2}{E_1} + \frac{1 - \nu_2^2}{E_2} \right)} \tag{3}$$

where R is the radius of the sphere

84

$\nu_1$, $\nu_2$ are Poisson's ratio of plane and sphere

$E_1$, $E_2$ are Young's modulus of plane and sphere.

Formulas for radius a of the contact area and the peak stress $q_o$ are also obtained from the Hertz theory:

$$a = \left[ \frac{3FR}{4} \left( \frac{1 - \nu_1^2}{E_1} + \frac{1 - \nu_2^2}{E_2} \right) \right]^{1/3} \tag{1}$$

$$q_o = \frac{3F}{2\pi a^2} = \frac{3F^{1/3}}{2\pi \left[ \frac{3R}{4} \left( \frac{1 - \nu_1^2}{E_1} + \frac{1 - \nu_2^2}{E_2} \right) \right]^{2/3}} \tag{2}$$

The peak stress $q_o$ is 1.5 times the average stress over the contact area. For the impact calculations, the time steps were taken to be small enough that the velocity change was less than 1% of the impact velocity.

Computations were made for a range of velocities for the four impact configurations listed in Table 5. The table also lists the material properties used in the calculations. The quantities of principal interest are those at the time $t_m$ of the maximum penetration of the sphere into the plane. Figures 37 through 40 plot the peak stress at the center of the contact area, the equivalent quasi-static load F, radius of the contact area, displacment of the sphere at the time $t_m$ and $t_m$ as functions of impact velocity. These curves exhibit the nonlinear nature of the impact problem.

The main results are that the impact durations are about one to two microseconds and the peak stresses are tens of GPa. The force-velocity relations provide an approximate means for relating the impact and static testing conditions.

85
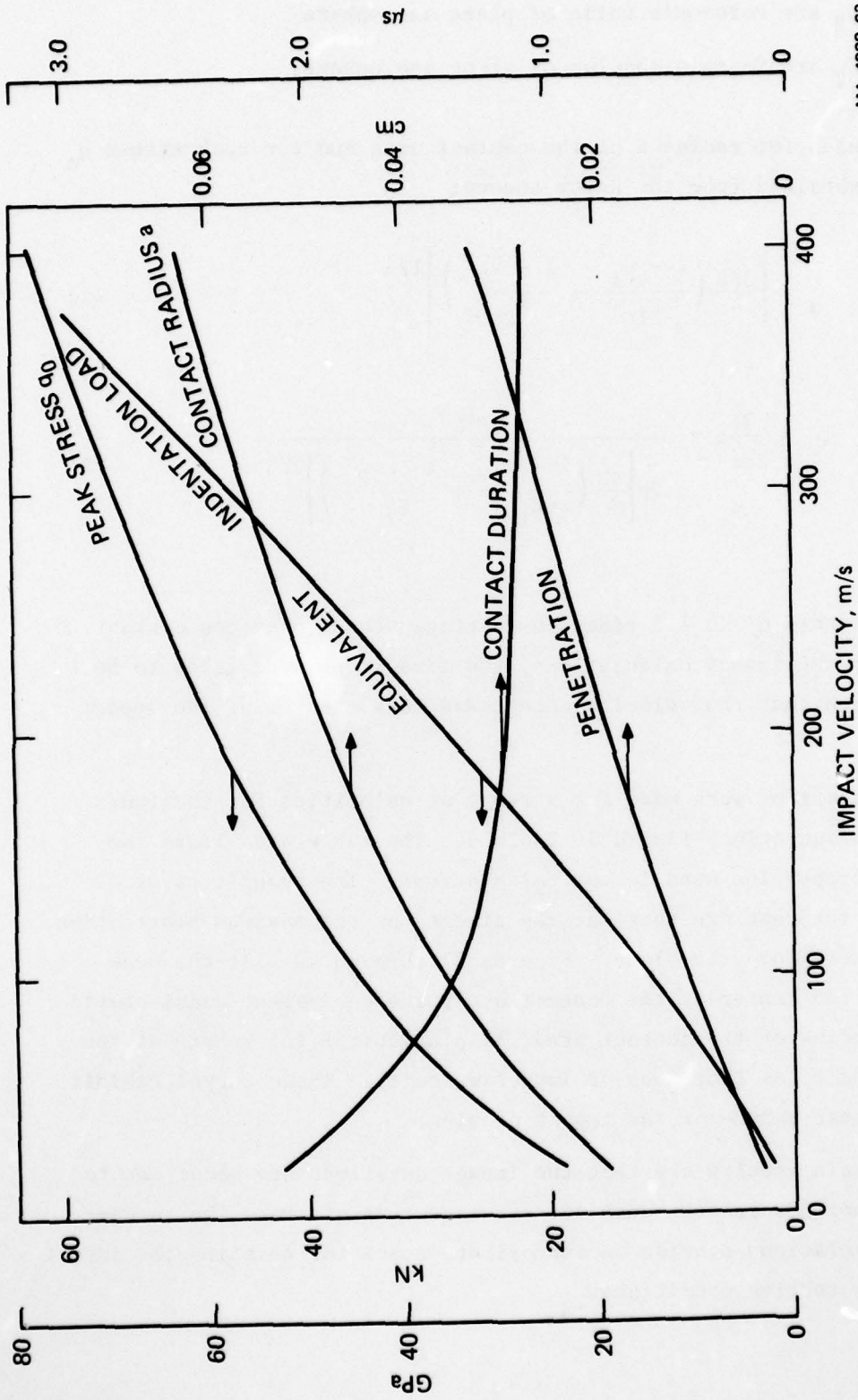
FIGURE 37    DYNAMIC CONTACT PARAMETERS (Particle: 2.4-mm-Diameter WC Sphere
Target: HP Si₃N₄)

MA-4928-63

86
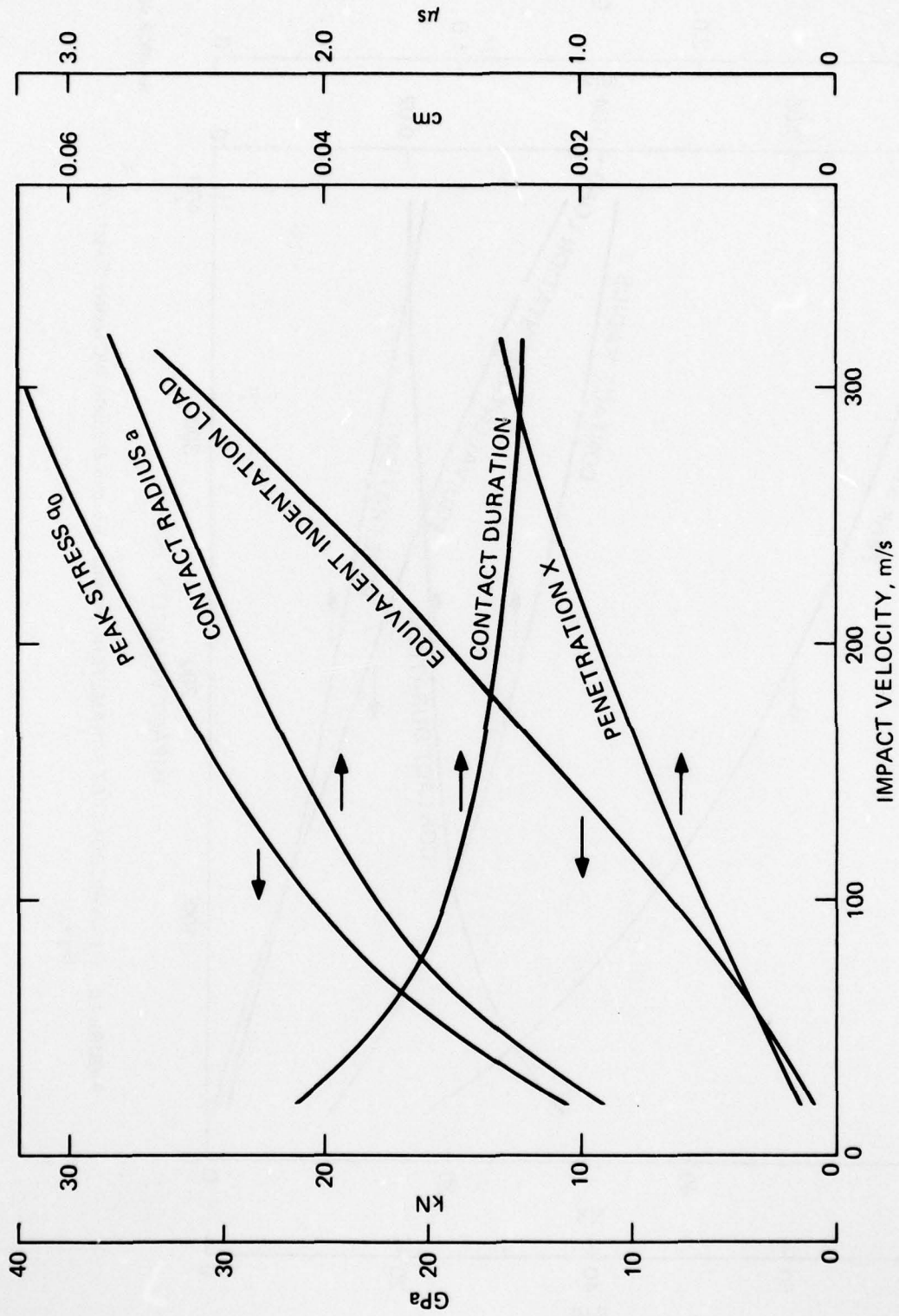
FIGURE 38   DYNAMIC CONTACT PARAMETERS (Particle: 2.4-mm-Diameter Steel Sphere Target: HP Si₃N₄)

MA-4928-64

87
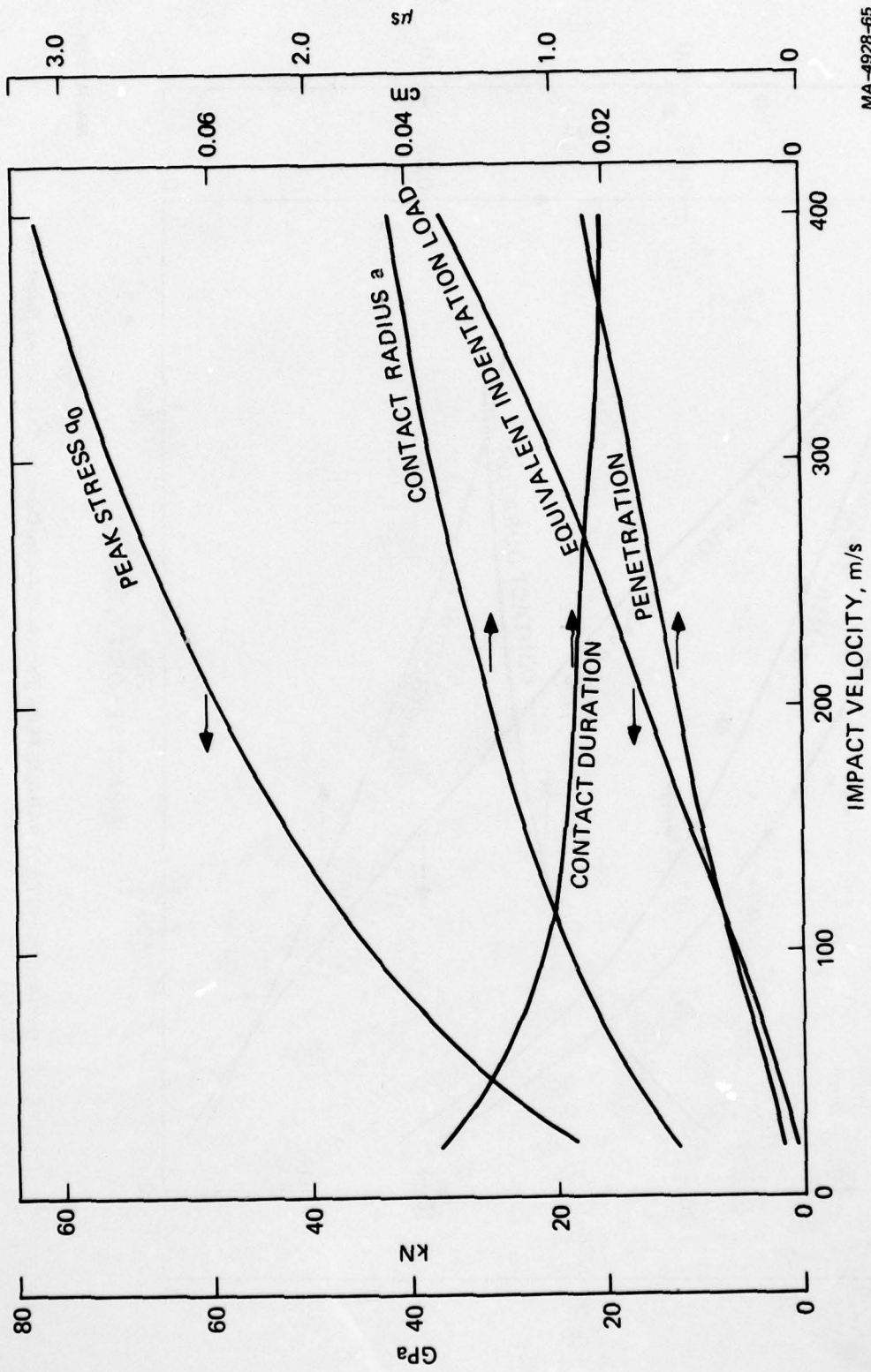
FIGURE 39  DYNAMIC CONTACT PARAMETERS (Particle: 1.6-mm-Diameter WC Sphere Target: HP $Si_3N_4$)

MA-4928-65

88
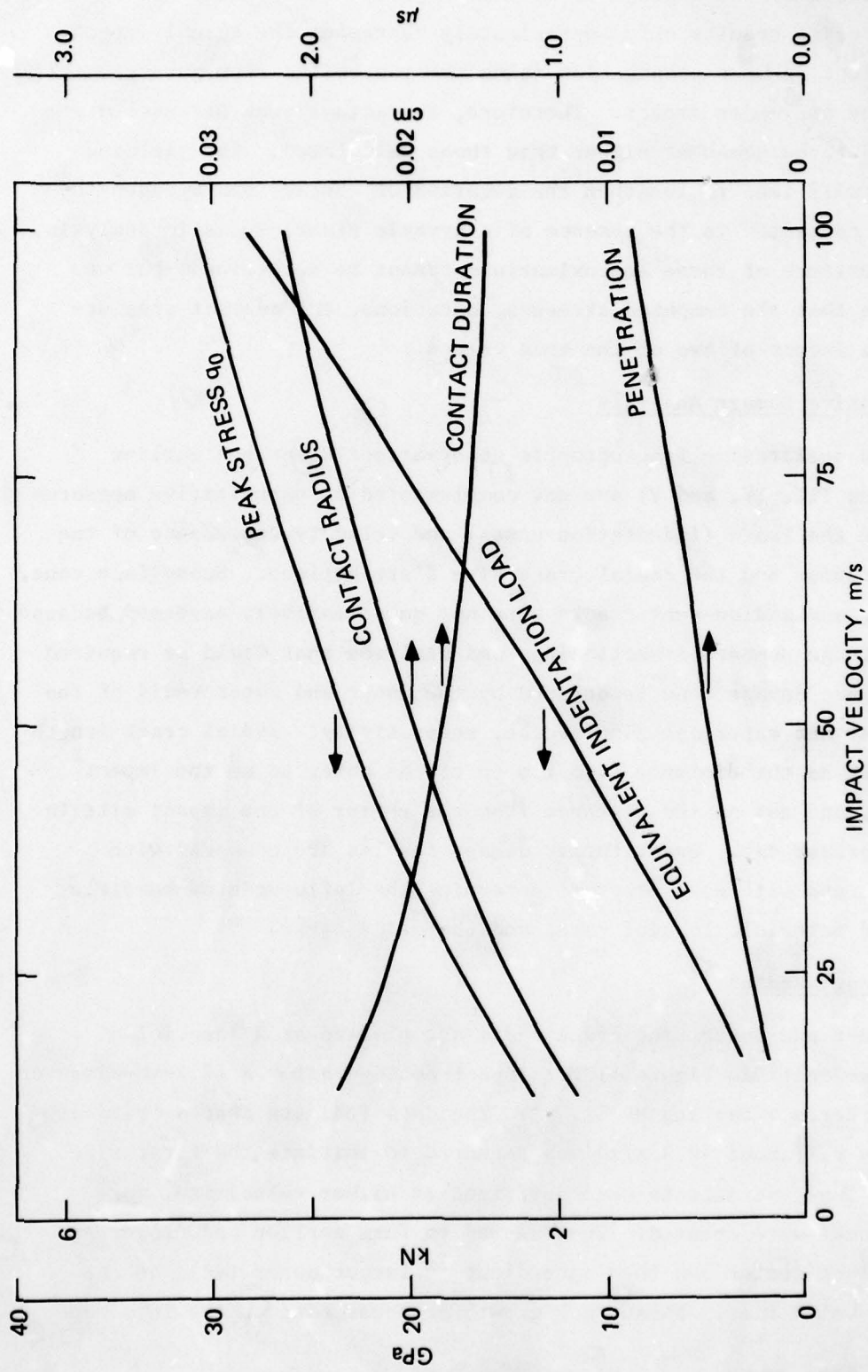
FIGURE 40 DYNAMIC CONTACT PARAMETERS (Particle: 1.6-mm-Diameter WC Sphere. Target: RB Si$_3$N$_4$)

MA-4928-66
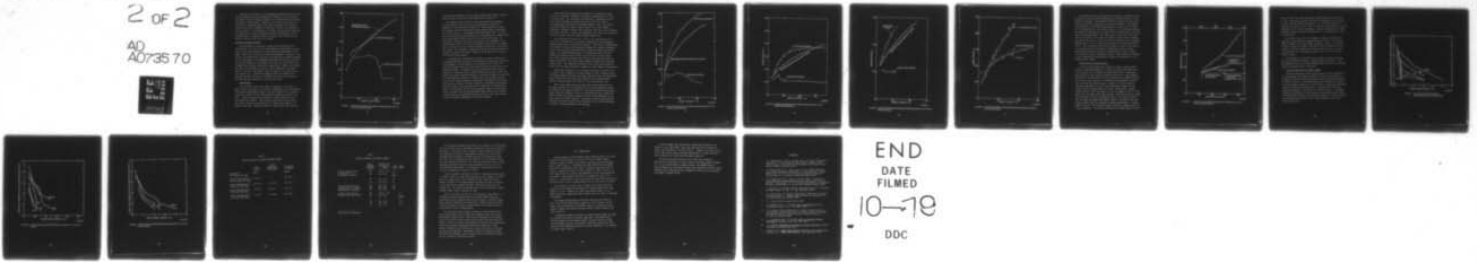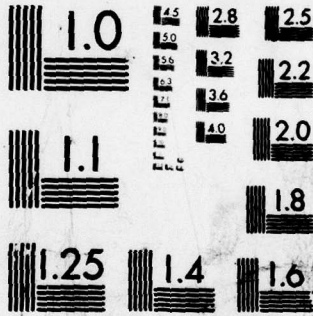
MICROCOPY RESOLUTION TEST CHART

NATIONAL BUREAU OF STANDARDS-1963-A

Because of the neglect of wave propagation times and yield effects, the preceding results only approximately represent the actual impact. The neglect of wave propagation makes the two bodies seem more flexible than they are under impact. Therefore, the actual peak stresses are expected to be somewhat higher than those calculated. The yielding process will tend to lengthen the duration of contact and broaden the area of contact. In the absence of a dynamic elastic-plastic analysis, the importance of these approximations cannot be determined, but we estimate that the computed stresses, durations, and contact area are within a factor of two of the true values.

## Quantitative Damage Analysis

The qualitative fractographic observations described earlier (Sections III, IV, and V) are now complemented by quantitative measurements of the load- (indentation cases) and velocity-dependence of the damage radius and the radial crack size distributions. Subsurface cone, lateral, and median-vent cracks were not quantitatively assessed because of the large number of sectionings and analyses that would be required. The surface damage zone is defined by the inner and outer radii of the innermost and outermost ring cracks, respectively. Radial crack length was taken as the distance from tip to tip as observed on the impact surface, and not as the distance from the center of the impact site to its outermost tip. Quantitative damage results are compared with analysis and with each other to determine the influences of particle size and material, loading rate, and the oxide layer.

### Damage Radius

Inner and outer ring crack radii are plotted as a function of impact velocity in Figure 41 for impact configuration A (2.4-mm-diameter steel spheres impacting HP $Si_3N_4$). The data indicate that a critical velocity $V_1$ (about 42.3 m/s) was required to initiate the first ring crack. Then, as impacts were performed at higher velocities, more ring cracks were created. They seemed to form earlier and closer to the contact center and then spread out to larger outer radii at the highest velocities. Subsurface growth of these ring cracks into cone

90
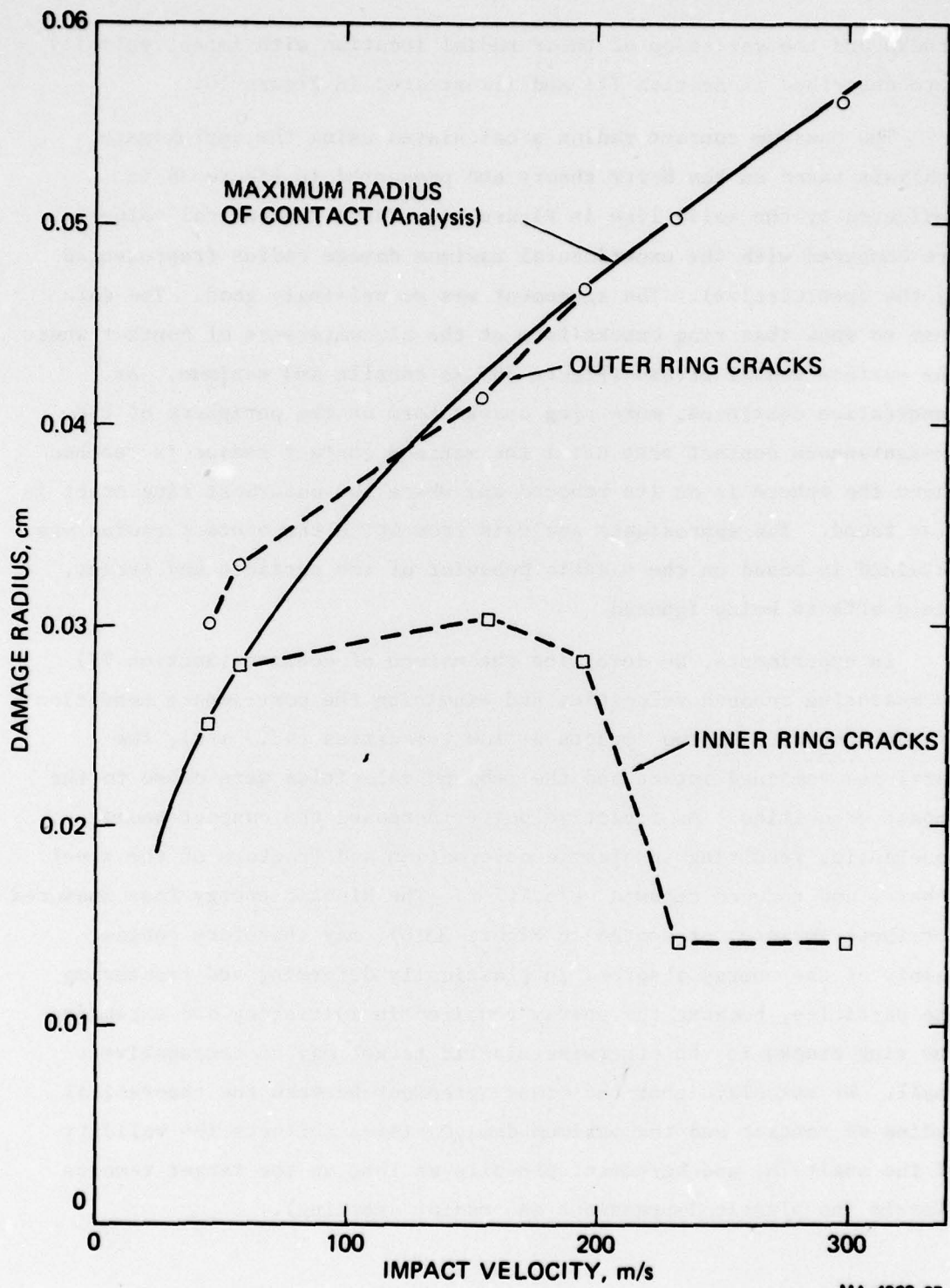
FIGURE 41   DAMAGE RADIUS RESULTS FOR IMPACT CONFIGURATION A (2.4-mm-
Diameter Steel Sphere/HP $Si_3N_4$)

91

cracks and the variation of their radial location with impact velocity were described in Section III and illustrated in Figure 10.

The maximum contact radius a calculated using the approximate analysis based on the Hertz theory and presented in Figure 38 is indicated by the solid line in Figure 41. These theoretical values are compared with the experimental maximum damage radius (represented by the open circles). The agreement was surprisingly good. The data seem to show that ring cracks form at the circumference of contact where the surface radial stress (Figure 36) is tensile and maximum. As penetration continues, more ring cracks form on the periphery of the instantaneous contact zone until the maximum contact radius is reached where the sphere is on its rebound and where the outermost ring crack is also found. The approximate analysis from which the contact radius was obtained is based on the elastic behavior of the particle and target, yield effects being ignored.

In experiments, we determine the nature of contact (Section VI) by measuring rebound velocities and examining the post-impact condition of the spheres. In two impacts at low velocities (42.3 m/s), the particles remained intact and the rebound velocities were close to the impact velocities. As impact velocity increased the contact became nonelastic, resulting in plastic deformation and fracture of the steel spheres and reduced rebound velocities. The kinetic energy loss measured for these impacts, presented in Figure 33(b), may therefore consist mainly of the energy absorbed in plastically deforming and fracturing the particles, because the energy required in initiating and extending the ring cracks in the otherwise elastic target may be comparatively small. We speculate that the close agreement between the theoretical radius of contact and the maximum damage radius reflects the validity of the analysis, and agreement prevails as long as the target remains elastic (no plastic impressions and radial cracking).

92

Inner and outer crack radii are plotted as a function of impact velocity in Figures 42 through 44 for impact configurations B, C, and D, respectively. For each impact configuration, a minimum (critical) velocity was required to nucleate the first ring crack, then at increasing impact velocity an increasing number of ring cracks formed and spread toward the contact center as well as to outer regions. Subsurface extension of these ring cracks into cone cracks also increased with impact velocity. Usually, the innermost cone crack grew catastrophically to several times the sphere diameter (Figure 12).

The theoretical maximum contact radii a are represented by the solid lines in Figures 42 to 44 and are compared with the experimental maximum damage radii (represented by points). These impact configurations used spheres of WC that had comparable hardness but superior deformation and fracture properties compared with the target materials (HP and RB $Si_3N_4$). The measured damage radius is consistently larger than the theoretical maximum contact radius, except for very low velocities. The results therefore indicate that, because both target and particle behave plastically, the actual contact radius is larger than predicted theoretically. The significant deviation from elastic theory seems to derive from the highly nonelastic condition of these impact configurations.

Comparison of Figures 42 and 43 shows the effect of particle size (1.6 and 2.4 mm in diameter) on impact damage in terms of damage radius. For similar impact velocities, the inner ring crack radii are essentially equal, whereas the outer ring crack radius for the 2.4-mm diameter spheres is approximately twice that for the 1.6-mm-diameter case.

Oxide crater radius and outer ring crack radius produced in the HP $Si_3N_4$ substrate are plotted together with the corresponding results for oxide-free HP $Si_3N_4$ in Figure 45. The results indicate that similar damage radius was produced in both the underlying HP $Si_3N_4$ (substrate) and the oxide-free material, whereas the size of the spallation in the oxide layer was slightly greater. The results therefore quantitatively show that the oxide has very little influence on the overall morphology or extent of fracture damage in the HP $Si_3N_4$.

93
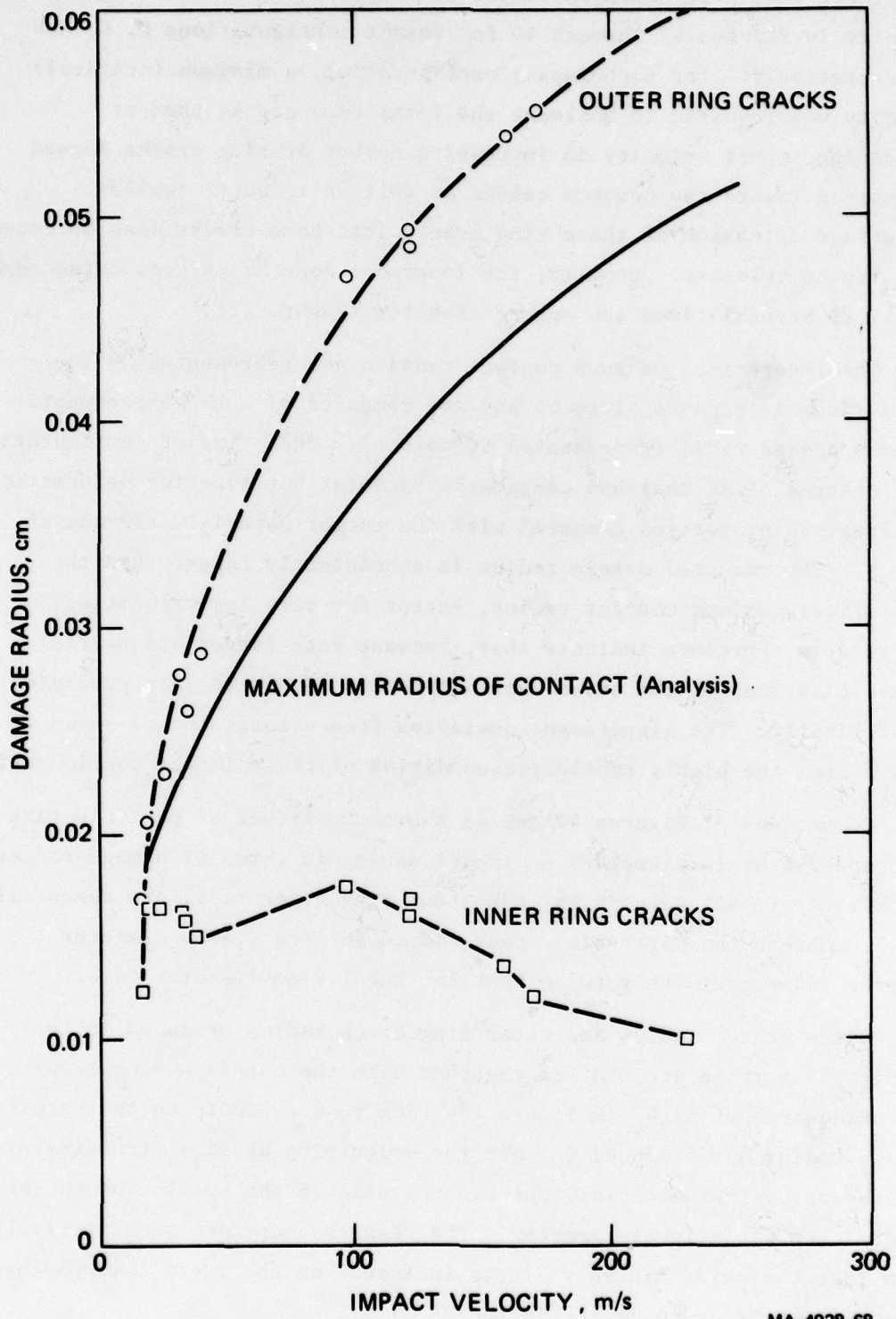
FIGURE 42    DAMAGE RADIUS RESULTS FOR IMPACT CONFIGURATION B (2.4-mm-
Diameter WC Sphere/HP Si$_3$N$_4$)

94
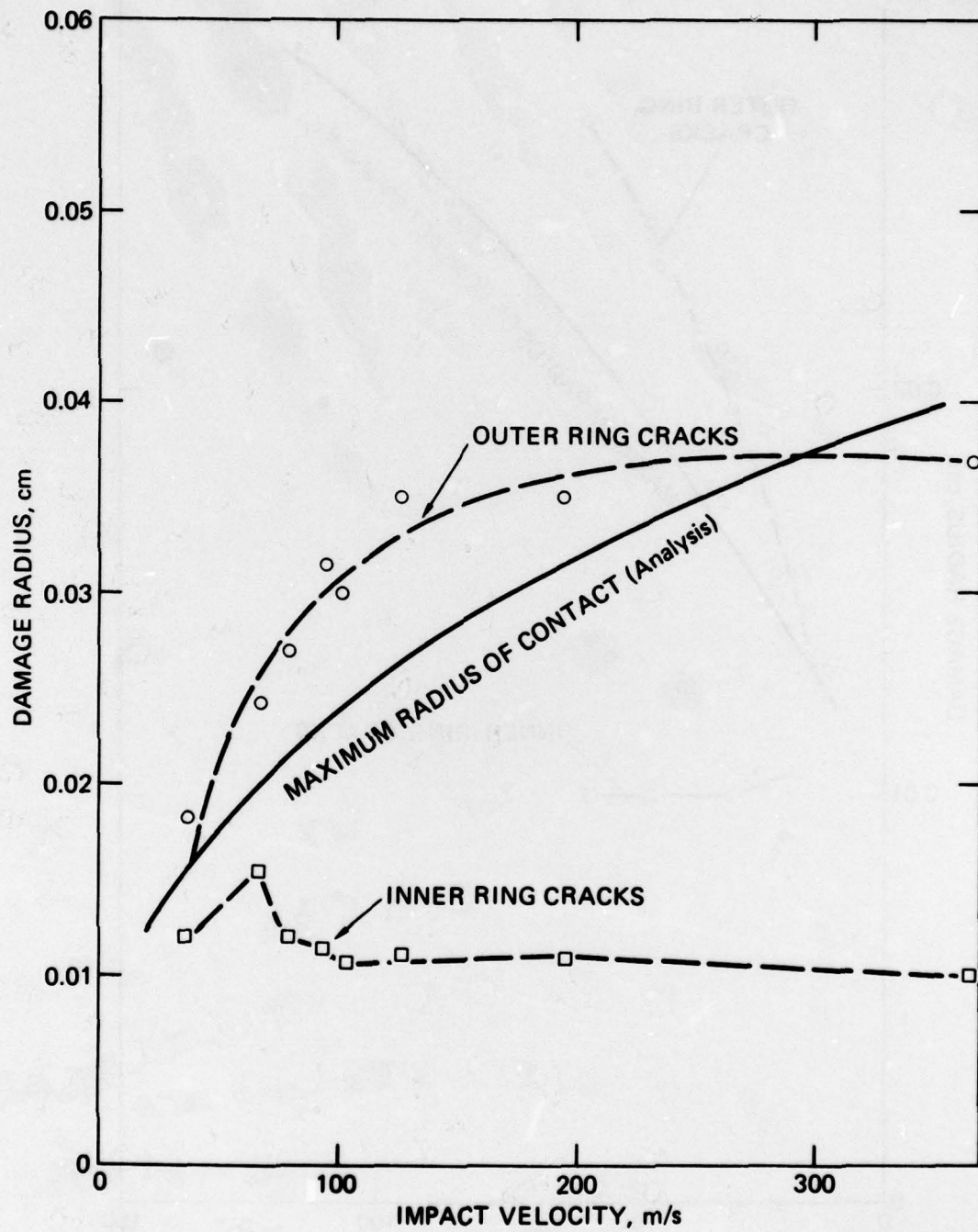
FIGURE 43    DAMAGE RADIUS RESULTS FOR IMPACT CONFIGURATION C (1.6-mm-
Diameter WC Sphere/HP Si$_3$N$_4$)

95
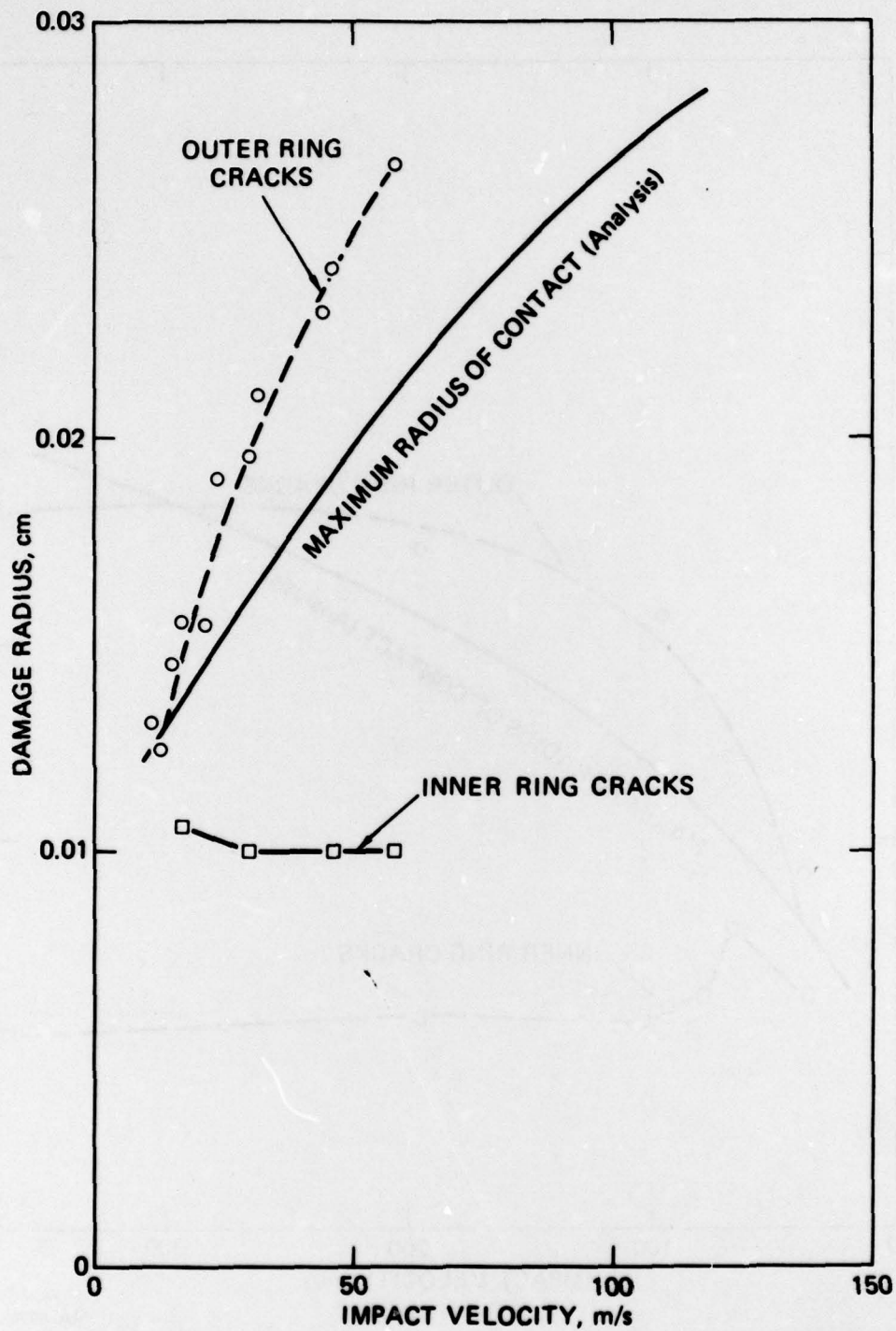
FIGURE 44   DAMAGE RADIUS RESULTS FOR IMPACT CONFIGURATION D (1.6-mm-Diameter WC Sphere/RB Si$_3$N$_4$)
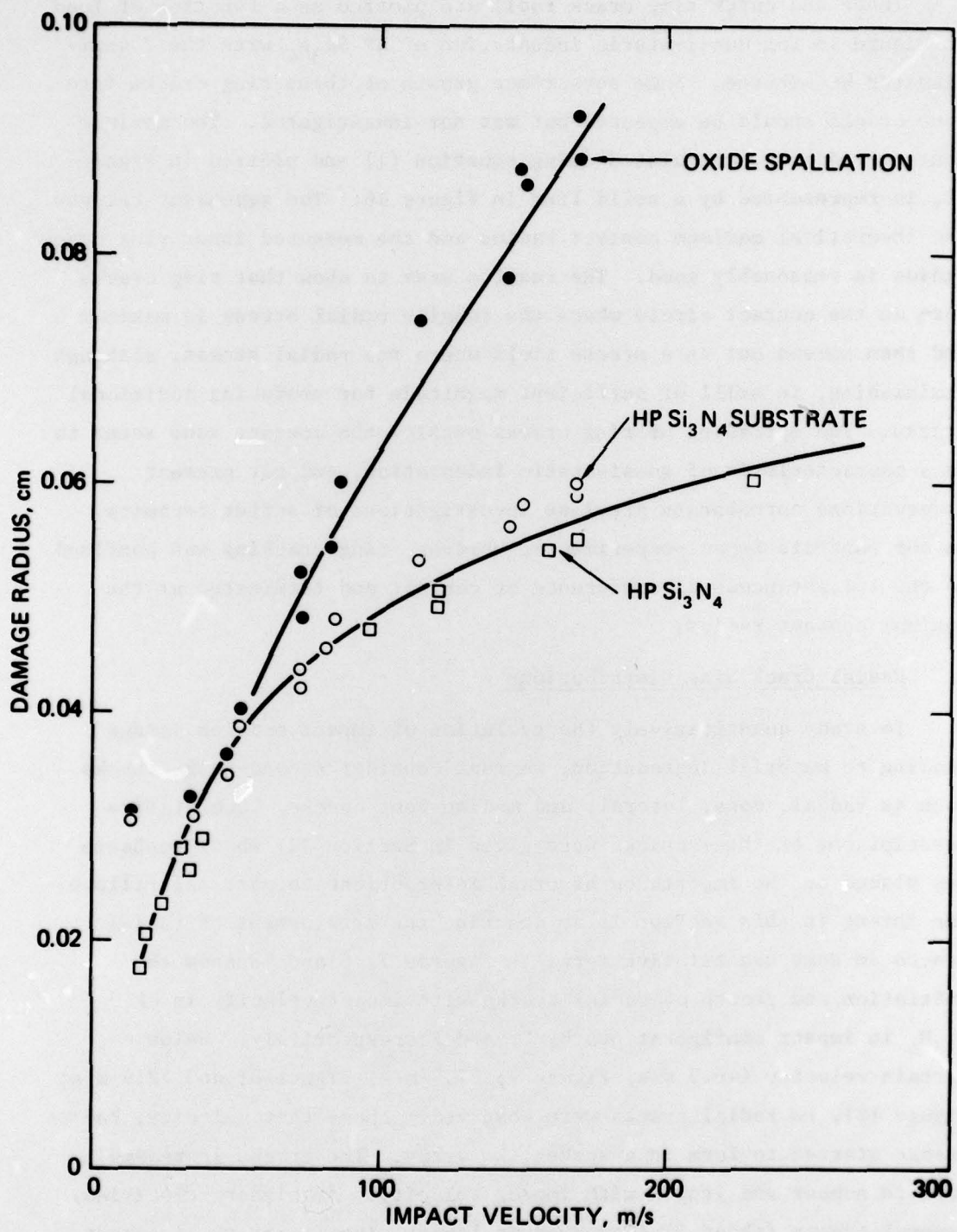
FIGURE 45    DAMAGE RADIUS RESULTS FOR OXIDIZED AND UNOXIDIZED HP Si$_3$N$_4$ (2.4-mm-Diameter WC Spheres)

Inner and outer ring crack radii are plotted as a function of load
in Figure 46 for quasi-static indentation of HP $Si_3N_4$ with the 2.4-mm-
diameter WC spheres.  Some subsurface growth of these ring cracks into
cone cracks should be expected but was not investigated.  The maximum
contact radius a, calculated using equation (1) and plotted in Figure
35, is represented by a solid line in Figure 46.  The agreement between
the theoretical maximum contact radius and the measured inner ring crack
radius is reasonably good.  The results seem to show that ring cracks
form on the contact circle where the tensile radial stress is maximum
and then spread out in a stress field where the radial stress, although
diminishing, is still of sufficient magnitude for producing additional
cracks.  The spreading of ring cracks outside the contact zone seems to
be a characteristic of quasi-static indentation, and our present
observations corroborate previous investigations of softer ceramics.
In our particle impact experiments, however, ring cracking was confined
to the instantaneous circumference of contact and terminated at the
maximum contact radius.

### Radial Crack Size Distributions

To study quantitatively the evolution of impact erosion damage
leading to material degradation, we must consider second-stage cracks
such as radial, cone, lateral, and median-vent cracks.  Qualitative
descriptions of these cracks were given in Section III where emphasis
was placed on the importance of crack interactions to material failure.
Our intent in this section is to describe the development of radial
cracks in some quantitative detail.  Figures 7, 8 and 18 show the
initiation and growth of radial cracks with impact velocity in HP
$Si_3N_4$ in impact configurations B, C, and F, respectively.  Below a
certain velocity (46.2 m/s, Figure 7; 67.7 m/s, Figure 8; and 72.6 m/s;
Figure 18), no radial cracks were observed.  Above that velocity, radial
cracks started to form in a spoke-like array.  The cracks increased
both in number and length with impact velocity.  At higher velocities,
several cracks (about 9) increased in length significantly.  A larger
number (from 20 to 25) of shorter radial cracks also appeared near the
contact periphery.  The shorter cracks have an average length of about

98
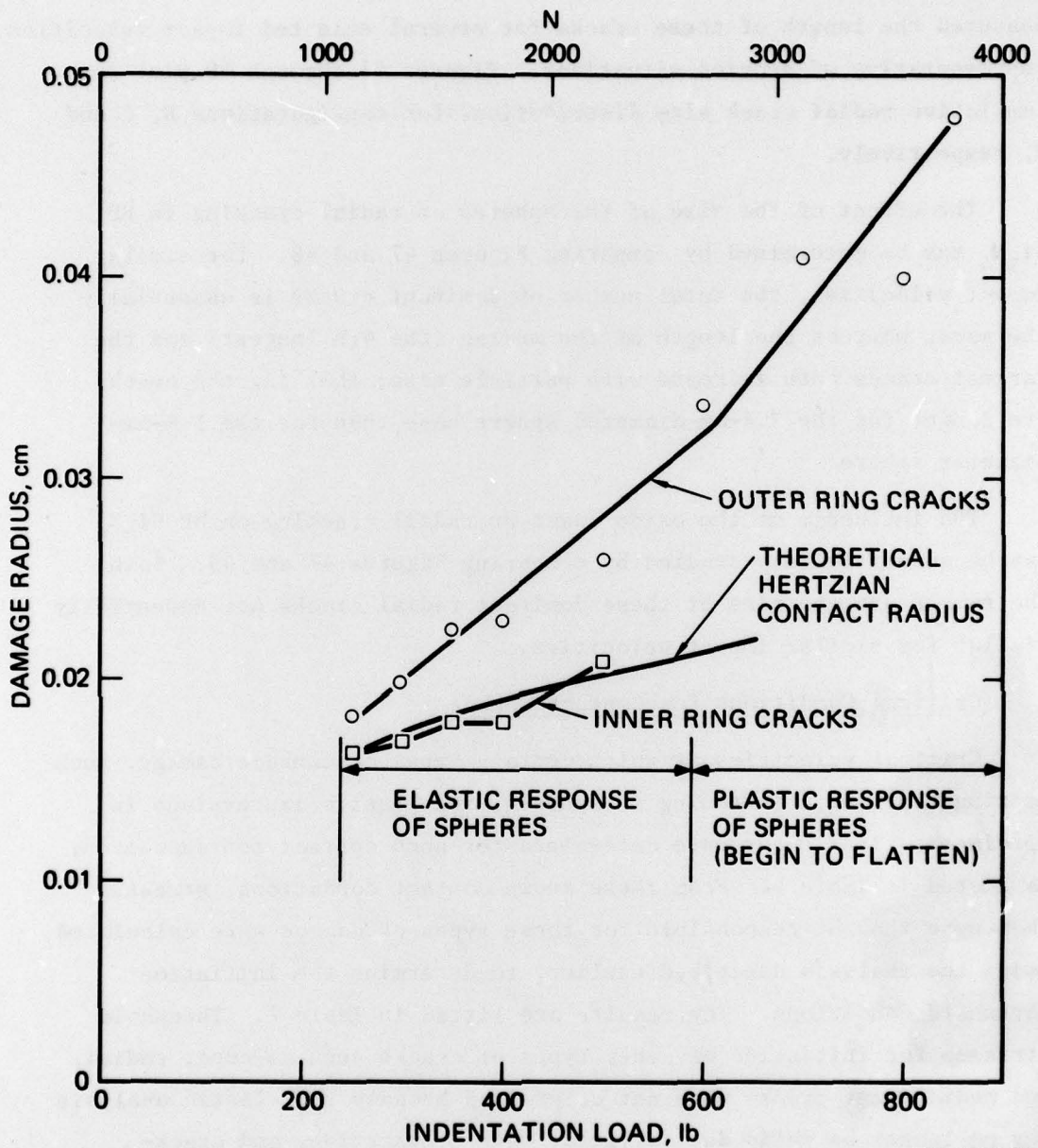
FIGURE 46    DAMAGE RADIUS RESULTS FOR QUASI-STATIC INDENTATION (2.4-mm-
Diameter WC Spheres/HP Si$_3$N$_4$)

100 μm, whereas the larger cracks (now called dominant) grew as long as 5 mm. The dominant radial cracks should be important to the problem of impact-induced strength degradation. We counted the number and measured the length of these cracks for several selected impact velocities representative of erosion situations. Figures 47 through 49 plot these cumulative radial crack size distributions for configurations B, C and F, respectively.

The effect of the size of the spheres on radial cracking in HP $Si_3N_4$ may be determined by comparing Figures 47 and 48. For similar impact velocities, the total number of dominant cracks is essentially the same, whereas the length of the median (the 4th longest) and the largest cracks both increase with particle size; that is, the cracks are longer for the 2.4-mm-diameter sphere case than for the 1.6-mm-diameter sphere.

The influence of the oxide layer on radial cracking on HP $Si_3N_4$ may be quantitatively studied by comparing Figures 47 and 49. Both the number and the size of these dominant radial cracks are essentially similar for similar impact velocities.

### Critical Conditions for Contact Damage

Critical velocities at which certain types of contact damage, such as ring cracking, flattening of spheres, and plastic impressions in specimens, first occur were determined for each contact configuration, as listed in Table 6. From these known contact conditions, stresses that were thought responsible for these types of damage were calculated, using the analysis described earlier, to determine the initiation threshold conditions. The results are listed in Table 7. Threshold stresses for initiation of other types of cracks such as cone, radial, and median-vent cracks were not determined because the elastic analysis may no longer be valid due to yield, wave propagation, and crack-interaction effects.

100
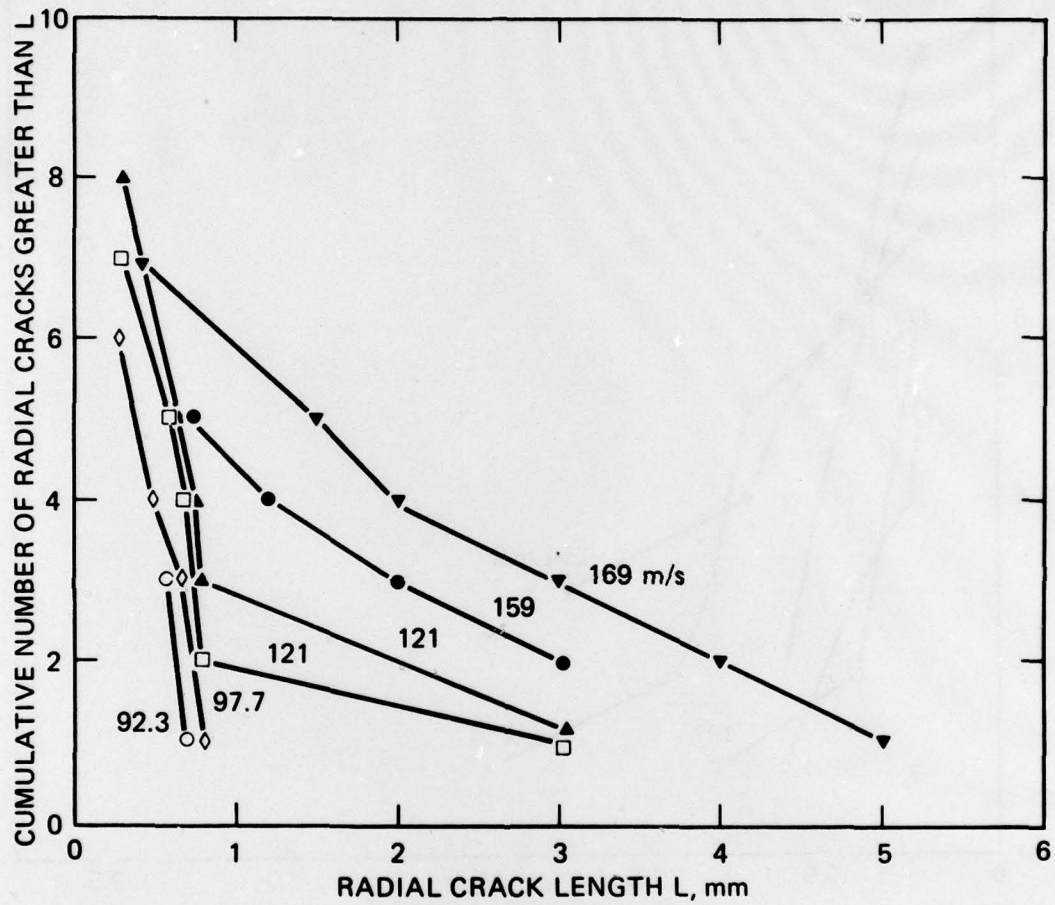
MA-4928-85

FIGURE 47    RADIAL CRACK SIZE DISTRIBUTIONS
(Impact Configuration B: 2.4 mm WC/HP $Si_3N_4$)

101
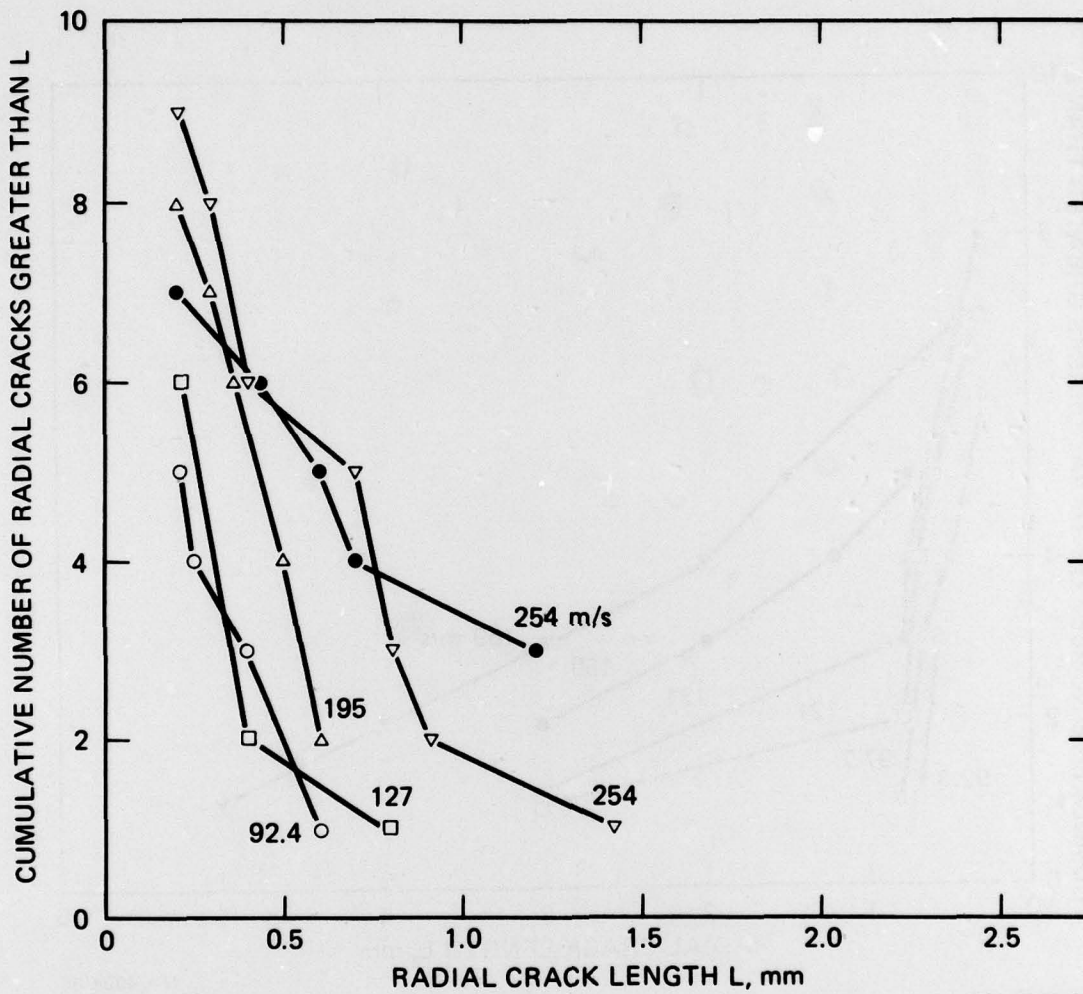
FIGURE 48    RADIAL CRACK SIZE DISTRIBUTIONS (Impact Configuration C: 1.6 mm WC/ HP Si$_3$N$_4$)

MA-4928-86

102
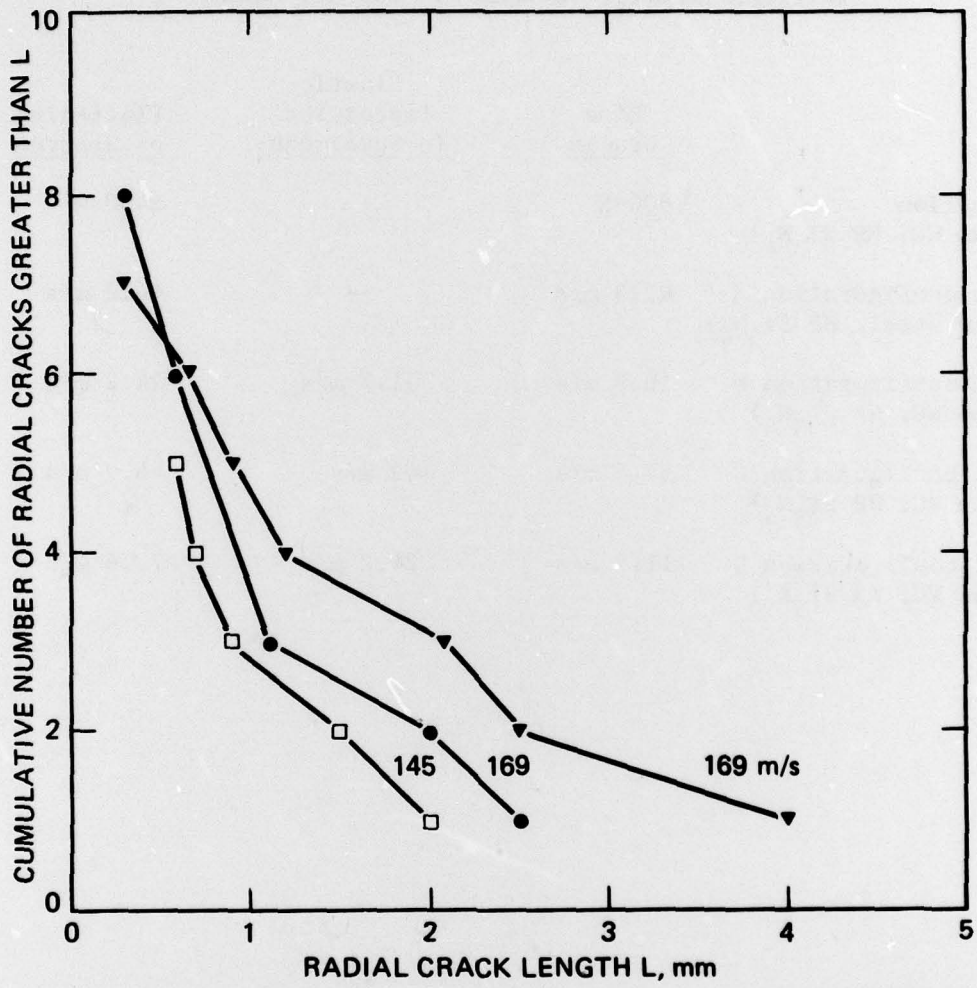
FIGURE 49    RADIAL CRACK SIZE DISTRIBUTIONS (Impact Configuration F: 2.4 mm WC/ Oxidized HP $Si_3N_4$)

103

Table 6

CRITICAL VELOCITY OR LOAD FOR CONTACT DAMAGE

|  | Ring Cracks | Plastic Impression in Specimens | Flattening of Spheres |
|---|---|---|---|
| Indentation (2.4-mm WC, HP $Si_3N_4$) | 800 N | -- | 2450 N |
| Impact configuration A (2.4-mm steel, HP $Si_3N_4$) | 42.3 m/s | -- | 46.2 m/s |
| Impact configuration B (2.4-mm WC, HP $Si_3N_4$) | 16.9 m/s | 31.7 m/s | 24.2 m/s |
| Impact configuration C (1.6-mm WC, HP $Si_3N_4$) | 37.6 m/s | ~42 m/s | 46.2 m/s |
| Impact configuration D (1.6-mm WC, RB $Si_3N_4$) | 11.3 m/s | 24.2 m/s | >72.6 m/s |

## Table 7

## CRITICAL STRESSES FOR CONTACT DAMAGE

| | Si$_3$N$_4$ Specimen Material | Sphere Type and Diameter (mm) | $\sigma_{zz}$ (GPa) | $\sigma_{rr}$ (GPa) |
|---|---|---|---|---|
| Critical normal stress (compressive) for flattening of spheres | HP | Steel, 2.40 | 17 | |
| | HP | WC, 2.40 | 25 (26*) | |
| | HP | WC, 1.60 | 31 | |
| | RB | WC, 1.60 | 27 | |
| Critical normal stress (compressive) for plastic impressions in specimens | HP | WC, 2.40 | 28 | |
| | HP | WC, 1.60 | 30 | |
| | RB | WC, 1.60 | 17 | |
| Critical radial stress (tensile) for ring cracks | HP | Steel, 2.40 | | 3.1 |
| | HP | WC, 2.40 | | 2.8 (2.9*) |
| | HP | WC, 1.60 | | 2.9 |
| | RB | WC, 1.60 | | 2.0 |

---

*Quasi-static indentation.

105

The incipient innermost ring cracks on the surface of the specimens give the location and the threshold condition for ring-crack nucleation and growth. The tensile radial stress at these locations represents the threshold and should be approximately constant for each contact configuration irrespective of impact velocity (or indentation load). For each contact configuration, the variation of the threshold stress for ring cracking with velocity (or load) was reasonably small ($\pm$ 10%), seemingly indicating that the elastic analysis is valid at least in the incipient damage regime. The average of these stresses for each contact configuration is listed in Table 7.

Contact strengths (expressed in terms of compressive normal stress at contact center) of steel and WC spheres are also compared in Table 7. Steel has significantly lower strength (17 GPa) than WC (25 GPa). Dynamic strength of the 24-mm-diameter WC spheres (25 GPa) is similar to its quasi-static strength (26 GPa), indicating little effect of loading rate. WC spheres of smaller size (1.6 mm in diameter) exhibit somewhat higher contact strength (31 GPa).

Critical stresses required for creating plastic impressions in different specimen materials show that reaction bonded $Si_3N_4$ has significantly lower strength than hot pressed $Si_3N_4$. Reaction bonded $Si_3N_4$ similarly exhibits lower resistance to ring cracking, and there is a close agreement between strength values for HP $Si_3N_4$ determined from different contact configurations.

The calculated radial tensile stresses for ring cracking in HP $Si_3N_4$ and RB $Si_3N_4$ are much higher than handbook values for flexural and uniaxial tensile stress. This may be reasonable for two reasons. First, the critical radial tensile stresses were calculated based on elastic contact, but plastic flow beneath the particle may significantly reduce the stresses considerably below these theoretical values. Second, stresses at the location where ring cracks form are triaxial and have steep gradients. Comparison of material strengths obtained from different loadings, such as particle impact and uniaxial tension may not, therefore, be entirely correct.

106

## VIII  CONCLUSIONS

Fracture damage in fully dense HP $Si_3N_4$ caused by impact of 2.4-mm-diameter WC spheres begin at a velocity of 17 m/s (radial tensile stresses of about 2.8 GPa) in the form of shallow ring cracks (Figure 7 and 34, Table 6 and 7).  Increasing velocities produce more and deeper ring cracks, and Hertzian cone cracks.  A plastic impression forms at 32 m/s (a compressive stress of 28 GPa, Figure 34, Table 6 and 7); at still higher velocities lateral and median-vent cracks are produced and the number of large radials increases to a maximum of about 8 or 9 Figure 7).  Interaction of these crack types with each other and with the specimen surface occurs at approximately 231 m/s and results in erosion.

The presence of an oxide scale (roughly 20 μm thick) had little influence on the morphology and extent of fracture damage in HP $Si_3N_4$ (pages 37 to 45).  However, the oxide layer spalled easily at low impact velocities, suggesting higher erosion rates for $Si_3N_4$ in oxidizing environments.

The damage phenomenology in 85% dense, RB $Si_3N_4$ was similar to that in the hot-pressed material (pages 30 to 36).  However, for RB $Si_3N_4$, ring cracking and all subsequent stages of the damage process began at roughly two-thirds the stress needed to produce damage in HP $Si_3N_4$ (Table 7).

A significant effect of particle size was observed (pages 30, 100), but loading rate effects were small (page 106).  Decreasing the WC particle diameter by 33% caused roughly a two-fold increase in ring crack threshold velocity (no increase in threshold stress) and a 50% increase in the threshold velocity for plastic impression (a 7% increase in stress, Table 6 and 7).

Fracture damage under quasi-static loading rates appeared to be similar to that under impact loads, and ring cracks were observed at similar load thresholds ($\sim$2.8 GPa, Table 7). However, flow and fracture of the indenting WC spheres prevented application of higher loads and hence production of further specimen damage (page 51).

An elastic Hertzian analysis of the stress field adequately predicted our observations of ring cracking in HP $Si_3H_4$ (page 92, Figure 41). In the elastic-plastic regime, however, the measured area of fracture damage was consistently broader than predicted by elastic theory, indicating that yielding and wave propagation effects must be accounted for (page 93, Figures 42-44).

# REFERENCES

1. D. A. Shockey, K. C. Dao, L. Seaman, and D. R. Curran, "Nucleation and Growth of Cracks in CVD ZnS under Particle Impact," Annual Report Part II to the Office of Naval Research, Arlington, VA, on Contract N00014-76-C-0657 (1979).

2. D. D. Cubicciotti, R. L. Jones, and K. H. Lau, "High Temperature Oxidation and Mechanical Properties of Silicon Nitride," Interim Report 5522-1 to the Air Force Office of Scientific Research, Bolling AFB, D.C., on Contract F44620-76-C-0016 (1977).

3. D. D. Cubicciotti, R. L. Jones, K. H. Lau, and D. J. Rowcliffe, "High Temperature Oxidation and Mechanical Properties of Silicon Nitride," Interim Report 5522-2 to the Air Force Office of Scientific Research, Bolling AFB, D.C., on Contract F44620-76-C-0016 (1978).

4. B. Lawn and T. R. Wilshaw, "Review Indentation Fracture:  Principles and Applications," J. Mat. Sci. <u>10</u>, 1049-1081 (1975).

5. A. G. Evans and T. R. Wilshaw, "Quasi-Static Solid Particle Damage in Brittle Solids - I. Observations, Analysis and Implications," *Acta Metallurgica* <u>24</u>, 939-956 (1976).

6. A. G. Evans, private communication (1979).

7. S. Timoshenko and J. N. Goodier, <u>Theory of Elasticity</u> 2nd Ed., (McGraw-Hill Book Co., Inc., New York, 1951).

8. G. N. Bycroft, "Forced Vibrations of a Rigid Circular Plate on a Semi-Infinite Elastic Space and on an Elastic Stratum," Philosophical Transactions of the Royal Society of London, Series A, No. 948, pp. 327-368 (1956).

9. I. S. Gradshteyn and I. W. Ryzhik, <u>Table of Integrals, Series, and Products</u> (Academic Press, New York, 1965).

10. G. N. Watson, <u>A Treatise on the Theory of Bessel Functions</u>, 2nd Ed. (Cambridge University Press 1944).

11. A Erdelyi, Ed., <u>Higher Transcendental Functions</u>, Bateman Manuscript Project, Vol. I (McGraw-Hill Book Co., Inc., New York, 1953).